Mars Odyssey Accelerometer: Report on Data Processing, Validation of Data Products and Scientific Analysis

Paul Withers[a,*]

[a] Center for Space Physics, Boston University, 725 Commonwealth Avenue, Boston, MA 02215, USA.

[*] Corresponding author email address: withers@bu.edu

Number of pages: 146

Number of figures: 72

Number of tables: 10

Proposed Running Head:

Odyssey Accelerometer Data

Editorial Correspondence to:

Paul Withers

Center for Space Physics, Boston University,

725 Commonwealth Avenue, Boston, MA 02215, USA.

Email: withers@bu.edu

Phone: (617) 353 1531

Fax: (617) 353 6463

Received ____________________; accepted ____________________

Formatted using AASTEX aasms4.sty

ABSTRACT

This report serves two purposes. First, source material for PDS documentation describing the generation of these data products. Second, source material for a scientific paper that briefly describes the generation of these data products and spends more time describing some analysis and interpretation of these data products.

Keywords: Mars, Atmosphere; Data Reduction Techniques

1. Introduction

The aim of this paper is to describe the processing of Mars Odyssey (ODY) accelerometer data and to present the results of preliminary scientific analysis of the derived data products. The structure of the paper is as follows: an introduction to the ACC datasets and a description of how the ACC dataset was processed (Section 2), a comparison to other results (Section 3), and a presentation of scientific results from analysis of the ACC data products (Sections 4–6).

ODY reached Mars on 24 October 2001 (Smith and Bell, 2005). ODY was inserted into an initial orbit around Mars with a period of 18.6 hours using chemical propulsion, then transferred into its desired science orbit, which has a period of less than two hours, by aerobraking. Aerobraking ended on 11 January 2002. Aerobraking uses atmospheric drag forces during a brief interval around periapsis to make a small adjustment to a spacecraft's orbit. Repeated over many periapses, aerobraking can cause significant orbital changes (Spencer and Tolson, 2007). The ODY accelerometer (ACC) instrument was used to measure atmospheric densities during aerobraking. These measurements influenced operational decisions during aerobraking, such as changes to periapsis altitude. The instrument was not part of the mission's scientific payload and its data were not archived at the Planetary Data System (PDS) in the usual manner. We have acquired ACC measurements and used them to obtain measurements of martian atmospheric properties.

Previous work on the ODY ACC dataset includes Tolson et al. (2007), Crowley and Tolson (2007), Bougher et al. (2006), Fritts et al. (2006), Wang et al. (2006) and Withers (2006, and references therein). Previous publications on ODY aerobraking include Spencer and Tolson (2007), Chavis and Wilmoth (2005), Mase (2005, and references therein), Smith and Bell (2005), Tolson et al. (2005), Takashima (2002) and Takashima and Wilmoth (2002).

Figures of orbit number, periapsis latitude, altitude, local solar time (LST) and L_s are contained in Tolson et al. (2005) and Tolson et al. (2007). L_s is the aerocentric longitude of the Sun, a measure of the martian season. L_s is 0° at the northern spring equinox, 90° at the northern summer solstice, 180° at the northern autumn equinox and 270° at the northern winter solstice. These figures show that the ODY ACC measurements separate naturally into two subsets — dayside and nightside. In this work, "dayside" corresponds to 12 hours $<$ LST $<$ 24 hours and "nightside" corresponds to 0 hours $<$ LST $<$ 12 hours. The boundary between dayside and nightside is not the same as the terminator that separates the sunlit and shadowed hemispheres. Sub-solar latitude changed from -24.9°N to -20.1°N during ODY aerobraking, so all latitudes poleward of 65.1°N (69.9°N) were in darkness in the polar night at the start (end) of aerobraking.

2. Data Processing

2.1. The Accelerometer Instrument and its Measurements

The ODY ACC instrument consisted of two inertial measurement units (IMUs). Each IMU contained three single-axis accelerometers, each of which measured linear acceleration along the accelerometer's axis at the position of the relevant sensor, and three single-axis gyroscopes, each of which measured angular velocity about the gyroscope's axis at the position of the relevant sensor. These measurements were converted into three-axis linear acceleration and three-axis angular velocity at a single position within the IMU before being transferred out of the IMU. "The primary IMU was used throughout aerobraking. The internal orientation of two of the three [single-axis] accelerometers was not aligned with the body axes, and so data from these two accelerometers were combined in the ground data system to form body axes accelerations" (Tolson et al., 2005). Data were acquired only near periapsis, so the dataset can easily be subdivided by orbit. Aerobraking concluded after several hundred orbits. The label “P076” refers to orbit number 76, and so on.

In this work we concentrate exclusively on the three-axis linear acceleration measurements and do not directly use the three-axis gyroscope measurements. ODY produced two distinct data streams of three-axis acceleration measurements, low rate and high rate, both of which had a nominal interval between measurements of 1 second. The generation of the high rate data stream was reported in Tolson et al. (2005). ODY's onboard computer sampled the IMU's output 200 times per second. For orbits 1–136, the mean of every 200 samples was sent to the high rate data stream each second. For orbits 137–268, the mean of the first 50 of every 200 samples was sent to the high rate data stream each second. For orbits 269–336, the mean of the first 20 of every 200 samples was sent to the high rate data stream each second (Tolson et al., 2005). Onboard memory limitations and the increase in the duration of aerobraking passes as the mission progressed were responsible for this deliberate degradation in ACC data quality. The generation of the low rate data stream has not been discussed in the scientific literature. Its noise characteristics do not change during aerobraking, which suggests that the same sampling rate was used throughout aerobraking. We hypothesize that the low rate data stream contains one of the 200 samples collected every second, not the mean of a subset of the 200 samples. This hypothesis is supported by analysis of the noise characteristics of the low rate and high rate data streams.

Low rate data have been delivered to the PDS Atmospheres Node in a non-standard format, but have not yet been peer-reviewed nor accepted into the PDS (ftp://atmos.nmsu.edu/odyssey/level0/data/). Acceleration measurements for orbit XXX were provided in an ASCII file (pXXXacc.txt) that contains time in YY/DOY-HH:MM:SS.SSS format and x, y, and z-axis accelerations in m s^{-2}. There is no accompanying documentation, so the time standard and reference frame required to use the data have to be identified by other means. Many different time standards are used by spacecraft missions. These times were confirmed to be UTC times, not barycentric dynamical times or ephemeris times (ET), by reproduction of published plots of acceleration/density versus time since periapsis for P076 (Tolson et al., 2005). We assumed that the x, y, and z-axes were those of the "M01_SPACECRAFT" frame defined by Navigation and Ancillary Information Facility (NAIF) SPICE kernel m01_v28.tf, which is identical to the Lockheed Martin (LMA) "mechanical coordinate system" for ODY (Takashima, 2002; NAIF, 2008b). The "M01_SPACECRAFT" frame and LMA "mechanical coordinate system" are identical to the "spacecraft frame" described in the PDS instrument host file for ODY (versions created after 14 March 2003). The LMA "mechanical coordinate system" and a POST "body-frame coordinate system" are also defined in Chavis and Wilmoth (2005).

High rate data have been delivered to the PDS Atmospheres Node in a non-standard format, but have not yet been peer-reviewed nor accepted into the PDS (ftp:atmos.nmsu.edu/odyssey/level0/data/). Acceleration measurements for orbit XXX were provided in a MATLAB file (LOPXXX.mat). Some documentation was provided in Microsoft Excel and Word files. We extracted variables HiACCTime and HiACC from each orbit's LOPXXX.mat file. According to the documentation, HiACCTime is time expressed as UTC seconds past J2000. These were confirmed to be UTC seconds, not ET seconds, by reproduction of published plots of acceleration/density versus time since periapsis for P076 (Tolson et al., 2005). According to the documentation, HiACC is x, y, and z-axis accelerations in m s^{-2}. These accelerations are similar to the low-rate accelerations, which suggests that they are expressed in the same coordinate system. Therefore we again assumed that the x, y, and z-axes were those of the "M01_SPACECRAFT" frame defined by SPICE kernel m01_v28.tf, which is identical to the Lockheed Martin (LMA) mechanical coordinate system for ODY (Takashima, 2002; NAIF, 2008b).

We extracted the low rate and high rate data from these files, then discarded some isolated data points. High rate data for hundreds of orbits contain gaps of >30s towards the end of the outbound leg. Data after these gaps were discarded. There is an additional gap of >5s towards the end of the outbound leg in high rate data for both P109 and P173. Data after these gaps were discarded. There is a gap of 3s between the last and penultimate data points in orbits 26, 27, 28, 38, 69, 74, 123, 155, 170, 179-189, 249, 273, 276, 285, 292, 297, 299, 301, 303, 305, and 306. The last data point was discarded in these orbits. Gaps of 1s-2s in the high rate data remain in about 20% of the orbits. These are short enough that their effects are minimal, so the data were not modified to correct for them. This completes step 1 (data cleaning) of the data processing.

2.2. Orbits with Available Data

No data were delivered to the PDS for orbits 1, 2, 3, 5, and 327. The possibility that data were acquired, but omitted from the dataset delivered to the PDS, for these orbits can be excluded. During aerobraking operations, "Quick Look Reports" were generated by the ACC team within hours of each periapsis pass in support of mission operations. These reports summarized ACC measurements from a given aerobraking pass. No "Quick Look Reports" were generated for these orbits, which suggests that no useful data were received on the ground.

Low rate data, but not high rate data, exist for orbits 4, 57, 158, 213, 255, 266, 289, and 336. The high rate data stream for orbit 137 begins well inside the atmosphere, close to periapsis, and contains measurements at 4 s intervals instead of the usual 1 s intervals. The low rate data for orbit 137 are normal. Data for orbits 4 (low rate only, periapsis altitude = 290 km) and 6 (low rate and high rate, periapsis altitude = 160 km) exist, but aerodynamic accelerations cannot be separated from non-aerodynamic accelerations when altitudes are so high and aerodynamic drag is so weak (see Section 2.3). Results for orbits 1-336 used the following data streams: no results for orbits 1, 2, 3, 4, 5, 6 and 327; results based on low rate data for orbits 57, 137, 158, 213, 255, 266, 289 and 336; and results based on high rate data for all other orbits.

2.3. Determination of Aerodynamic Accelerations from Measured Accelerations

We wish to derive atmospheric densities, ρ, from aerodynamic accelerations, $\underline{a_{aero}}$. Measured accelerations, $\underline{a_{meas}}$, are not identical to $\underline{a_{aero}}$. They are related by:

$$\underline{a_{meas}} = \underline{a_{bias}} + \underline{a_{aero}} + \underline{a_{gg}} + \underline{a_{thr}} + \underline{\omega} \times (\underline{\omega} \times \underline{r}) + \underline{\dot{\omega}} \times \underline{r} \tag{1}$$

$\underline{a_{bias}}$ represents the effect of sensor bias, $\underline{a_{gg}}$, which is called the gravity gradient term, represents the effect of differences between the acceleration due to gravity at the sensor and at the spacecraft's centre of mass, $\underline{a_{thr}}$ represents the effect of reaction control system (RCS) thruster firings, $\underline{\omega}$ is the angular velocity of the spacecraft, $\underline{r}$ is the position of the accelerometer with respect to the spacecraft's centre of mass, an overdot indicates a derivative with respect to time, and the last two terms represent the effects of angular motion of the sensor about the spacecraft's centre of mass. The derivation of atmospheric densities uses only the y-axis component of $\underline{a_{aero}}$, so we focus on the y-axis component of Equation 1. We now address each term in Equation 1.

The two angular acceleration terms can, in principle, be calculated. SPICE orientation information is sufficient to determine $\underline{\omega}$ and $\underline{\dot{\omega}}$. However, we do not know $\underline{r}$ accurately. The positions of the accelerometer and the centre of mass were measured before launch. The accelerometer has not moved since then, but the centre of mass has. Fuel consumption causes a secular change in centre of mass position. Accelerations experienced during aerobraking cause the fuel to slosh back and forth in the tanks, which also alters the centre of mass position. Rapid changes in $\underline{r}$ could introduce an additional term, a Coriolis term, into Equation 1. According to Tolson et al. (2005), the accelerometer position is (x,y,z) = (0.164, -0.544, 1.137) metres relative to the centre of mass. However, the reference frame for this position is not defined. The frame suggested by Figure 1 of Tolson et al. (2005) is not consistent with either the "M01_SPACECRAFT" frame or the "body coordinate system" (NAIF, 2008b; Takashima, 2002; Chavis and Wilmoth, 2005). According to Chavis and Wilmoth (2005), the accelerometer position at the midpoint of aerobraking was (x,y,z) = (-0.629, -0.0172, 1.1) metres relative to the centre of mass in the "body coordinate system." This is (x,y,z) = (0.0172, 0.629, -1.1) metres relative to the centre of mass in the "M01_SPACECRAFT" frame. It is likely that the frame used by Tolson et al. (2005) differs from the "M01_SPACECRAFT" frame by a factor of -1, which makes their accelerometer position (x,y,z) = (0.164, -0.544, 1.137) metres relative to the centre of mass. We do not correct $\underline{a_{meas}}$ for the two angular acceleration terms, therefore angular accelerations influence the uncertainty in $\underline{a_{meas}}$ (Section 2.5).

$\underline{a_{thr}}$ is "two orders of magnitude less than the periapsis drag effect" (Tolson et al., 2005). The typical acceleration at periapsis is 2×10^{-2} ms^{-2}, so the thruster term is on the order of 2×10^{-4} ms^{-2}. The nominal impulse, I, generated by a single RCS thruster firing is approximately $I = 0.00804038t + 0.02125765$, where t is the duration of the thruster firing in milliseconds and I is in N-sec (Mase and Burkhart, 2000). There are four RCS thrusters, labelled RCS1 to RCS4. The change in ODY's velocity due to an RCS thruster firing, $\Delta\underline{v}$, equals $I\hat{\underline{e}}/m$ where m is ODY's mass and $\hat{\underline{e}}$ is a unit vector. $\hat{\underline{e}}_{RCS1}$ = (-X, Y, -Z), $\hat{\underline{e}}_{RCS2}$ = (-X, -Y, -Z), $\hat{\underline{e}}_{RCS3}$ = (X, -Y, -Z), $\hat{\underline{e}}_{RCS4}$ = (X, Y, -Z), where $X = 0.8926$, $Y = 0.4162$, and $Z = 0.1736$ (Mase and Burkhart, 2000). These unit vectors are in the "M01_SPACECRAFT" frame. Thruster firings for orbit XXX are reported in ASCII files (pXXXthot.txt) that accompany the low rate accelerometer data. The cumulative times that each thruster has fired for are listed as functions of time. Typical thruster firings last for 0.1 sec, much less than the typical interval between cumulative times in pXXXthot.txt (1–10 sec). Since the times of thruster activity cannot be resolved, their contributions cannot be removed from the measured accelerations. Also, the actual impulse produced by a thruster will differ from the nominal impulse. Past experience has shown that determination of thruster impulse to within 50% is difficult (Tolson et al., 2005). We do not correct $\underline{a_{meas}}$ for thruster activity.

$\underline{a_{gg}}$ is on the order of 1×10^{-6} ms^{-2} (Cancro et al., 1998). This is much smaller than $\underline{a_{thr}}$, so we neglect it.

When ODY is far outside the atmosphere, $\underline{a_{meas}} = \underline{a_{bias}}$. Pre-entry and post-exit measured accelerations can be used to estimate instrument bias. Scatter in $a_{meas,lo,y}$ (the y-component of the low rate measured acceleration) was large enough that estimates of $a_{bias,lo,y}$ could not be distinguished from zero. $a_{meas,lo,y}$ was not corrected for bias. $a_{bias,hi,y}$ was calculated from pre-entry and post-exit accelerations. The pre-entry value of $a_{bias,hi,y}$ was assumed to be the mean of all $a_{meas,hi,y}$ measurements from 10s after the start of the data stream to 60s later. The post-exit value of $a_{bias,hi,y}$ was assumed to be the mean of all $a_{meas,hi,y}$ measurements from 70s before the end of the data stream to 60s later. These time ranges were chosen to ensure that aerodynamic accelerations and any transients associated with the beginning/end of the data stream were negligible. The typical pre-entry bias was -2.4×10^{-4} ms^{-2} and the typical post-exit bias was -2.2×10^{-4} ms^{-2}, as shown in Figures 1 and 2. $a_{bias,hi,y}$ was assumed to vary linearly with time during an aerobraking pass. The post-exit bias was assumed to equal the pre-entry bias for orbits 84, 91, 93, and 95 due to lack of adequate post-exit data. We correct $\underline{a_{meas}}$ for bias for high rate data only.

[FIGURE 1] [FIGURE 2]

Thus $a_{aero,lo,y} = a_{meas,lo,y}$ and $a_{aero,hi,y} = a_{meas,hi,y}$ - $a_{bias,hi,y}$. Maximum values of $a_{aero,hi,y}$ and $a_{aero,lo,y}$ are shown in Figure 3. This completes step 2 (data correction) of the data processing.

[FIGURE 3]

2.4. Reduction of Noise in the Data

We next formed 7-point and 39-point running means of $a_{aero,lo,y}$ and $a_{aero,hi,y}$, effectively 7-s and 39-s averages, and labelled them $a_{aero,lo,y,7}$, $a_{aero,lo,y,39}$, $a_{aero,hi,y,7}$, and $a_{aero,hi,y,39}$. This reduced the noise in the accelerations at the expense of spatial resolution. The duration of the 39-point time series is shorter than the duration of the 7-point time series, which is shorter than the duration of the unaveraged time series, because a 7-point running mean cannot be calculated for the first three data points in a series of measurements.

The noise inherent in $a_{aero,lo,y}$, $a_{aero,hi,y}$, $a_{aero,lo,y,7}$, $a_{aero,hi,y,7}$, $a_{aero,lo,y,39}$, and $a_{aero,hi,y,39}$ was estimated based on the standard deviation of selected pre-entry measurements. Measurements from 30s after the start of the time series to 60s later were used for $a_{aero,lo,y}$, $a_{aero,lo,y,7}$, and $a_{aero,lo,y,39}$. Measurements from 10s after the start of the time series to 200s later were used for $a_{aero,hi,y}$. Measurements from 10s after the start of the time series to 100s later were used for $a_{aero,hi,y,7}$. Measurements from 30s after the start of the time series to 60s later were used for $a_{aero,hi,y,39}$. The start times of these time series were chosen to ensure that transients associated with the beginning of the data stream did not affect any of the calculated noise values. The end times of these time series were chosen to ensure that aerodynamic accelerations did not affect any of the calculated noise values. These time series were made as long as possible to increase the accuracy of the noise calculation.

Results are shown in Figure 4 and Table 1. Noise levels clearly depend on the number of samples acquired per second: 200 for orbits 1–136, 50 for orbits 137–268 and 20 for orbits 269–330. The ratio of noise levels in $a_{aero,hi,y}$ for orbits 269–330 to orbits 1–136 is 6.05, significantly greater than the ratio of $\sqrt{200/20} = 3.16$ that would occur for samples from a Gaussian distribution. The ratio of noise levels in $a_{aero,hi,y}$ for orbits 137–268 to orbits 1–136 is 3.28, significantly greater than the ratio of $\sqrt{200/50} = 2$ that would occur for samples from a Gaussian distribution. The ratio of noise levels in $a_{aero,hi,y}$ for orbits 269–330 to orbits 137–268 is 1.84, close to the ratio of $\sqrt{50/20} = 1.58$ that would occur for samples from a Gaussian distribution. Ratios of noise levels are also stated in Table 2. This suggests that scatter in $a_{aero,hi,y}$ for orbits 137–330, but not for orbits 1–136, can be considered to be Gaussian noise.

[FIGURE 4] [TABLE 1] [TABLE 2]

2.5. Selection of Useful Data and Determination of Uncertainties

Useful data are data that are clearly dominated by aerodynamic acceleration, not other factors such as instrument noise (Figure 4), the effects of thrusters, and the effects of angular accelerations (Section 2.3). We process the dataset to remove those data points that are not useful.

Accelerations due to thrusters are on the order of 2×10^{-4} ms^{-2} (Section 2.3). Let the magnitudes of the y-component of the two angular acceleration terms in Equation 1 be Y_1 and Y_2 respectively. We estimate Y_1 and Y_2 using angular rate information from SPICE and $\underline{r}$. We tested two values for $\underline{r}$, both assumed to be in the "M01_SPACECRAFT frame", $\underline{r} = (0.164, -0.544, 1.137)$ metres (Tolson et al., 2005) and $\underline{r} = (0.0172, 0.629, -1.1)$ (Chavis and Wilmoth, 2005). Differences in Y_1 and Y_2 are relatively small, and we adopted the value derived from Tolson et al. (2005).

Data points that were smaller than a threshold were deemed to be not useful. The threshold was calculated for each time step and each of the six sets of accelerations ($a_{aero,lo,y}$, $a_{aero,lo,y,7}$, $a_{aero,lo,y,39}$, $a_{aero,hi,y}$, $a_{aero,hi,y,7}$, and $a_{aero,hi,y,39}$). The threshold was the largest of (A) the relevant noise level, (B) 2×10^{-4} ms^{-2}, (C) Y_1 and (D) Y_2. Angular accelerations determine threshold values near periapsis when accelerations significantly exceed threshold values. Further from periapsis, the time at which accelerations cross the threshold is controlled by either the effects of thrusters ($a_{aero,lo,y,7}$, $a_{aero,lo,y,39}$, orbits 7–136 of $a_{aero,hi,y}$, $a_{aero,hi,y,7}$ and $a_{aero,hi,y,39}$) or by noise ($a_{aero,lo,y}$ and orbits 137–336 of $a_{aero,hi,y}$). Thus the vertical range of ODY density profiles is not affected by angular accelerations or choice of $\underline{r}$.

Data points that were smaller than their corresponding thresholds were discarded. This sometimes resulted in large gaps in the time series of retained data points, which is not desirable. To correct this, additional data points were discarded as necessary to ensure that the time series of retained data points was continuous. For example, suppose that data points at $t < -100$s did not exceed their thresholds, data points at $-100\text{s} < t < -90$s exceeded their thresholds, data points at $-90\text{s} < t < -80$s did not exceed their thresholds, data points at $-80\text{s} < t < +100$s exceeded their thresholds and data points at $t > +100$s did not exceed their thresholds. Data points at $-80\text{s} < t < +100$s would be retained, but all other data points would be discarded, including data points at $-100\text{s} < t < -90$s. Each retained data point was assigned an uncertainty equal to its corresponding threshold. This completes step 3 (data selection) of the data processing.

Figures 5 and 6 show $a_{aero,hi,y}$, $a_{aero,hi,y,7}$ and $a_{aero,hi,y,39}$ versus time for orbit P076.

[FIGURE 5] [FIGURE 6]

2.6. Spacecraft Position, Velocity, and Orientation

Interpretation of the ACC measurements requires knowledge of ODY's position, velocity and orientation. The position, velocity, and orientation of ODY in an inertial reference frame during aerobraking were obtained from SPICE kernels m01_ab.bsp, m01_sc_ab0110.bc, m01_sc_ab0111.bc, m01_sc_ab0112.bc, m01_sc_ab0201.bc, and m01_sc_ab0202.bc (NAIF, 2008a). The position and orientation of Mars in an inertial reference frame were obtained from SPICE kernels de414.bsp and pck00008.tpc. Time-related SPICE kernels naif0008.tls and orb1_sclkscet_00129.tsc were also used in this work. The velocity of the martian atmosphere, assuming that it rotates with the solid body of the planet, in an inertial reference frame was calculated using these SPICE kernels. The velocity of the atmosphere relative to the spacecraft and of the spacecraft relative to the atmosphere can be determined from this information. Spacecraft altitude was defined as $\left|\underline{r_{ODY}} - \underline{r_A}\right|$, where $\underline{r_{ODY}}$ is the position of the spacecraft relative to the centre of mass of Mars, $\underline{r_A}$ is the position of a point on a pre-defined martian areoid relative to the centre of mass of Mars, and $\underline{r_{ODY}}$ is parallel to $\underline{r_A}$. In this work, the MOLA 0.25 x 0.25 degree areoid was used (Smith et al., 2003). Periapsis is defined in this work as the point of minimum altitude, not minimum radial distance.

SPICE kernels for ODY's orientation are not available on 28 November 2001, which encompasses aerobraking passes on orbits 58 and 59. ODY's attitude on these orbits was assumed to be $\phi = 0°$ and $\theta = -4°$, where ϕ and θ are defined in Section 2.7 (Tolson et al., 2005). This attitude, the nominal trim attitude, is consistent with ODY's average attitude for neighbouring orbits.

2.7. Derivation of Atmospheric Densities

The atmospheric density, ρ, satisfies:

$$m\,|a_{aero,y}| = \frac{\rho V^2 C_y A}{2} \tag{2}$$

where m is the spacecraft mass, $a_{aero,y}$ is the y-component of the aerodynamic acceleration, V is the scalar speed of the spacecraft relative to the atmosphere, or vice versa, C_y is an aerodynamic coefficient, and A is a reference area connected with C_y (Withers et al., 2003). Similar equations exist for all directions. We use the y-axis in the M01_SPACECRAFT frame since acceleration measurements along this axis, which is close to the velocity of the spacecraft relative to the atmosphere, have the greatest signal-to-noise ratio.

m decreased monotonically from 460.8 kg at the start of aerobraking to 451.7 kg at the end, as shown in Figure 7 (pers. comm, Mase, 2006). Uncertainty in the absolute mass is 3 kg, although the change in mass from one orbit to the next orbit is known much more accurately (<1 g). A is 11.03 m^2 (Chavis and Wilmoth, 2005). V is known from SPICE information (Section 2.6). The product $\rho \times C_y$ can be found using measured or known quantities (m, $a_{aero,y}$, V, and A) at each time step along an aerobraking pass.

[FIGURE 7]

Next, ρ and C_y are determined from the product $\rho \times C_y$. ODY's C_y, typically $\sim$2, is a function of density and the attitude of the spacecraft with respect to its velocity relative to the atmosphere. Spacecraft attitude can be expressed as two angles, ϕ and θ. If the velocity of the atmosphere relative to the spacecraft is $\underline{U} = U\underline{u}$, where $\underline{u}$ is a unit vector expressed in the "M01_SPACECRAFT frame", then pitch (θ) and yaw (ϕ) angles are defined by (Takashima, 2002):

$$u_x = \cos\theta \sin\phi \tag{3}$$

$$u_y = \cos\theta \cos\phi \tag{4}$$

$$u_z = -\sin\theta \tag{5}$$

Values of C_y for various ρ, ϕ, and θ have been determined by numerical simulation. These values constitute the "aerodynamic database." The aerodynamic database was reported in Takashima and Wilmoth (2002) and provided to us by R. Mase (pers. comm., 2006). Uncertainties in C_y are estimated to be 3% (Chavis and Wilmoth, 2005). Inputs to the numerical simulations ranged from 10^{-4} kg km^{-3} to 10^{4} kg km^{-3} for ρ, from -60° to 60° for ϕ, and -60° to 60° for θ. These ranges encompassed all conditions encountered during aerobraking. We found the unit vector $\underline{u}$ as a function of time for each aerobraking pass (Section 2.6). Angles ϕ and θ were then determined using Equations 3–5, also as functions of time for each aerobraking pass. At each time step in each aerobraking pass, the simulated value of C_y was found as a function of ρ using the aerodynamic database. The simulated value of the product $\rho \times C_y$ was also found as a function of ρ.

$\rho \times C_y$ is a **single-valued function** of ρ for any specified ϕ and θ, which enables both ρ and C_y to be found from $\rho \times C_y$. At each time step in each aerobraking pass, the observed value of the product $\rho \times C_y$ and the simulated function $\rho C_y(\rho)$ were compared to determine the value of ρ. The value of C_y followed trivially. This is illustrated in Figures 8 and 9. This technique is also discussed by Takashima and Wilmoth (2002) and Tolson et al. (2005).

[FIGURE 8] [FIGURE 9]

This process was applied to $a_{aero,lo,y}$, $a_{aero,hi,y}$, $a_{aero,lo,y,7}$, $a_{aero,hi,y,7}$, $a_{aero,lo,y,39}$, and $a_{aero,hi,y,39}$ to obtain ρ_{lo}, ρ_{hi}, $\rho_{lo,7}$, $\rho_{hi,7}$, $\rho_{lo,39}$, and $\rho_{hi,39}$. Uncertainties in each of these densities were found using (Bevington, 1969):

$$\left(\frac{\sigma_\rho}{\rho}\right)^2 = \left(\frac{\sigma_m}{m}\right)^2 + \left(\frac{\sigma_{Cy}}{C_y}\right)^2 + \left(\frac{\sigma_a}{a}\right)^2 \tag{6}$$

Derived densities that were smaller than their uncertainties were discarded. This sometimes resulted in large gaps in the time series of retained densities, which is not desirable. To correct this, other derived densities were discarded as necessary to ensure that the time series of retained densities was continuous. For example, suppose that densities at $t < -100$s did not exceed their uncertainties, densities at $-100\text{s} < t < -90$s exceeded their uncertainties, densities at $-90\text{s} < t < -80$s did not exceed their uncertainties, densities at $-80\text{s} < t < +100$s exceeded their uncertainties and densities at $t > +100$s did not exceed their uncertainties. Densities at $-80\text{s} < t < +100$s would be retained, but all other densities would be discarded, including densities at $-100\text{s} < t < -90$s. This completes step 4 (density derivation) of the data processing.

Figures 10–14 show time series of u_x, u_z, ϕ and θ for orbit P076. Figure 15 shows time series of C_y for orbit P076. Figures 16 and 17 show time series of ρ_{hi}, $\rho_{hi,7}$ and $\rho_{hi,39}$ for orbit P076.

[FIGURE 10] [FIGURE 11] [FIGURE 12] [FIGURE 13] [FIGURE 14] [FIGURE 15] [FIGURE 16] [FIGURE 17]

Each aerobraking pass has up to six derived density profiles: ρ_{lo}, ρ_{hi}, $\rho_{lo,7}$, $\rho_{hi,7}$, $\rho_{lo,39}$, and $\rho_{hi,39}$. Each derived density value has an associated altitude. Let z_{max} be the greatest altitude for a given density profile. Values of σ_ρ and $\sigma_{aaero,y}$ at z_{max}, as well as the value of z_{max}, are listed in Table 3 for the three types of high rate density profiles at the start and end of aerobraking.

[TABLE 3]

Derived densities rely on knowledge of the speed and direction of the spacecraft relative to the atmosphere. The velocity of ODY in an inertial frame is determined from SPICE information (Section 2.6). The velocity of the atmosphere in an inertial frame is determined from the assumption that the atmosphere rotates at the same angular velocity as the solid planet. This assumption is not accurate. Models predict zonal and meridional winds of $\sim$100 ms^{-1} at aerobraking altitudes (Bougher et al., 1999; Bougher et al., 2000; Bougher et al., 2002). These speeds are consistent with results from the first efforts to determine winds from aerobraking measurements (Baird et al., 2007; Crowley and Tolson, 2007).

If, instead of assuming solid body rotation for the atmosphere, we assume that there is a zonal wind of 100 ms^{-1}, then derived densities are altered by <1%. A meridional wind of 100 ms^{-1} alters derived densities by $\sim$5%. Data users should be aware of this potential source of error, which is not included in the derived uncertainties (Equation 6) because the accuracy of wind predictions has not been quantified.

2.8. Derivation of Constant Altitude Data Products

The 1-second sampling rate (<1 km vertical resolution) in the derived density profiles is not necessary for many studies of large-scale atmospheric processes. Another dataset of reduced size, called the constant altitude dataset, was generated from ρ_{39} data to support such studies. Orbits for which $\rho_{hi,39}$ data were available used $\rho_{hi,39}$ data. Orbits for which $\rho_{hi,39}$ data were not available used $\rho_{lo,39}$ data.

ρ_{39} measurements for a given orbit were first split in two. All densities before periapsis, including the periapsis density, were assigned to the inbound leg. All densities after periapsis, including the periapsis density, were assigned to the outbound leg. Each leg was processed separately. Target altitudes were defined as 100 km, 110 km, 120 km, 130 km, 140 km, 150 km, and 160 km. Periapsis never reached 90 km. If density measurements existed more than 3 km below the target altitude and more than 3 km above the target altitude, then we proceeded to determine constant altitude data products for that target altitude.

We assume that densities, ρ, within 5 km of the target altitude, z_0, satisfy:

$$\rho = \rho_0 \exp\left(\frac{-(z - z_0)}{H_\rho}\right) \tag{7}$$

where ρ_0 is the density at z_0 and H_ρ is the density scale height between $z_0 - 5$ km and $z_0 + 5$ km. Equivalently:

$$\ln \rho = \ln \rho_0 + \left(\frac{-1}{H_\rho}\right)(z - z_0) \tag{8}$$

Defining $y = \ln \rho$, $x = z - z_0$, $a = \ln \rho_0$ and $b = -1/H_\rho$, we have:

$$y = a + bx \tag{9}$$

Values of x, the independent variable, are known exactly. Values of y, the dependent variable have uncertainties $\sigma_y = \sigma_\rho/\rho$. We use standard least-squares techniques, Equation 6-12 of Bevington (1969) as implemented by the IDL POLY_FIT procedure, to determine best-fit values of a and b, and uncertainties σ_a and σ_b. Then we have (Bevington, 1969):

$$\rho_0 = e^a \tag{10}$$

$$\sigma_{\rho_0} = \sigma_a \rho_0 \tag{11}$$

$$H_\rho = \frac{-1}{b} \tag{12}$$

$$\sigma_{H_\rho} = H_\rho^2 \sigma_b \tag{13}$$

Assuming an isothermal atmosphere, temperature, T_ρ, and its uncertainty, σ_{T_ρ}, were estimated from the fitted density scale height, H_ρ, using:

$$T_\rho = \frac{\mu g H_\rho}{k_B} \tag{14}$$

$$\frac{\sigma_{T_\rho}}{T_\rho} = \frac{\sigma_{H_\rho}}{H_\rho} \tag{15}$$

where μ is mean molecular mass, assumed to be 43.49 daltons, g is the acceleration due to gravity, and k_B is Boltzmann's constant. The assumed μ, which corresponds to Viking Lander measurements at the surface, is an overestimate (Owen, 1992; Magalhães et al., 1999). Light species such as O are more abundant in the thermosphere than near the surface. Data users who wish to make a different assumption concerning μ can simply multiply our T_ρ and σ_{T_ρ} by the ratio of their desired mean molecular mass to 43.49 daltons. g is given by:

$$g = \frac{GM}{(R_{ref} + z)^2} \tag{16}$$

where R_{ref} is the mean equatorial radius of the MOLA areoid used in this work, 3396 km, G is the gravitational constant, and M is the mass of Mars (Smith et al., 2003). $GM = 4.2828382332 \times 10^{13}$ m^3 s^{-2} (Tyler et al., 2000). As an example, constant altitude data products for orbit P076 are shown in Table 4.

[TABLE 4]

No fitted ρ, H_ρ, or T_ρ had a smaller absolute value than its uncertainty. One set of results for H_ρ and T_ρ was negative (orbit 12, outbound 130 km, H_ρ = -75 km, σ_{H_ρ} = 29 km, T_ρ = -1340K, σ_{T_ρ} = 480K). Recall that aerobraking passes are not vertical; they span significant horizontal extent. Densities do decrease with altitude at 130 km on the outbound leg of this aerobraking pass, presumably due to some kind of wave in the atmosphere, so this negative scale height is formally accurate. However, this illustrates that caution should be used when interpreting scale heights derived from non-vertical density profiles. Fitted values of ρ cannot be negative, due to the exponential fitting approach.

The orbits for which constant altitude results were obtained are listed in Table 5. Results were obtained at 110 km and 120 km for almost all orbits, at 100 km for >50% of orbits, and at 140 km outbound for >20% of orbits. Results at 150 km and 160 km are essentially non-existent. Accelerations were measured at 140 km on outbound legs at daytime LSTs more frequently than at 140 km on inbound legs, and the difference between daytime and nighttime densities at 140 km explains why there are so many more outbound 140 km measurements than inbound 140 km measurements. Typical uncertainties in fitted ρ, H_ρ, and T_ρ are shown in Table 6.

[TABLE 5] [TABLE 6]

2.9. Derivation of Pressure and Temperature Profiles

Vertical pressure, p, and temperature, T, profiles can be derived from a vertical density profile using:

$$\frac{dp}{dz} = -\rho g \tag{17}$$

$$p = \frac{\rho k_B T}{\mu} \tag{18}$$

where g and μ are as defined in Section 2.8. Equation 17 needs an upper boundary condition. If the atmosphere is isothermal, then $p = \rho g H_\rho$, where H_ρ is the density scale height, which can be derived from a fit to the vertical density profile. If applied to aerobraking density profiles, which are non-vertical, this approach will produce biased p and T profiles because horizontal gradients in the atmosphere are not properly accounted for. Differences between values of the periapsis pressure derived for the inbound and outbound legs are a particularly visible manifestation of this problem (see below). Nevertheless, we have used this approach to produce p and T profiles corresponding to the inbound and outbound density profiles on each aerobraking pass. $T\,(p)$ profiles are so much more common in atmospheric modelling than $\rho\,(z)$ profiles that the production of p and T profiles increases the value of the ODY ACC dataset to many potential users despite inevitable biases in the p and T profiles.

Pressure and temperature profiles have been derived from the unaveraged densities, from the 7-point averaged densities, and from the 39-point averaged densities. Orbits for which high rate data were available used high rate data. Orbits for which high rate data were not available used low rate data.

The density measurements for a given orbit were first split in two. All densities before periapsis, including the periapsis density, were assigned to the inbound leg. All densities after periapsis, including the periapsis density, were assigned to the outbound leg. Each leg was processed separately. Any measurement whose altitude is greater than the altitude of a density measurement that is less than twice the density uncertainty was discarded. This improves the application of the upper boundary condition for Equation 17 and the forthcoming Monte Carlo analysis. If the altitude range of the remaining densities was less than 5 km, then no pressure or temperature profile was obtained.

An exponential fit to all densities within 10 km of the altitude of the highest measurement was used to determine the density scale height at the altitude of the highest measurement. Uncertainties in the densities were used to determine the uncertainty in the fitted density scale height. Procedures were the same as in Section 2.8.

A Monte Carlo approach was used to obtain the pressure and temperature profiles, with uncertainties. A dummy density profile was generated using the true density profile and its uncertainties. A dummy density scale height for the top of the profile was generated using the fitted density scale height and its uncertainty. All uncertainties were assumed to correspond to a Gaussian distribution. If any of the dummy density values or the dummy density scale height were negative, then the dummy profiles were generated again. A single pressure profile and a single temperature profile were then obtained using Equations 17–18. After N pressure/temperature profiles were obtained, where $N = 1000$, the mean and standard deviation pressure/temperature were calculated at each altitude. The uncertainty in pressure/temperature was assumed to equal the standard deviation in the Monte Carlo ensemble. Any p measurement whose altitude is greater than the altitude of a p measurement that is less than its uncertainty was discarded. T measurements were treated similarly.

Periapsis pressure and temperature, and their uncertainties, need special treatment, since they are calculated twice, once for the inbound leg and once for the outbound leg. The best estimates of periapsis conditions are calculated as follows:

$$\frac{1}{\sigma^2_{Xbest}} = \frac{1}{\sigma^2_{Xin}} + \frac{1}{\sigma^2_{Xout}} \tag{19}$$

$$\frac{X_{best}}{\sigma^2_{Xbest}} = \frac{X_{in}}{\sigma^2_{Xin}} + \frac{X_{out}}{\sigma^2_{Xout}} \tag{20}$$

where X is periapsis p or T, X_{in} and X_{out} are the inbound and outbound values of X, σ_{Xin} and σ_{Xout} are their uncertainties, X_{best} is the best estimate of X, and σ_{Xbest} is its uncertainty.

Differences between p_{in} and p_{out} are shown in Figure 18. The differences are not distributed randomly. Figure 19 shows how the differences are affected by periapsis latitude and by whether the inbound leg is poleward or equatorward of the outbound leg.

[FIGURE 18] [FIGURE 19]

Figures 20–22 show the vertical pressure and temperature profiles for orbit P076.

[FIGURE 20] [FIGURE 21] [FIGURE 22]

2.10. Summary of Data Sources

This data processing has used many sources of information. For convenience, all sources are collected here in one place. Time series of accelerations were obtained in files pXXXacc.txt (low rate) and LOPXXX.mat (high rate) which were provided to Jim Murphy and the Atmospheres Node of the PDS by the aerobraking team. Frame information was obtained from SPICE kernel m01_v28.tf. ODY position, velocity and orientation were obtained from ODY SPICE kernels m01_ab.bsp, m01_sc_ab0110.bc, m01_sc_ab0111.bc, m01_sc_ab0112.bc, m01_sc_ab0201.bc, and m01_sc_ab0202.bc. Additional information on time and planetary motions was obtained from generic SPICE kernels de414.bsp, pck00008.tpc, naif0008.tls and orb1_sclkscet_00129.tsc. Altitudes were obtained using the 0.25 x 0.25 degree MOLA areoid. ODY's mass history was obtained from R. Mase in file Nav_reconstr_thru_P338.xls. ODY's aerodynamic database was obtained from R. Mase in file 01_aerodatabase.v1.inc. ODY's area of 11.03 m^2 was obtained from Chavis and Wilmoth (2005)

3. Validation of Results

3.1. Validation of Results for Time and Position

These results can be compared against the unpeer-reviewed data products at the PDS. These include UTC time, altitude, latitude, longitude, LST, solar zenith angle (SZA), ρ, σ_ρ, H_ρ, and $\sigma_{H\rho}$ at periapsis, inbound 110 km, inbound 120 km, outbound 110 km, and outbound 120 km. We refer to these as the "aerobraking team's results". In this section, absolute differences in results are defined as the results of this work minus the aerobraking team's results, ratios in results are defined at the results of this work divided by the aerobraking team's results, and relative differences in results are defined as (the results of this work minus the aerobraking team's results) divided by the aerobraking team's results. Three periapsis times in the aerobraking team's results are incorrect. The time stated for orbit P017 is stated as zero. The time stated for orbit P029 is that of orbit P028. The time stated for orbit P068 is that of orbit P027. Therefore results involving periapsis time are not calculated for these orbits in this section.

Differences in periapsis time are shown in Figure 23. Differences in periapsis time are +5 seconds at the start of aerobraking. This time offset changes steadily during aerobraking. Differences in periapsis time are -60 seconds at the end of aerobraking. The difference at orbit P209 deviates from the general trend, so this orbit is not included in Figures 25–36.

[FIGURE 23]

Differences in periapsis latitude are shown in Figure 24. Differences in periapsis latitude are -0.6°N at the start of aerobraking. This meridional offset changes steadily during aerobraking. Differences in periapsis latitude are -4.0°N at the end of aerobraking.

[FIGURE 24]

Differences in periapsis altitude are shown in Figure 25. Differences in periapsis altitude are +0.1 km at the start of aerobraking. This vertical offset changes steadily during aerobraking. Differences in periapsis altitude are -0.5 km at the end of aerobraking.

[FIGURE 25]

Differences in periapsis longitude are shown in Figure 26. Differences are greatest near the pole, when the distance that corresponds to one degree of longitude is smallest. Differences in periapsis LST, which are similar, are shown in Figure 27.

[FIGURE 26] [FIGURE 27]

Differences in periapsis SZA are shown in Figure 28.

[FIGURE 28]

Figures 29 and 30 show that differences in periapsis latitude and differences in periapsis altitude are correlated with periapsis latitude.

[FIGURE 29] [FIGURE 30]

Differences in periapsis time, periapsis longitude, periapsis LST and periapsis SZA are also correlated with periapsis latitude, as shown in Figures 31–34, if the sign of differences obtained on the dayside is reversed.

[FIGURE 31] [FIGURE 32] [FIGURE 33] [FIGURE 34]

If we redefine our periapses to occur at the aerobraking team's periapsis times, then differences between our results and the aerobraking team's results are reduced by between one and two orders of magnitude. Differences in redefined periapsis longitude, LST and SZA are negligible. Differences in redefined periapsis latitude are clearly correlated with periapsis latitude, as shown in Figure 35. Differences in redefined periapsis altitude, which are approximately 100 m, are also influenced by periapsis latitude, but exhibit substantial scatter as shown in Figure 36.

[FIGURE 35] [FIGURE 36]

A plausible explanation for these results is that different areoids were used in this work and the aerobraking team's work. The documentation accompanying the aerobraking team's results does not specify which areoid was used. The MGS accelerometer archives at the PDS used an ellipsoid with equatorial radius of 3393.4 km and flattening, f, of 0.0052083 with fourth degree and order corrections for gravitational potential. The correction coefficients were not stated (http://pds-atmospheres.nmsu.edu/PDS/data/mgsa_0002/catalog/altds.cat). The MOLA 0.25 x 0.25 degree areoid was used in this work (Smith et al., 2003).

The aerobraking team results do not include times for inbound 110 km or the other fixed altitude levels, so we cannot compare times for these results. The latitude differences between our results and the aerobraking team's results for these altitude levels are less than 0.5 degrees. The use of different areoids will clearly lead to some differences in such latitudes. We now demonstrate that the scale of the latitude difference is consistent with the previous results that motivated the hypothesis of different areoids. If this work and the aerobraking team's work used two different areoids, then the two sets of results will cross the inbound 110 km altitude at different points along the trajectory. Consequently, the two sets of results will cross the inbound 110 km altitude at different radial distances from the centre of mass of Mars, different UTC times and different latitudes. Multiplication of these latitude differences by the rate of change in altitude with respect to latitude yields vertical differences of about 0.5 km, which is the same scale as the differences in periapsis altitude shown in Figure 30. Therefore the scale of the latitude differences in the constant altitude results is consistent with the scale of the differences in periapsis altitude.

Figure 37 shows that periapsis latitude is close to the mean of the inbound and outbound 120 km latitudes for our results, but not for the aerobraking team's results. We label periapsis latitude as L_p, latitude at 120 km on the inbound leg as L_{in120}, latitude at 120 km on the outbound leg as L_{out120}, and define Q as $0.5 \times (L_{in120} + L_{out120}) - L_p$. Q is non-zero for our results near the pole, which is expected when the aerobraking pass goes across the pole. At all other latitudes, Q is zero for our results but not for the aerobraking team's results. Orbit 331 is an example. The aerobraking team's results have inbound 120 km at 15.76°N, periapsis at 25.67°N, and outbound 120 km latitude at 27.96°N. Inbound 120 km is 10 degrees away from periapsis, outbound 120 km is 2 degrees away. By contrast, a figure similar to Figure 37 using MGS results at 130 km, which have been archived and peer-reviewed by the PDS, shows that periapsis latitude was within 1 degree of the mean of the inbound and outbound latitudes, except when MGS was close to a pole. It is difficult to develop a hypothesis that can explain the results in Figure 37; one unlikely possibility is that the aerobraking team's periapsis results use a different areoid from their fixed altitude results.

[FIGURE 37]

If positions such as "periapsis" and "inbound 110 km" refer to different positions along the aerobraking trajectory in our work and the aerobraking team's work, then differences between our results are inevitable. Given a scale height of 10 km, a difference in altitude of 0.5 km corresponds to a difference in density of 5%.

3.2. Validation of Results for Density and Density Scale Height

Figures 38–41 and Table 7 compare our results and the aerobraking team's results for densities at 110 km and 120 km (inbound and outbound). The mean of the relative difference is 6% at 110 km and 10% at 120 km. The standard deviation of the relative difference is 6% at 110 km and 10% at 120 km. Differences $\sim$5% are expected due to areoid differences. Differences due to different data processing approaches (such as whether to use a data point in a fit or not, different interpolation techniques within the aerodynamic database, or differences in uncertainties that subsequently affect a fit) might also be expected. We suggest that these differences could be on the order of the uncertainties in the results. Uncertainties in the aerobraking team's densities are $\sim$5% at 110 km and 120 km. Uncertainties in our densities are $\sim$1% at 110 km and $\sim$3% at 120 km. These uncertainties are probably too low because they were calculated using the assumption that uncertainties in mass ($<$1%) and drag coefficient (3%) were Gaussian, when they are actually systematic uncertainties. The effects of unknown winds were also neglected, but this is likely to affect both sets of results equally (Section 2.7). These effects (5% due to areoid, 5% due to other causes) are sufficient to explain differences of 10%. However, results at 120 km differ by more than this on many orbits.

[FIGURE 38] [FIGURE 39] [FIGURE 40] [FIGURE 41] [TABLE 7]

Figures 42–45 and Table 7 compare our results and the aerobraking team's results for density scale heights at 110 km and 120 km (inbound and outbound). A large difference is seen in the outbound density scale height at 110 km for orbit P122 (Figure 43). Figure 46 shows that our density scale height of 53 km, which is much larger than the aerobraking team's density scale height of 12.5 km, is consistent with our density profile. Note also that the strong waves in Figure 46 could cause larger-than-expected differences between our densities and the aerobraking team's densities. Our densities at 120 km are based upon fits to data points between 115 km and 125 km. If the aerobraking team used, say, data points between 117 km and 123 km and had a difference in absolute altitudes of 1 km, then significant differences in derived densities at 120 km should be expected when density profiles contain strong waves. This may help explain the relatively large density differences at 120 km. The mean of the relative difference in density scale height is 10% at 110 km and 7% at 120 km. The standard deviation of the relative difference is 20% at 110 km and 15% at 120 km. Negligible differences are expected due to areoid differences and differences in altitude of 0.5 km (Withers, 2006). Uncertainties in the aerobraking team's density scale heights are ∼10% at 110 km and 120 km. Uncertainties in our density scale heights are ∼3% at 110 km and ∼6% at 120 km. Uncertainties in our density scale heights are not underestimated by the assumption that systematic uncertainties in mass (<1%) and drag coefficient (3%) were Gaussian. Such systematic uncertainties lead to systematic density uncertainties that do not affect derived scale heights.

[FIGURE 42] [FIGURE 43] [FIGURE 44] [FIGURE 45] [FIGURE 46]

The relative difference in inbound density at 110 km is correlated with inbound density at 110 km ($r = 0.47$, where r is the correlation coefficient, using the aerobraking team's densities and $r = 0.55$ using our densities). The relative difference in outbound density at 110 km is correlated with outbound density at 110 km ($r = 0.49$ using the aerobraking team's densities and $r = 0.59$ using our densities). Correlations are significantly weaker at 120 km, $r = 0.05$ for inbound using the aerobraking team's densities, $r = 0.27$ for inbound using our densities, $r = 0.26$ for outbound using the aerobraking team's densities, and $r = 0.40$ for outbound using our densities.

Relative differences in density scale height are strongly correlated with our density scale heights, but not with the aerobraking team's density scale heights. At 110 km, inbound, $r = 0.38$ using the aerobraking team's density scale heights and $r = 0.81$ using our density scale heights. At 110 km, outbound, $r = 0.29$ using the aerobraking team's density scale heights and $r = 0.93$ using our density scale heights. At 120 km, inbound, $r = 0.34$ using the aerobraking team's density scale heights and $r = 0.76$ using our density scale heights. At 120 km, outbound, $r = 0.37$ using the aerobraking team's density scale heights and $r = 0.80$ using our density scale heights. These striking correlations involving density scale heights could occur if our density scale heights are incorrect, but the aerobraking team's density scale heights are not. To provide reassurance that this hypothesis is untrue, Figure 47 shows that our density scale heights are consistent with our density profiles. The inbound density scale height at 110 km on orbit P081 is 12.6 km in our results and 9.0 km in the aerobraking team's results. The inbound density at 110 km on orbit P081 is 11.6 kg km^{-3} in our results and 10.6 kg km^{-3} in the aerobraking team's results. Figure 47 shows that our fitted density and density scale height are consistent with our density profile, but the aerobraking team's fitted density and density scale height are not consistent.

[FIGURE 47]

There are several trends in the differences between our results and the aerobraking team's results. These trends are presumably related to the underlying causes of the differences, but we are not able to use the trends to identify the causes.

4. Science — Density Profiles

4.1. Small-scale Structure

Oscillatory small-scale structure is present in the 7-second density profiles, as shown in Figure 48. This can be quantified by the following figure-of-merit, X:

$$Y = 2\frac{(\rho_7 - \rho_{39})}{(\rho_7 + \rho_{39})} \tag{21}$$

$$X = \sqrt{\overline{Y^2}} \tag{22}$$

where ρ_7 and ρ_{39} are 7-second and 39-second densities, respectively, and $\overline{Y^2}$ is the mean value of Y^2. Results are shown in Figure 49. Small-scale structure is probably due to gravity waves, and is therefore affected by conditions in the lower atmosphere that control gravity wave excitation and upward propagation (CreaseyA et al., 2006; CreaseyB et al., 2006).

[FIGURE 48] [FIGURE 49]

The typical value of X for ODY is 0.1, slightly larger than typical values for MGS, which are shown in Figure 4a of Withers (2006). MGS's dayside values of X were largest at 60°N and 60°S. ODY's dayside values of X have limited meridional range, but are consistent with this trend. The dayside MGS Phase 1 data and dayside ODY data are quite consistent — X is 0.15 around 60°N and decreases to 0.10 30° away. The dayside MGS Phase 2 data, where X is 0.07–0.08 and is not peaked at 60°N, are not consistent with these. The consistency between ODY and MGS Phase 1 data makes it unlikely that the Noachis dust storm, which affected MGS Phase 1 data only, controlled small-scale structure in MGS Phase 1. The L_s ranges of MGS Phase 1, MGS Phase 2 and ODY are 180°–300°, 30°–90° and 260°–310°, respectively. The consistency in X between MGS Phase 1 and ODY data, but not MGS Phase 2 data, might be due to seasonal effects. ODY's nightside values of X, which have a mean of 0.10, are essentially independent of latitude. The meridional dependence of MGS's nightside values of X, which have a mean of 0.07, cannot be determined due to their limited meridional range.

Several MGS profiles contain sudden changes in density that appear more step-like than oscillatory. Such changes are less common in ODY profiles. We identified all 7-second density profiles in which density changed by a factor of two in less than five seconds within 100 seconds of periapsis. Six of the available 329 ODY profiles (1.8%) satisfied this criterion, compared to 34 of the available 800 MGS profiles (4.3%). The sudden density changes in some of these 34 MGS profiles, such as P0041, P0114 and P1123, which are shown in Figures 4b–4d of Withers (2006), are visually striking. Only one ODY profile, P056, has a comparable appearance, as shown in Figure 50.

[FIGURE 50]

4.2. Polar Warming

Scale heights increase as latitude increases towards the north pole (Bougher et al., 2006). This increase is not zonally uniform. Figure 51 shows that nightside scale heights at 110 km are zonally uniform equatorward of 70°N, but greatest at longitudes between 90°E and 270°E for latitudes poleward of 75°N. Tolson et al. (2005) saw zonal structure in density at polar latitudes, also dominated by wavenumber 1.

[FIGURE 51]

A lower atmosphere general circulation model, supported by MGS Thermal Emission Spectrometer (TES) data, predicted that two eastward propagating travelling waves with zonal wavenumber 1 would be strong at northern latitudes during ODY aerobraking (Wilson et al., 2002). These two modes had periods of 6.5 and 20 sols. The MGS Mars Horizon Sensor Assembly (MHSA) acquired a global map of lower atmospheric temperatures at fixed local times once per sol (e.g. Martin and Murphy, 2001). MHSA data showed a region of high temperatures centred on the pole in the northern hemisphere during ODY aerobraking. The latitude of the boundary of this region varied with longitude. On any given day, the zonal variation in boundary latitude was dominated by wavenumber 1. The phase and amplitude of this wavenumber 1 component varied. At times, the phase shifted 30°–50° eastward each sol (pers. comm., T. Martin, 2001). This might explain why zonal structure with a strong wave 1 component is common in analyses of short intervals of ODY data and why zonal structure is weak in analyses of long intervals of ODY data.

Numerous profiles acquired during the early stages of ODY aerobraking contained evidence of unusually large horizontal density gradients. Meridional density gradients are typical near the winter pole (Tolson et al., 2005; Bougher et al., 2006). Such evidence included large changes in density over a small change in altitude (orbit P011, Figure 54) and periapsis density being significantly smaller than the maximum density (orbit P012, Figure 55).

[FIGURE 52] [FIGURE 53] [FIGURE 54] [FIGURE 55]

We continue to investigate possible wavenumber 1 structure in the polar vortex by analysing all orbits with periapsis altitude below 130 km, periapsis latitude less than 80°N and periapsis LST greater than 12 hours. Orbits 9 to 80 satisfy these criteria, and we examine their 7-second density profiles. The ratio of maximum density to periapsis density is greater than 1.4 in 12 of these 72 orbits (17%). If the ratio of maximum density to periapsis density was greater than 1.4 for orbit X, then this ratio was always smaller than 1.4 for orbits $X - 1$ and $X + 1$. There is only a 12% chance of this occurring randomly. Therefore some mechanism is preventing orbits with high ratios of maximum density to periapsis density from occurring consecutively. Suppose this mechanism is represented as a black box whose output depends deterministically on a set of inputs and that its output determines whether or not the ratio of maximum density to periapsis density exceeds 1.4. The observed series of ratios show that the black box's output changes significantly from one orbit to the next. Therefore the inputs on which the black box's output depends must also change significantly from one orbit to the next. Periapsis latitude and periapsis LST, for example, do not change significantly from one orbit to the next. Only two of the many characteristics that define an aerobraking pass change significantly from one orbit to the next — time (UTC, not LST) and longitude.

If a travelling wave is responsible for this behaviour, then we would expect to find orbits with high ratios of maximum density to periapsis density occuring preferentially at certain "adjusted longitudes", where adjusted longitude = periapsis longitude - 360° $(t - t_0)/T$, t

is time since arbitrary time t_0, and T is the travelling wave's period. A range of periods from -20 to +20 days was tested, but results were inconclusive (Wilson et al., 2002).

5. Science — Tides in Constant Altitude Data

5.1. Tides in ODY Data

Thermal tides were responsible for zonal variations in MGS density measurements at fixed latitude, season, altitude and LST (Withers, 2003; Withers et al., 2003). Zonal density variations attributable to thermal tides are also present in ODY density measurements. "Dayside" corresponds to 12 hours $<$ LST $<$ 24 hours and "nightside" corresponds to 0 hours $<$ LST $<$ 12 hours.

Figure 56 shows outbound dayside densities at 130 km between 60°N and 70°N. There is clearly a strong influence of longitude on density. Figure 56 also shows a harmonic fit to the density measurements. Fitted parameters are listed in Table 8. The fitting procedure is described in Section 5.3.

[FIGURE 56] [TABLE 8]

The zonal structure persists over a broad altitude range. Figure 57 shows outbound dayside densities at 120, 130 and 140 km between 60°N and 70°N. The longitudes of peaks and troughs do not change significantly with altitude, indicating that the phases of the dominant tidal modes do not change significantly with altitude at these altitudes. Zonal mean density decreases as altitude increases, as do the relative amplitudes of the peaks and troughs in density. Similar trends were present in the MGS observations (Withers, 2003; Withers et al., 2003).

[FIGURE 57]

Figure 58 shows nightside inbound densities at 110, 120 and 130 km between 60°N and 70°N. Fitted parameters from 130 km are listed in Table 8. In this case, nightside zonal mean densities are about half the corresponding dayside values. Relative amplitudes of the zonal structure are also smaller on the nightside than the dayside.

[FIGURE 58]

Meridional trends in the zonal structure are most apparent in the nightside data, despite the zonal structure being stronger on the dayside, because the meridional extent of the nightside data is much greater than that of the dayside data. Figure 59 shows the zonal structure as a function of latitude for inbound densities at 120 km on the nightside. The zonal structure is coherent over substantial meridional distances, as seen in dayside MGS data (Withers, 2003; Withers et al., 2003). The longitudes of some density peaks and troughs change significantly more than others, whereas longitudes of all density peaks and troughs were relatively uniform in dayside MGS data (Withers, 2003; Withers et al., 2003). The strength of the zonal structure at 120 km appears to increase from pole to equator. However, this trend is not observed at 130 km. There are theoretical reasons to expect weaker zonal structure at the poles than at the equator, and suggestions of a similar trend in dayside MGS data (Withers et al., 2003, and references therein).

[FIGURE 59]

Section 5.3 defines the amplitude and phase of each harmonic term. The phase of the wave-n harmonic is between zero and 360°E/n by definition. Figure 60 shows phases of each term in Figure 59's harmonic fit. Phases are not randomly distributed, as expected for zonal structure that is coherent over an extended meridional range. Phases for wave-2 and wave-3 do not vary greatly with latitude. In fact, the wave-2 phase is always between 0°E and 35°E, 20% of its full range. The wave-3 phases varies almost monotonically between 15°E at 70°N–80°N and 65°E at 10°N–20°N. Although phases for wave-1 and wave-4 in a given latitude band are generally similar to their values in adjacent latitude bands, their values vary within their full ranges. The wave-1 and wave-4 phases are positively correlated, which may indicate a physical connection of some kind.

[FIGURE 60]

Figure 61 shows relative amplitudes of each term in Figure 59's harmonic fit. Amplitudes are more variable than the phases. Amplitudes of the wave-2 and wave-3 terms are generally largest.

[FIGURE 61]

These trends in ODY phases and amplitudes are generally consistent with analysis of dayside MGS data. Future analysis of the numerical values of the stable phases may be productive.

Simultaneous day/night measurements at the same latitude and altitude were made by ODY for a short period. On orbit 127, ODY made observations at 130 km at 75.7°N, 16.5 hr *and* 75.5°N, 2.5 hr. We now compare the zonal structure at 130 km between 70°N and 80°N on the dayside (outbound, orbits 96–146, LST 16.44–16.68 hrs) and on the nightside (inbound, orbits 109–151, LST 2.25–2.67 hrs). Results are shown in Figures 62 and 63 and in Table 9. The nightside's zonal structure is weak, if not non-existent. The dayside's zonal structure is slightly more significant. By contrast, zonal structure at 130 km between 50°S and 70°S during MGS Phase 2 was present on the dayside and stronger on the nightside.

[FIGURE 62] [FIGURE 63] [TABLE 9]

5.2. Tides in MGS Phase 1 Data

Neither Withers et al. (2003) nor Withers (2003) discussed MGS Phase 1 data. Keating et al. (1998) fitted wave-1 and wave-2 components to 21 densities at 125 km from orbits 90 to 110. Here we investigate tides in the MGS Phase 1 data in more detail, focusing on outbound data at 130 km which give the clearest results. Data before orbit 70 was neglected, because data at 130 km from orbits 1–70 are insufficient to sample all longitudes. Data from orbits 70–100, 80–110, 90–120, . . ., 170–200 were fitted. Overlapping intervals were used for ease of analysis. Figure 64 shows density as a function of longitude for orbits 130–160. The zonal structure is readily apparent and obviously dominated by wavenumber 2. Figure 65 shows that wavenumber 2 is stronger than wavenumber 1, which is stronger than wavenumber 3, which is stronger than wavenumber 4. Figure 66 shows that all phases change slowly during MGS Phase 1. Similar analysis at higher altitudes shows that the zonal structure is less apparent and its amplitudes and phases are more variable at higher altitudes than at 130 km.

[FIGURE 64] [FIGURE 65] [FIGURE 66]

Wavenumber 2 is important in the dayside zonal structure for both MGS Phase 1 and MGS Phase 2. Wavenumber 1 is stronger than wavenumber 3 in the MGS Phase 1 data, but weaker in MGS Phase 2 data. Seasonal changes in the atmosphere below 130 km are probably responsible for this difference.

5.3. Harmonic fit to zonal structure

Harmonic fits to zonal structure are performed using the same techniques as Withers et al. (2003). These techniques are also discussed in Withers (2003). Density as a function of longitude is fitted to this function:

$$\rho = a_0 + a_1 \cos(\lambda) + b_1 \sin(\lambda) + \cdots + a_k \cos(k\lambda) + b_k \sin(k\lambda) \tag{23}$$

Where ρ is density, λ is east longitude, and the a_i and b_i are model parameters. This is a wave-k model as it contains wavenumbers up to and including k. Measurement uncertainties are not used in the fitting procedure because the sol-to-sol atmospheric variability is typically much greater than the measurement uncertainties. With the above assumption about dealing with uncertainties, m density measurements, and n model parameters, the process follows Equation 7.18 of Neter and Wasserman (1974):

$$\underline{Y} = \underline{\underline{X}}\,\underline{p} + \underline{\epsilon} \tag{24}$$

Where $\underline{Y}$ is an m-element vector of density observations, $\underline{\underline{X}}$ is an m-by-n matrix, $\underline{p}$ is an n-element vector of model parameters, and $\underline{\epsilon}$ is an n-element vector of uncorrelated random variables of mean 0 and standard deviation σ.

Using the fitting function in Equation 23:

$$\begin{aligned} X_{i0} &= 1 \\ X_{i1} &= \cos\left(\lambda_i\right) \\ X_{i2} &= \sin\left(\lambda_i\right) \\ &\vdots \\ X_{in-2} &= \cos\left(\frac{(n-1)\lambda_i}{2}\right) \\ X_{in-1} &= \sin\left(\frac{(n-1)\lambda_i}{2}\right) \end{aligned} \tag{25}$$

$$\begin{aligned} p_0 &= a_0 \\ p_1 &= a_1 \\ p_2 &= b_1 \\ &\vdots \\ p_{n-2} &= a_{\frac{n-1}{2}} \\ p_{n-1} &= b_{\frac{n-1}{2}} \end{aligned} \tag{26}$$

The index i labels an individual density measurement. The n variables $(1, \cos(\lambda), \sin(\lambda), \ldots)$ being fitted are linearly independent. The least squares solution for the model parameters, $\underline{p}$, follows Equation 7.21 of Neter and Wasserman (1974):

$$\underline{p} = \left(\underline{\underline{X}}^T \underline{\underline{X}}\right)^{-1} \underline{\underline{X}}^T \underline{Y} \tag{27}$$

Where a superscript T indicates the transpose of a matrix and the superscript -1 indicates the inverse of a matrix. Note that the constant density term, a_0 or p_0, is not formally identical to the mean density. Hence it is referred to as the constant density term rather than as the zonal mean term. However, the two are usually similar.

The model predictions, $\underline{\hat{Y}}$, for atmospheric densities at the longitudes at which measurements have been made follow Equation 7.23 of Neter and Wasserman (1974):

$$\underline{\hat{Y}} = \underline{\underline{X}}\, \underline{p} \tag{28}$$

The covariance matrix for $\underline{p}$ follows Equation 7.39 of Neter and Wasserman (1974):

$$\underline{\underline{Cov}}\left(\underline{p}\right) = \frac{\left(\underline{\hat{Y}} - \underline{Y}\right)^T \left(\underline{\hat{Y}} - \underline{Y}\right)}{m - n} \left(\underline{\underline{X}}^T \underline{\underline{X}}\right)^{-1} \tag{29}$$

1 σ uncertainties in the model parameters are given by:

$$\sigma_{p_j} = Cov_{jj} \tag{30}$$

Using sine and cosine terms is useful for forming a linear model. However, it is more useful to interpret paired sine and cosine terms as being a single sinusoid with an amplitude and a phase. The phase of a given harmonic can be defined as the longitude of its first peak east of 0°. Thus the phase of the wave-q harmonic must lie between 0° and 360°E/q where q labels a certain harmonic.

$$a_q \ \cos\left(q\lambda\right) + b_q \ \sin\left(q\lambda\right) = R_q \ \cos\left(q\left[\lambda - \alpha_q\right]\right) \tag{31}$$

Where R_q is the amplitude of the qth harmonic and α_q is the phase of the qth harmonic. Note that Withers (2003) incorrectly call $q\alpha_q$ the phase of the qth harmonic. Trigonometry yields the following solutions for R_q and α_q in terms of a_q and b_q.

$$R_q = \left(a_q^2 + b_q^2\right)^{1/2} \tag{32}$$

$$\alpha_q = \frac{1}{q} \tan^{-1}\left(b_q / a_q\right) \tag{33}$$

Using the usual formula, Equation 4.9 of Bevington (1969), for transforming uncertainties of uncorrelated variables:

$$\sigma^2_{R_q} = \sigma^2_{a_q} \left(\frac{\partial R_q}{\partial a_q} \right)^2 + \sigma^2_{b_q} \left(\frac{\partial R_q}{\partial b_q} \right)^2 \tag{34}$$

$$\sigma^2_{\alpha_q} = \sigma^2_{a_q} \left(\frac{\partial \alpha_q}{\partial a_q} \right)^2 + \sigma^2_{b_q} \left(\frac{\partial \alpha_q}{\partial b_q} \right)^2 \tag{35}$$

$$\sigma^2_{R_q} = \sigma^2_{a_q} \left(\frac{a_q}{R_q} \right)^2 + \sigma^2_{b_q} \left(\frac{b_q}{R_q} \right)^2 \tag{36}$$

$$\sigma^2_{\alpha_q} = \frac{b_q^2 \sigma^2_{a_q} + a_q^2 \sigma^2_{b_q}}{q^2 \left(a_q^2 + b_q^2 \right)^2} \tag{37}$$

A phase of $3^\circ \pm 15^\circ$ is a perfectly reasonable and meaningful result. An amplitude of 3 kg km^{-3} $\pm$ 15 kg km^{-3} means that the harmonic is not present in any statistically significant sense and that its corresponding phase is meaningless.

It is often useful to normalize the zonally-varying terms in each wavefit (R_q) by their constant density term (R_0). This facilitates a comparison of the strength of the zonal structure between different seasons or altitudes. The symbol R_q^N labels normalized harmonic amplitudes.

$$R_q^N = \frac{R_q}{R_0} \tag{38}$$

$$\sigma^2_{R_q^N} = \sigma^2_{R_q} \left(\frac{\partial R_q^N}{\partial R_q} \right)^2 + \sigma^2_{R_0} \left(\frac{\partial R_q^N}{\partial R_0} \right)^2 \tag{39}$$

$$\sigma^2_{R_q^N} = \frac{R_q^2 \, \sigma^2_{R_0}}{R_0^4} + \frac{\sigma^2_{R_q}}{R_0^2} \tag{40}$$

A 1 σ uncertainty about the fitted function can be calculated at any given longitude following Equation 7.54a of Neter and Wasserman (1974):

$$\sigma^2_{fit} = \left(1 + \underline{X}^T_{new} \left(\underline{\underline{X}}^T \underline{\underline{X}} \right)^{-1} \underline{X}_{new} \right) \frac{\left(\underline{\hat{Y}} - \underline{Y} \right)^T \left(\underline{\hat{Y}} - \underline{Y} \right)}{m - n} \tag{41}$$

where $\underline{X}_{new}$ is an n-element vector whose elements are calculated identically to those of a single column of $\underline{\underline{X}}$, as in Equation 25. The longitude used to calculate $\underline{X}_{new}$ is that at which the 1 σ uncertainty is desired. Formally, this is the 1 σ uncertainty on what a new observation at that longitude might be. The predicted value of that observation is as in Equation 28.

6. Science — Other Aspects of Constant Altitude Data

6.1. Comparison of results to predictions

The Mars Thermospheric General Circulation Model (MTGCM) has predicted the state of the atmosphere under conditions appropriate for ODY aerobraking (Bougher et al., 1999; Bougher et al., 2000; Bougher et al., 2002). Results from eight MTGCM simulations have been made available online at http://aoss-research.engin.umich.edu/tgcm_planets_archive/predms01.html and are summarized in

Table 10. Dust opacities (τ) of 0.3, 1.0 and 3.0 were simulated. Altitude ranges are 100–150 km or better and vertical resolutions are 5 km or better. Results are available at LSTs of 3, 4, 15, 16, 17 and 18 hours. Results at LST=4 hours and LST=15 hours were not used because, apart from a small region near the pole, all data have either LST<3 hours or LST>16 hours. The simulated latitudes, altitudes, local solar times and seasons almost completely cover the range of conditions in the ODY dataset. Additional simulations at equatorial latitudes at $L_s \approx 297°$ and nightside LSTs would have been useful.

[TABLE 10]

ODY and MTGCM dayside densities are compared in Figure 67. Multiple MTGCM dayside densities are plotted for a single latitude and altitude. These correspond to different LSTs (16, 17 and 18 hours), dust opacities (τ = 0.3, 1.0 and 3.0) and seasons (L_s = 256°, 277° and 297°). Dust opacity is responsible for most of the range in density at fixed latitude and altitude. This is why the multiple MTGCM densities at, say, 57.5°N and 100 km form three distinct clusters. There are only two clusters at 87.5°N and 100 km because simulated densities are available at only two dust opacities. Observed and simulated densities are very consistent. Simulations at $\tau = 1.0$ appear most consistent with observations.

[FIGURE 67]

ODY and MTGCM nightside densities are compared in Figure 68. Simulated densities are available at only two dust opacities (τ=0.3 and 1.0). Observed polar densities are consistent with simulations at τ=1.0. Observed mid-latitude densities are significantly smaller than simulated densities. Densities equatorward of 70°N do not vary with latitude, in constrast to the strong meridional density gradient in simulations, which may indicate difference between simulated and actual dynamics.

[FIGURE 68]

ODY and MTGCM dayside scale heights are compared in Figure 69. Densities at different altitudes are clearly distinct, but scale heights are not. Therefore the large filled circles indicate an average of all scale height measurements within a ten degree latitude window. Altitude is indicated by the colour of the filled circle. Observed scale heights at 110 km are about a factor of two greater than predicted. Equatorward of 80°N, observed scale heights at 120 and 130 km are consistent with predictions. Observations poleward of 80°N show that the scale height decreases as altitude increases, opposite to the predicted increase in scale height with increasing altitude. However, it is important to note that the observed scale heights are derived from non-vertical density profiles.

[FIGURE 69]

ODY and MTGCM nightside scale heights are compared in Figure 70. Observations and simulations are reasonably consistent, especially equatorward of 70°N. Observed scale heights are somewhat greater than predicted poleward of 70°N (Bougher et al., 2006). Both observations and simulations show that scale heights (and, by implication, temperatures) increase poleward of about 70°N. Observations show the scale height decreasing as altitude increases, whereas simulations show a more uniform scale height.

[FIGURE 70]

6.2. Variations with Latitude and LST

Figure 71 shows mean dayside and nightside densities for a range of latitudes and altitudes. Differences between nightside and dayside densities increase as altitude increases and as latitude moves from pole to equator. ODY data were obtained around northern winter solstice, when northern polar regions are not illuminated by the Sun. It is therefore reasonable that nightside and dayside densities are similar during the polar night.

[FIGURE 71]

Figure 72 shows a similar plot for scale heights. Scale heights are greater in the polar region than at tropical and mid-latitudes. Dayside scale heights are greater than nightside scale heights. Nightside scale heights at 120 and 130 km do not vary significantly with latitude equatorward of 60°N. Nightside mid-latitude scale heights at 130 km are slightly greater than at 120 km. A very different picture is presented by analysis of MGS dayside scale heights (Withers, 2006). Scale heights are greater in the tropics in MGS data than in polar regions. Scale heights vary significantly with latitude equatorward of 60° in MGS data.

[FIGURE 72]

6.3. Interannual Variability

There are no instances where ODY and MGS data were obtained at different years, but identical latitudes, LSTs and seasons.

ODY and MGS data were obtained at similar latitudes and seasons, but dissimilar LSTs. MGS measured densities at 130 km, 55°N–60°N, LST=12.0-12.8 hrs, Ls=270°–285° in February 1998. ODY measured densities at 130 km at 130 km, 62°N–70°N, LST=16.4-18.0 hrs, Ls=263°–288° in November 2001. There is a difference of 6 hours in LST. The mean density was 2.64 kg km^{-3} for ODY and 3.25 kg km^{-3} for MGS. The mean density scale height was 7.1 km for ODY and 7.6 km for MGS.

7. Conclusions

Density profiles, as well as constant altitude densities and density scale heights, have been generated from Odyssey (ODY) accelerometer measurements. These form a more complete dataset than the unpeer-reviewed data products currently available from the Planetary Data System (PDS). They will be archived at the PDS in compliant formats with extensive documentation.

Small-scale structure, probably due to gravity waves, is present in ODY density profiles. Its amplitudes and meridional trends are broadly consistent with those seen in MGS density profiles. Only one ODY density profile, P056, contains a sudden change in density comparable to those present in MGS density profiles. The previously-observed increase in temperature with latitude near the north polar region during winter is not zonally-uniform, which suggests that dynamics plays a major role in maintaining the high temperatures.

Thermal tides produce zonal variations in atmospheric densities during ODY aerobraking, as previously observed during MGS aerobraking. Tidal effects persist from 120 km to 140 km, with amplitudes, but not phases, changing significantly with altitude. Zonal structure is weaker on the nightside than on the dayside. The zonal structure is coherent over 60 degrees of latitude, although it is less stable for ODY than for MGS.

Atmospheric simulations produced in support for ODY aerobraking can now be compared to data. Predicted dayside densities were accurate. The predicted strong meridional gradient in nightside densities was not observed. Simulations did not predict changes in scale height with altitude well. These discrepancies can be used to investigate which model boundary conditions were inadequate or which representations of physical processes were incomplete.

Acknowledgments

We gratefully acknowledge the Odyssey operations team for safely guiding Odyssey through its aerobraking phase; Bob Mase, Jill Prince and their NASA colleagues for providing mass, aerodynamics and orientation information to us; Steve Bougher for making MTGCM simulations publicly available; and the Odyssey aerobraking team, led by Gerry Keating, for making raw data available to the PDS. Partial support for PW's activities was provided by the Odyssey Participating Scientist Program.

REFERENCES

Baird, D. T., Tolson, R., Bougher, S., Steers, B., 2007. Zonal wind calculations from Mars Global Surveyor Accelerometer and rate data. J. Spacecraft Rockets 44, 1180–1187.

Bevington, P. R., 1969. *Data reduction and error analysis for the physical sciences* (1st ed.). Cambridge University Press, New York.

Bougher, S., Engel, S., Roble, R. G., Foster, B., 1999. Comparative terrestrial planet thermospheres 2. Solar cycle variation of global structure and winds at equinox. J. Geophys. Res. 104, 16591–16611.

Bougher, S. W., Bell, J. M., Murphy, J. R., Lopez-Valverde, M. A., Withers, P. G., 2006. Polar warming in the Mars thermosphere: Seasonal variations owing to changing insolation and dust distributions. Geophys. Res. Lett. 33, L02203, 10.1029/2005GL024059.

Bougher, S. W., Engel, S., Roble, R. G., Foster, B., 2000. Comparative terrestrial planet thermospheres 3. Solar cycle variation of global structure and winds at solstices. J. Geophys. Res. 105, 17669–17692.

Bougher, S. W., Roble, R. G., Fuller-Rowell, T., 2002. Simulations of the upper atmospheres of the terrestrial planets. In: Mendillo, M., Nagy, A. F., Waite, J. H. (Eds.), Atmospheres in the solar system: comparative aeronomy, Volume 130 of *Geophys. Monogr. Ser.* American Geophysical Union, Washington, D.C., pp. 261–288.

Cancro, G. J., Keating, G. M., Tolson, R. H., 1998. Operational data reduction procedure for determining density and vertical structure of the martian upper atmosphere from Mars Global Surveyor Accelerometer measurements, also NASA/CR-998-208721. Master's thesis, Joint Institute for Advanced Flight Studies, George Washington University and NASA Langley Research Center.

Chavis, Z., Wilmoth, R., 2005. Plume modeling and application to Mars 2001 Odyssey aerobraking. J. Spacecraft Rockets 42, 450–456.

CreaseyA, J. E., Forbes, J. M., Keating, G. M., 2006. Density variability at scales typical of gravity waves observed in Mars' thermosphere by the MGS accelerometer. Geophys. Res. Lett. 33, L22814, 10.1029/2006GL027583.

CreaseyB, J. E., Forbes, J. M., Hinson, D. P., 2006. Global and seasonal distribution of gravity wave activity in Mars' lower atmosphere derived from MGS radio occultation data. Geophys. Res. Lett. 33, L01803, 10.1029/2005GL024037.

Crowley, G., Tolson, R. H., 2007. Mars thermospheric winds from Mars Global Surveyor and Mars Odyssey Accelerometers. J. Spacecraft Rockets 44, 1188–1194.

Fritts, D. C., Wang, L., Tolson, R. H., 2006. Mean and gravity wave structures and variability in the Mars upper atmosphere inferred from Mars Global Surveyor and Mars Odyssey aerobraking densities. J. Geophys. Res. 111, A12304, 10.1029/2006JA011897.

Keating, G. M., Bougher, S. W., Zurek, R. W., Tolson, R. H., Cancro, G. J., Noll, S. N., Parker, J. S., Schellenberg, T. J., Shane, R. W., Wilkerson, B. L., Murphy, J. R., Hollingsworth, J. L., Haberle, R. M., Joshi, M., Pearl, J. C., Conrath, B. J., Smith, M. D., Clancy, R. T., Blanchard, R. C., Wilmoth, R. G., Rault, D. F., Martin, T. Z., Lyons, D. T., Esposito, P. B., Johnston, M. D., Whetzel, C. W., Justus, C. G., Babicke, J. M., 1998. The structure of the upper atmosphere of Mars: In situ Accelerometer measurements from Mars Global Surveyor. Science 279, 1672–1676.

Magalhães, J. A., Schofield, J. T., Seiff, A., 1999. Results of the Mars Pathfinder atmospheric structure investigation. J. Geophys. Res. 104, 8943–8956.

Martin, T. Z., Murphy, J. R., 2001. A martian year of mapping by the MGS Horizon Science Experiment. Division for Planetary Sciences Meeting, Abstract 19.24.

Mase, R., 2005. Introduction: 2001 Mars Odyssey mission. J. Spacecraft Rockets 42, 385–385.

Mase, R., Burkhart, D., 2000. *Navigation small forces verification*. JPL document IOM-MARS01:NAV-01-005, 4 March 2000 (possibly 2001).

NAIF, 2008a. *ftp://naif.jpl.nasa.gov/pub/naif/M01/kernels/*.

NAIF, 2008b. *ftp://naif.jpl.nasa.gov/pub/naif/M01/kernels/fk/m01_v28.tf*.

Neter, J., Wasserman, W., 1974. *Applied linear statistical models*. Richard D. Irwin, Homewood, Illinois, USA.

Owen, T., 1992. The composition and early history of the atmosphere of Mars. In: Kieffer, H. H., Jakosky, B. M., Snyder, C. W., Matthews, M. S. (Eds.), Mars. University of Arizona Press, pp. 818–834.

Smith, D. E., Neumann, G., Arvidson, R. A., Guinness, E. A., Slavney, S., 2003. *Mars Global Surveyor Laser Altimeter Mission Experiment Gridded Data Record*. NASA Planetary Data System, MGS-M-MOLA-5-MEGDR-L3-V1.0, http://pds-geosciences.wustl.edu/geo/mgs-m-mola-5-megdr-l3-v1/mgsl_300x/meg004/.

Smith, J. C., Bell, J., 2005. 2001 Mars Odyssey aerobraking. J. Spacecraft Rockets 42, 406–415.

Spencer, D. A., Tolson, R., 2007. Aerobraking cost and risk decisions. J. Spacecraft Rockets 44, 1285–1293.

Takashima, N., 2002. *Attitude angles for Mars Odyssey*. Unpublished NASA Langley Research Center memorandum dated 13 May 2002 and supplied by Jill Prince.

Takashima, N., Wilmoth, R. G., 2002. Aerodynamics of Mars Odyssey. In: American Institute of Aeronautics and Astronautics paper 2002-4809, AIAA Atmospheric Flight Mechanics Conference and Exhibit, 5–8 August 2002, Monterey, California, USA.

Tolson, R. H., Dwyer, A. M., Hanna, J. L., Keating, G. M., George, B. E., Escalera, P. E., Werner, M. R., 2005. Application of accelerometer data to Mars Odyssey aerobraking and atmospheric modeling. J. Spacecraft Rockets 42, 435–443.

Tolson, R. H., Keating, G. M., Zurek, R. W., Bougher, S. W., Justus, C. G., Fritts, D. C., 2007. Application of accelerometer data to atmospheric modeling during Mars aerobraking operations. J. Spacecraft Rockets 44, 1172–1179.

Tyler, G. L., Balmino, G., Hinson, D. P., Sjogren, W. L., Smith, D. E., Woo, R., Armstrong, J. W., Flasar, F. M., Simpson, R. A., Priest, P., 2000. PDS volume MORS_1006. In: MGS-M-RSS-5-SDP-V1.0, NASA Planetary Data System.

Wang, L., Fritts, D. C., Tolson, R. H., 2006. Nonmigrating tides inferred from the Mars Odyssey and Mars Global Surveyor aerobraking data. Geophys. Res. Lett. 33, L23201, 10.1029/2006GL027753.

Wilson, R. J., Banfield, D., Conrath, B. J., Smith, M. D., 2002. Traveling waves in the northern hemisphere of Mars. Geophys. Res. Lett. 29, 1684, 10.1029/2002GL014866.

Withers, P., 2003. *Tides in the Martian atmosphere — and other topics.* Ph. D. thesis, University of Arizona.

Withers, P., 2006. Mars Global Surveyor and Mars Odyssey Accelerometer observations of the martian upper atmosphere during aerobraking. Geophys. Res. Lett. 33, L02201, 10.1029/2005GL024447.

Withers, P., Bougher, S. W., Keating, G. M., 2003. The effects of topographically-controlled thermal tides in the martian upper atmosphere as seen by the MGS accelerometer. Icarus 164, 14–32.

Withers, P., Towner, M. C., Hathi, B., Zarnecki, J. C., 2003. Analysis of entry accelerometer data: A case study of Mars Pathfinder. Planet. Space Sci. 51, 541–561.

This manuscript was prepared with the AAS LATEX macros v4.0.

Table 1. Mean noise in high-rate acceleration measurements

Acceleration	Orbits	Noise (m s^{-2})
$a_{aero,hi,y}$	1–136	8.601×10^{-5}
	137–268	2.824×10^{-4}
	269–330	5.200×10^{-4}
$a_{aero,hi,y,7}$	1–136	1.824×10^{-5}
	137–268	5.168×10^{-5}
	269–330	7.960×10^{-5}
$a_{aero,hi,y,39}$	1–136	4.655×10^{-6}
	137–268	8.663×10^{-6}
	269–330	1.262×10^{-5}

Table 2. Ratios of mean noise in high-rate acceleration measurements

Orbits	$a_{aero,hi,y,1}$:$a_{aero,hi,y,7}$	$a_{aero,hi,y,1}$:$a_{aero,hi,y,39}$	$a_{aero,hi,y,7}$:$a_{aero,hi,y,39}$
1–136	4.71	18.48	3.92
137–268	2.34	5.71	2.44
269–330	2.56	6.42	2.51
Expected ratio for $\sqrt{N}$	$\sqrt{7} = 2.65$	$\sqrt{39} = 6.25$	$\sqrt{39/7} = 2.36$

Table 3. Some characteristics of derived high-rate density profiles.

	$\rho_{hi,39}$	$\rho_{hi,7}$	ρ_{hi}
Start of Aerobraking			
z_{max} (km)	146	145	142
σ_ρ at z_{max} (kg km^{-3})	0.4	0.4	0.6
$\sigma_{aaero,y}$ at z_{max} (m s^{-2})	2×10^{-4}	2×10^{-4}	2×10^{-4}
End of Aerobraking			
z_{max} (km)	134	132	122
σ_ρ at z_{max} (kg km^{-3})	0.6	0.8	4
$\sigma_{aaero,y}$ at z_{max} (m s^{-2})	2×10^{-4}	2×10^{-4}	1.3×10^{-3}

Table 4. Constant altitude data products for orbit P076. Uncertainties are 1σ.

Altitude (km)	Density (kg km^{-3})	Scale Height (km)
Inbound		
110	17.56±0.10	8.24±0.12
120	4.47±0.08	6.72±0.25
130	1.10±0.08	7.37±1.30
Outbound		
110	21.23±0.12	10.30±0.19
120	7.44±0.09	8.64±0.28
130	1.98±0.08	7.30±0.72

Table 5. Coverage of constant altitude data.

Altitude (km)	Number of orbits	First orbit	Last orbit
Inbound			
100	37	95	146
110	173	46	255
120	316	13	335
130	255	11	336
140	6	7	32
150	0	—	—
160	0	—	—
Outbound			
100	37	95	146
110	173	46	255
120	316	13	335
130	280	11	336
140	77	7	158
150	3	16	29
160	0	—	—

Table 6. Typical uncertainties in constant altitude data

Altitude (km)	σ_ρ (kg km^{-3})	σ_H (km)	σ_T (K)
Inbound			
100	0.155	0.14	2.5
110	0.100	0.18	3.3
120	0.076	0.28	5.1
130	0.084	1.36	24.5
140	0.083	2.00	35.9
150	—	—	—
160	—	—	—
Outbound			
100	0.176	0.51	9.3
110	0.104	0.33	6.0
120	0.078	0.34	6.1
130	0.083	1.32	23.7
140	0.089	3.01	53.9
150	0.095	5.07	90.4
160	—	—	—

Table 7. Mean and standard deviation of the relative differences between our results and the aerobraking team's results

Altitude (km)	Mean	Standard deviation
Density		
Inbound 110	0.06	0.05
Outbound 110	0.05	0.10
Inbound 120	0.10	0.07
Outbound 120	0.09	0.09
Density Scale Height		
Inbound 110	0.08	0.19
Outbound 110	0.11	0.36
Inbound 120	0.05	0.13
Outbound 120	0.08	0.18
Outbound 110[1]	0.09	0.21

[1]Not including orbit P122 (Figures 43 and 46)

Table 8. Model fit parameters for ODY densities measured at 130 km between 60°N and 70°N. Uncertainties are 1σ.

Parameters	Dayside (outbound)	Nightside (inbound)
Constant Amplitude (kg km^{-3})	2.755 ± 0.119	1.171 ± 0.039
Normalised Wave 1 Amplitude	0.099 ± 0.063	0.076 ± 0.048
Normalised Wave 2 Amplitude	0.178 ± 0.062	0.128 ± 0.048
Normalised Wave 3 Amplitude	0.271 ± 0.064	0.172 ± 0.052
Normalised Wave 4 Amplitude	0.122 ± 0.062	0.122 ± 0.059
Wave 1 Phase (degrees)	89.9 ± 35.2	220.9 ± 36.3
Wave 2 Phase (degrees)	166.4 ± 9.9	29.1 ± 10.5
Wave 3 Phase (degrees)	34.8 ± 4.2	30.5 ± 5.7
Wave 4 Phase (degrees)	81.4 ± 7.1	17.8 ± 5.5

Table 9. Model fit parameters for ODY densities measured at 130 km between 70°N and 80°N. Uncertainties are 1σ.

Parameters	Dayside (outbound)	Nightside (inbound)
Constant Amplitude (kg km^{-3})	1.829 ± 0.085	1.173 ± 0.036
Normalised Wave 1 Amplitude	0.135 ± 0.066	0.069 ± 0.043
Normalised Wave 2 Amplitude	0.126 ± 0.062	0.056 ± 0.045
Normalised Wave 3 Amplitude	0.047 ± 0.068	0.051 ± 0.044
Normalised Wave 4 Amplitude	0.177 ± 0.068	0.042 ± 0.054
Wave 1 Phase (degrees)	159.7 ± 27.9	255.7 ± 36.9
Wave 2 Phase (degrees)	171.8 ± 16.6	170.5 ± 23.8
Wave 3 Phase (degrees)	41.2 ± 27.4	9.7 ± 17.7
Wave 4 Phase (degrees)	82.2 ± 5.5	58.0 ± 15.5

Table 10. MTGCM Simulations.

Label	Run date	τ	L_s (°)	Date	Latitudes	LSTs
MS01OCC.AB2	09/10/01	1.0	256	21 Oct 2001	57.5, 67.5, 77.5	17, 18
MS01OCD.AB2	09/24/01	3.0	256	21 Oct 2001	57.5, 67.5, 77.5	17, 18
MS01NVC.AB2	10/23/01	1.0	277	23 Nov 2001	67.5, 77.5, 87.5	15, 16
MS01DCC.AB2	10/23/01	1.0	297	25 Dec 2001	37.5, 47.5, 57.5	3, 4
					67.5, 77.5, 87.5	3, 4
Nov23t03	01/25/00	0.3	277	23 Nov 2001	47.5, 57.5, 67.5	3, 4
					77.5, 87.5	3, 4
					57.5, 67.5, 77.5	15, 16, 17
					87.5	15, 16, 17
Nov23t10	10/26/00	1.0	277	23 Nov 2001	47.5, 57.5, 67.5	3, 4
					77.5, 87.5	3, 4
					57.5, 67.5, 77.5	15, 16, 17
					87.5	15, 16, 17
Dec25t03	01/25/00	0.3	297	25 Dec 2001	47.5, 57.5, 67.5	3, 4
					77.5, 87.5	3, 4
					57.5, 67.5, 77.5	15, 16, 17
					87.5	15, 16, 17
Dec25t10	10/26/00	1.0	297	25 Dec 2001	47.5, 57.5, 67.5	3, 4
					77.5, 87.5	3, 4
					57.5, 67.5, 77.5	15, 16, 17
					87.5	15, 16, 17

Figure Captions

Figure 1: Pre-entry values of $a_{bias,hi,y}$ for each orbit that has high-rate data.

Figure 2: Post-exit values of $a_{bias,hi,y}$ for each orbit that has high-rate data.

Figure 3: Maximum values of $a_{aero,hi,y}$ (crosses) for each orbit that has high-rate data and $a_{aero,lo,y}$ (diamonds) for each orbit that has low-rate data only.

Figure 4: Noise in acceleration measurements. Noise in $a_{aero,hi,y}$ (black crosses), $a_{aero,hi,y,7}$ (black triangles) and $a_{aero,hi,y,39}$ (black squares) shown for each orbit that has high-rate data. Noise in $a_{aero,lo,y}$ (grey crosses), $a_{aero,lo,y,7}$ (grey triangles) and $a_{aero,lo,y,39}$ (grey squares) shown for each orbit that has low-rate data only. The effects of using different sampling rates for orbits 1–136, 137–268 and 269–330 can be seen.

Figure 5: Time series of $a_{aero,hi,y}$, $a_{aero,hi,y,7}$ and $a_{aero,hi,y,39}$ for orbit P076. Plotted values of $a_{aero,hi,y,7}$ ($a_{aero,hi,y,39}$) have been increased from actual values by 0.01 (0.02) m s^{-2} for clarity.

Figure 6: Time series of $a_{aero,hi,y}$, $a_{aero,hi,y,7}$ and $a_{aero,hi,y,39}$ for orbit P076. The line with the largest maximum acceleration is $100 \times a_{aero,hi,y,39}$, the line with the second-largest maximum acceleration is $10 \times a_{aero,hi,y,7}$ and line with the third-largest maximum acceleration is $1 \times a_{aero,hi,y}$. The remaining line, whose value is 2×10^{-4} m s^{-2} at $\pm$150s, is the uncertainty in $a_{aero,hi,y}$. For orbits prior to P137, such as this one, the thruster limit of 2×10^{-4} m s^{-2} is greater than the noise level in $a_{aero,hi,y}$, $a_{aero,hi,y,7}$ and $a_{aero,hi,y,39}$, so uncertainties in $a_{aero,hi,y}$, $a_{aero,hi,y,7}$ and $a_{aero,hi,y,39}$ are identical. Note how $a_{aero,hi,y,39}$ covers a larger time interval than $a_{aero,hi,y,7}$, which in turn covers a larger time interval than $a_{aero,hi,y}$. This is due to the reduction in noise by averaging.

Figure 7: Mass of ODY during aerobraking.

Figure 8: ρC_y as a function of ρ for $u_x = 0$ and $u_z = 0$. Values from the aerodynamic database are marked by crosses and joined by dashed lines. The solid line indicates $\rho C_y = \rho$, or $C_y = 1$. Since ρC_y is a single-valued function of ρ, this figure can be used to find ρ from an observed value of ρC_y. As shown in Figure 9, $C_y \approx 2$.

Figure 9: C_y as a function of ρ for $u_x = 0$ and $u_z = 0$. Values from the aerodynamic database are marked by crosses and joined by dashed lines.

Figure 10: u_x as a function of time after periapsis for orbit P076.

Figure 11: u_z as a function of time after periapsis for orbit P076.

Figure 12: u_x and u_z for orbit P076. The dashed (solid) line indicates time before (after) periapsis. Values are plotted for times within 200 seconds of periapsis. Crosses mark values of u_x and u_z at -200s, -100s, 0s, 100s and 200s.

Figure 13: ϕ as a function of time after periapsis for orbit P076.

Figure 14: θ as a function of time after periapsis for orbit P076.

Figure 15: C_y as a function of time after periapsis for orbit P076. Values of C_y for $\rho_{hi,39}$, $\rho_{hi,7}$ and ρ_{hi} at a given time are similar, but not identical. The top line shows $C_y + 0.2$ for $\rho_{hi,39}$. The middle line shows $C_y + 0.1$ for $\rho_{hi,7}$. The bottom line shows C_y for ρ_{hi}.

Figure 16: Density on a linear scale as a function of time after periapsis for orbit P076. The top line shows $\rho_{hi,39} + 10$ kg km^{-3}. The middle line shows $\rho_{hi,7} + 5$ kg km^{-3}. The bottom line shows ρ_{hi}. Note how $\rho_{hi,39}$ covers a larger time interval than $\rho_{hi,7}$, which in turn covers a larger time interval than ρ_{hi}. This is due to the reduction in noise by averaging.

Figure 17: Density on a logarithmic scale as a function of time after periapsis for orbit P076. The top line shows $\rho_{hi,39} \times 100$. The next line shows $\rho_{hi,7} \times 10$. The next line shows ρ_{hi}. The bottom line shows the uncertainty in $\rho_{hi,39}$. Uncertainties in $\rho_{hi,7}$ and ρ_{hi} are very

similar, but slightly smoother.

Figure 18: $2 \times (p_{in} - p_{out}) / (p_{in} + p_{out})$ versus orbit number.

Figure 19: $2 \times (p_{in} - p_{out}) / (p_{in} + p_{out})$ versus periapsis latitude. Dayside (nightside) datapoints are indicated by + (X).

Figure 20: Pressure profiles (solid lines) for orbit P076. Pressures at a given altitude are greater on the outbound (equatorward) leg than on the inbound (poleward) leg. 1σ uncertainties are marked by the dashed lines. The horizontal solid line joining the inbound and outbound legs indicates the pressure discontinuity at periapsis.

Figure 21: Temperature profiles (solid lines) for orbit P076. Temperatures around 110 km are greater on the outbound (equatorward) leg than on the inbound (poleward) leg. 1σ uncertainties are marked by the dashed lines. The horizontal solid line joining the inbound and outbound legs indicates the temperature discontinuity at periapsis.

Figure 22: Temperature versus pressures for orbit P076. Temperatures at a given pressure are greater on the outbound (equatorward) leg than on the inbound (poleward) leg.

Figure 23: Difference in periapsis time between the results of this work and the aerobraking team's results as a function of orbit number.

Figure 24: As Figure 23, but for periapsis latitude.

Figure 25: As Figure 23, but for periapsis altitude (z).

Figure 26: As Figure 23, but for periapsis longitude.

Figure 27: As Figure 23, but for periapsis LST.

Figure 28: As Figure 23, but for periapsis solar zenith angle (SZA).

Figure 29: Difference in periapsis latitude between the results of this work and the aerobraking team's results as a function of this work's periapsis latitude. Both dayside and nightside differences are shown for periapsis latitudes poleward of about 67°N. Differences in periapsis latitude at a given periapsis latitude are only slightly dependent on whether datapoints come from the dayside or nightside.

Figure 30: Difference in periapsis altitude between the results of this work and the aerobraking team's results as a function of this work's periapsis latitude. Both dayside and nightside differences are shown for periapsis latitudes poleward of about 67°N. Differences in periapsis altitude at a given periapsis latitude are independent of whether datapoints come from the dayside or nightside.

Figure 31: Difference in periapsis time between the results of this work and the aerobraking team's results as a function of this work's periapsis latitude (black symbols). Results from dayside periapses are multiplied by -1 and plotted again (grey symbols). The unadjusted nightside differences and the adjusted dayside differences are very similar at any given periapsis latitude.

Figure 32: As Figure 31, but for periapsis longitude.

Figure 33: As Figure 31, but for periapsis LST.

Figure 34: As Figure 31, but for periapsis solar zenith angle (SZA).

Figure 35: Difference in redefined periapsis latitude as a function of this work's periapsis latitude. Dayside and nightside differences poleward of about 67°N appear indistinguishable. Differences in this Figure are much smaller than differences in Figure 29.

Figure 36: As Figure 31, but for periapsis altitude. Differences in this Figure are much smaller than differences in Figure 30.

Figure 37: Q as a function of periapsis latitude for our results (black crosses) and the aerobraking team's results (grey diamonds).

Figure 38: Relative difference in inbound density at 110 km as a function of orbit number.

Figure 39: As Figure 38, but for outbound density at 110 km.

Figure 40: As Figure 38, but for inbound density at 120 km.

Figure 41: As Figure 38, but for outbound density at 120 km.

Figure 42: As Figure 38, but for inbound density scale height at 110 km.

Figure 43: As Figure 38, but for outbound density scale height at 110 km.

Figure 44: As Figure 38, but for inbound density scale height at 120 km.

Figure 45: As Figure 38, but for outbound density scale height at 120 km.

Figure 46: Density profile ($\rho_{hi,39}$) for orbit P122 (dashed line). Black solid line shows extrapolation based on fitted outbound density and density scale height at 110 km using our results. Grey solid line shows extrapolation based on fitted outbound density and density scale height at 110 km using the aerobraking team's results.

Figure 47: Density profile ($\rho_{hi,39}$) for orbit P081 (dashed line). Black solid line shows extrapolation based on fitted inbound density and density scale height at 110 km using our results. Grey solid line shows extrapolation based on fitted inbound density and density scale height at 110 km using the aerobraking team's results.

Figure 48: Density profiles from orbit P011. Both $\rho_{hi,7}$ (solid line) and $\rho_{hi,39}$ (dashed line) are shown.

Figure 49: Measure of small-scale structure, X, for dayside (squares) and nightside

(triangles). Mean values for 5° latitude bins are plotted.

Figure 50: Profiles of $\rho_{hi,7}$ from orbit P056. Each of the measurements, which are separated by 1 second, is marked by a cross.

Figure 51: Average nightside density scale heights at 110 km. All nightside density scale heights (inbound and outbound) at 110 km within a 5° latitude by 30° longitude region were identified. The mean scale height (km) is indicated by the black number. The number of scale heights from which this average was calculated is indicated by the grey number. Latitude-longitude regions for which no scale heights are available were left blank.

Figure 52: Latitude of ground track near periapsis for orbit P011.

Figure 53: Time series of density measurements from orbit P011. Both $\rho_{hi,7}$ (solid line) and $\rho_{hi,39}$ (dashed line) are shown.

Figure 54: Density profiles from orbit P011. Both $\rho_{hi,7}$ (solid line) and $\rho_{hi,39}$ (dashed line) are shown.

Figure 55: As Figure 53, but for orbit P012.

Figure 56: All outbound dayside density measurements at 130 km between 60°N and 70°N (crosses), wave-4 harmonic model fit to the data (solid line) and 1σ uncertainties about the fit (dashed lines).

Figure 57: As Figure 56, but different colours correspond to different altitudes. Black is 110 km, red is 120 km, green is 130 km and blue is 140 km. Data only available at 120–140 km.

Figure 58: As Figure 57, but for inbound nightside data. Data only available at 110–130 km.

Figure 59: Contour plot of normalized fitted densities at 120 km for outbound dayside

data. Contour intervals are 0.2 (dimensionless) and negative regions (low densities) are shaded.

Figure 60: Phases from the wave-4 harmonic fits used in Figure 59. Results are indicated by asterisks for wave-1, crosses for wave-2, triangles for wave-3 and squares for wave-4. Vertical lines are 1σ error bars. Symbols are slightly offset from the centre of their latitude band for clarity. Recall that the maximum value of the phase of the wave-n harmonic is $360°\mathrm{E}/n$.

Figure 61: Normalized amplitudes corresponding to the phases in Figure 60. Symbols as Figure 60.

Figure 62: Dayside (LST = 16.44–16.68 hours) density measurements at 130 km between 70°N and 80°N. Symbols as Figure 56.

Figure 63: Nightside (LST = 2.25–2.67 hours) density measurements at 130 km between 70°N and 80°N. Symbols as Figure 56.

Figure 64: Outbound densities at 130 km from orbits 130–160 of MGS Phase 1. Symbols as Figure 56.

Figure 65: Relative amplitudes of harmonic components from fits to outbound densities from MGS Phase 1. Fits were performed to densities from orbits 70–100, 80–110, 90–120, ..., 170–200. Results are plotted near the centre of their corresponding orbit interval, different components are offset by slightly different amounts to minimize overlap. Symbols are asterisks for wave-1, crosses for wave-2, triangles for wave-3 and squares for wave-4. Vertical lines are 1σ error bars.

Figure 66: Phases corresponding to the relative amplitudes in Figure 65. Symbols as Figure 65.

Figure 67: Dayside MTGCM (crosses) and ODY (small filled circles) densities. MTGCM densities at X° latitude and 100 (110, 120, 130, 140) km are plotted at X°-2° (X°-1°, X°, X°+1°, X°+2°). This minimizes the overlap of MTGCM data points. Colours indicate altitude. For MTGCM densities, dark blue crosses correspond to 100 km and 130 km, with large densities at 100 km clearly distinguishable from small densities at 130 km. Similarly, black crosses correspond to 110 km and 140 km. Pink crosses correspond to 120 km. For ODY densities, small filled green circles correspond to 100 km and 130 km. Small filled red circles correspond to 110 km and 140 km. Small filled light blue circles correspond to 120 km.

Figure 68: As Figure 67, but nightside densities. Data and simulations are shown at 110, 120 and 130 km.

Figure 69: Dayside MTGCM (crosses) and ODY (small and large filled circles) scale heights. Data and simulations are shown at 110, 120 and 130 km. MTGCM data points are offset in latitude and colours indicate altitude as in Figure 68. Small filled circles, which exhibit significant scatter, are individual ODY data points as in Figure 68. Large filled circles indicate the mean value of all ODY data points from a given altitude within a ten degree latitude band. Altitude is indicated by the colours of large filled circles as it is for small filled circles.

Figure 70: As Figure 69, but nightside scale heights.

Figure 71: Mean dayside (grey) and nightside (black) densities. Symbols indicate altitude at 100 km (square), 110 km (X), 120 km (triangle), 130 km (+) and 140 km (diamond). All inbound and outbound data points within a five degree latitude interval were averaged. Data points from different altitudes are offset slightly in latitude to minimize overlap.

Figure 72: As Figure 71, but scale height.

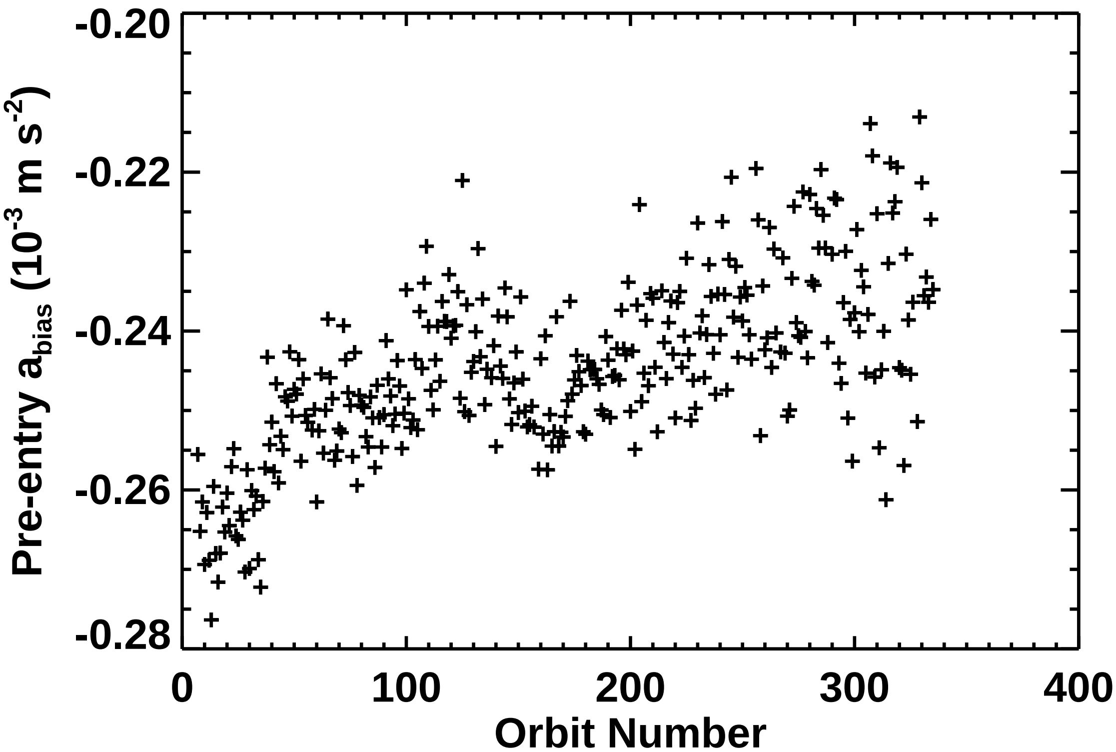

Fig. 1.— Author Paul Withers — Odyssey Accelerometer Data

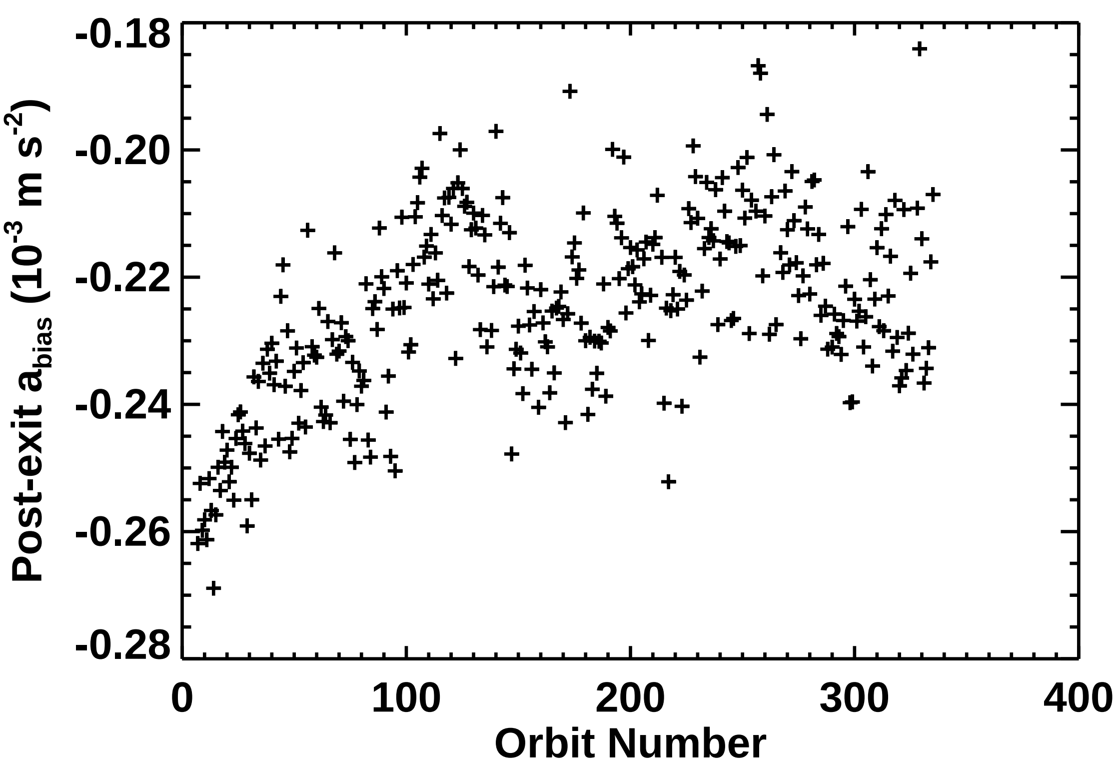

Fig. 2.— Author Paul Withers — Odyssey Accelerometer Data

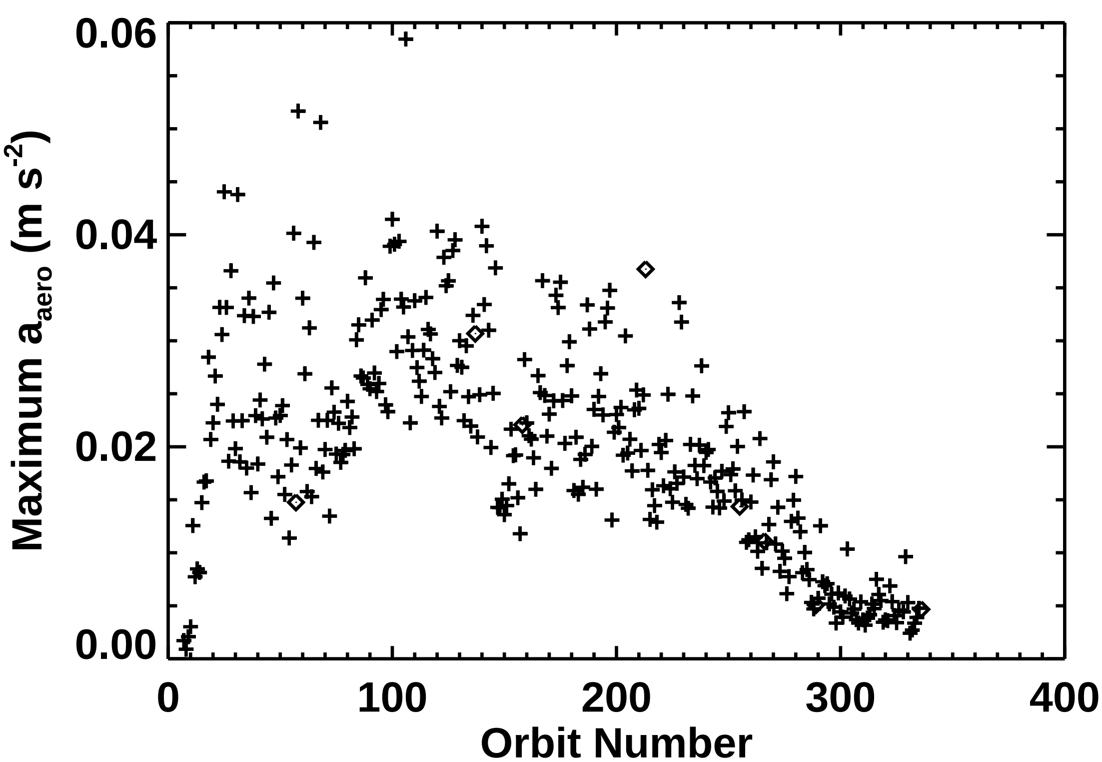

Fig. 3.— Author Paul Withers — Odyssey Accelerometer Data

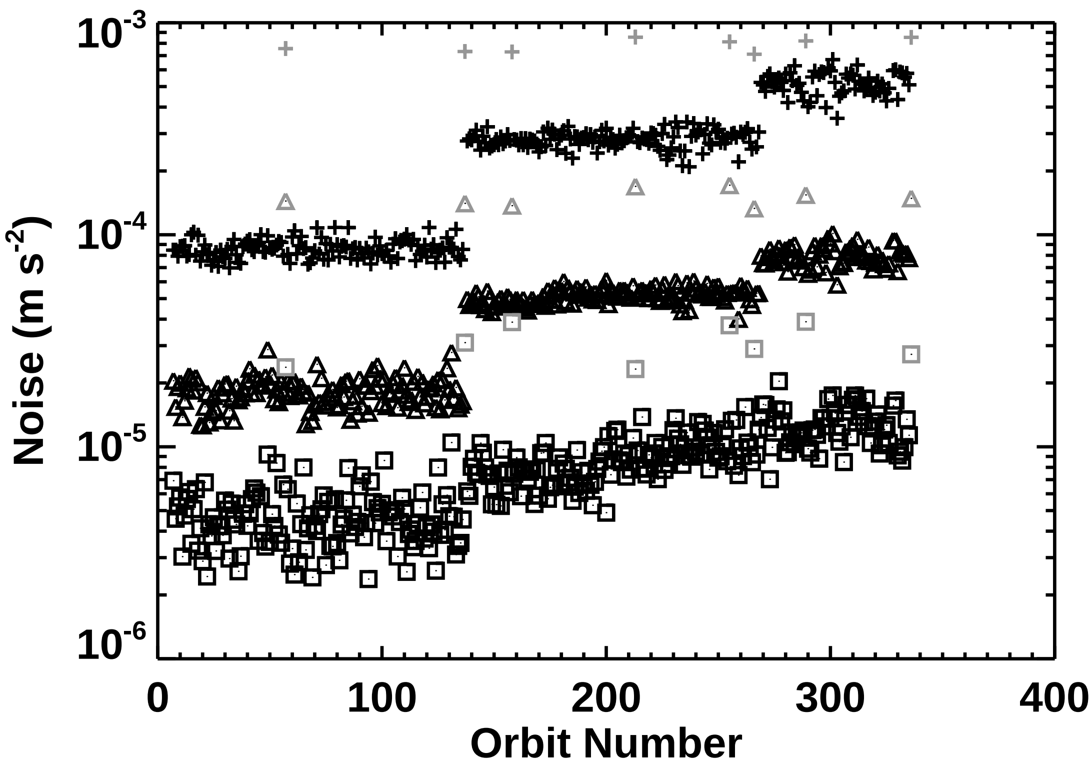

Fig. 4.— Author Paul Withers — Odyssey Accelerometer Data

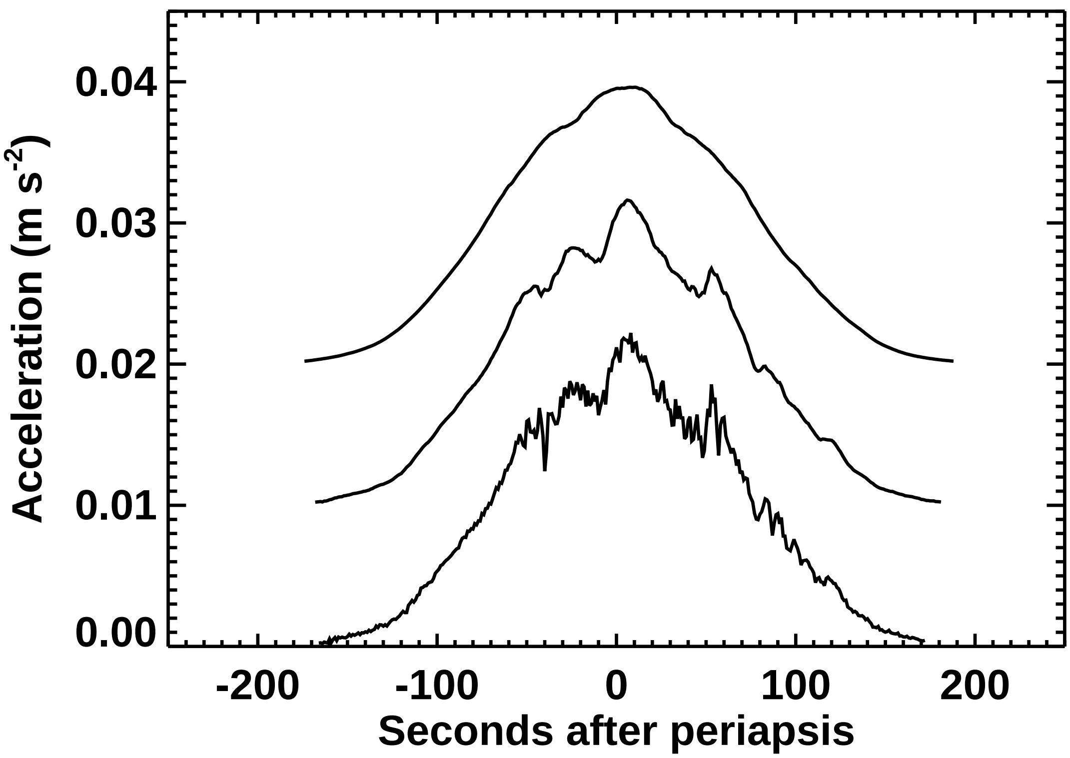

Fig. 5.— Author Paul Withers — Odyssey Accelerometer Data

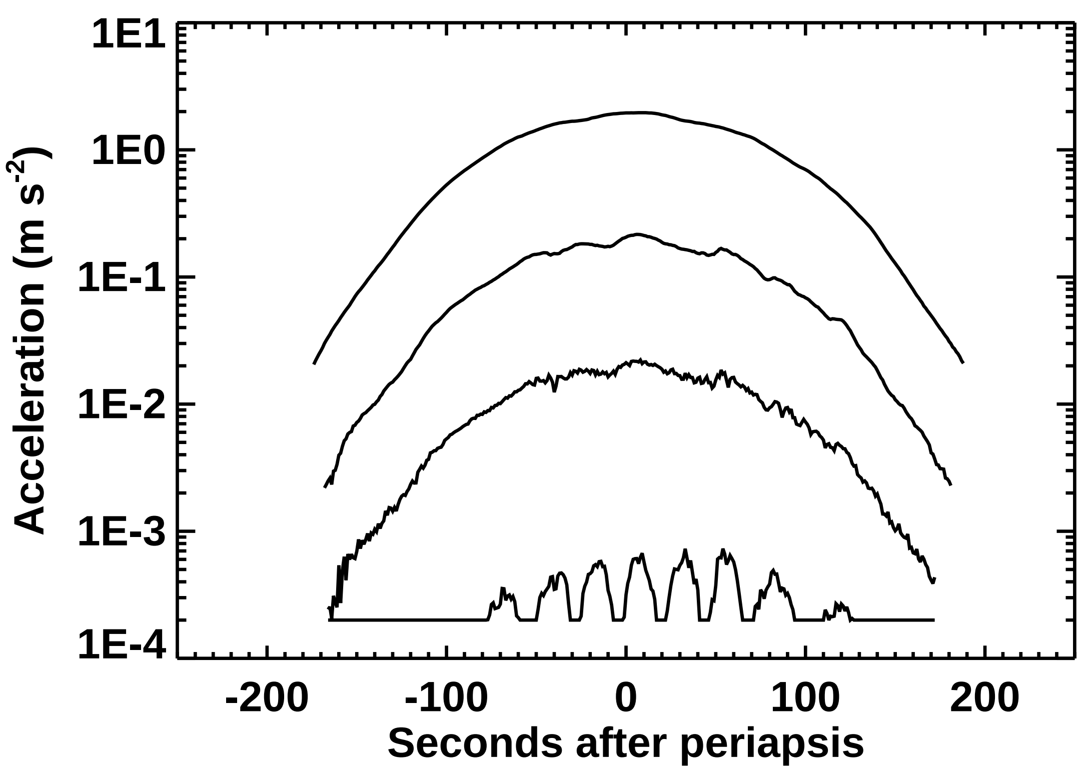

Fig. 6.— Author Paul Withers — Odyssey Accelerometer Data

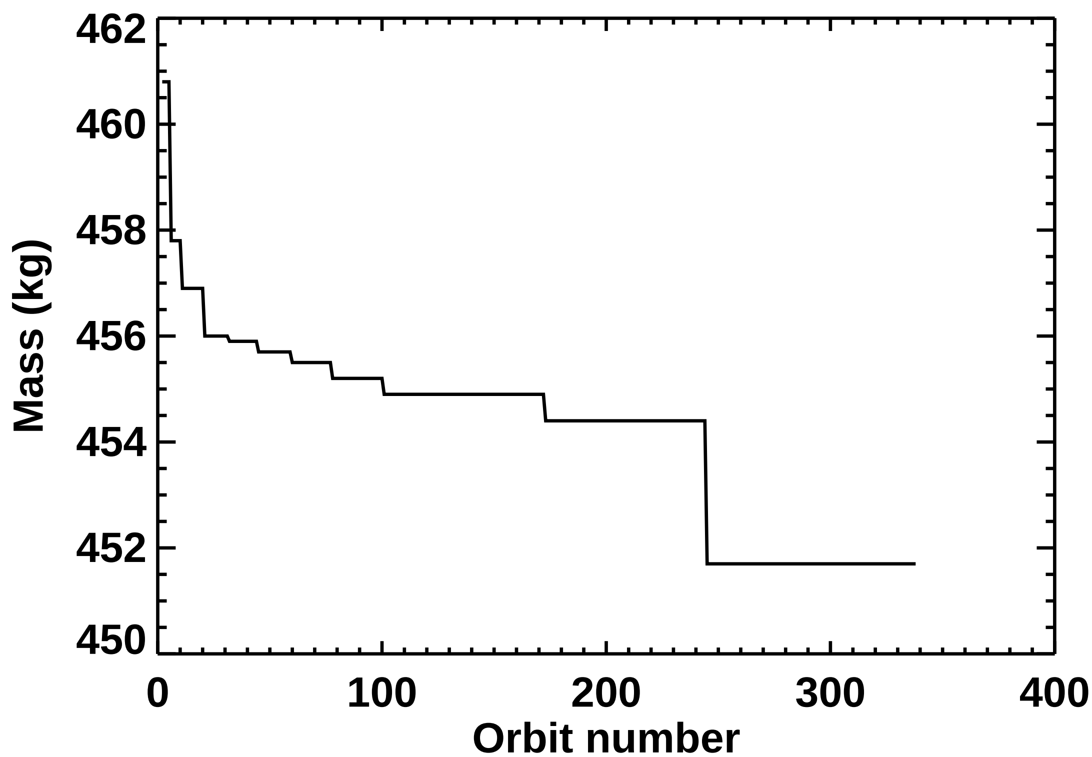

Fig. 7.— Author Paul Withers — Odyssey Accelerometer Data

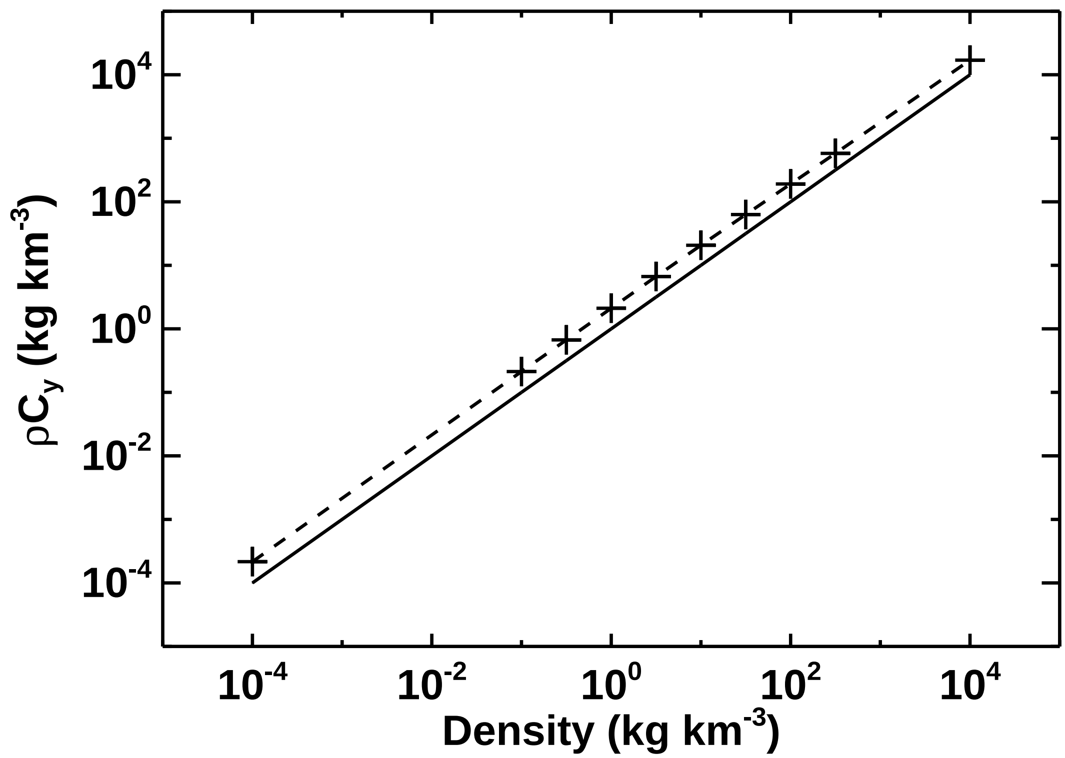

Fig. 8.— Author Paul Withers — Odyssey Accelerometer Data

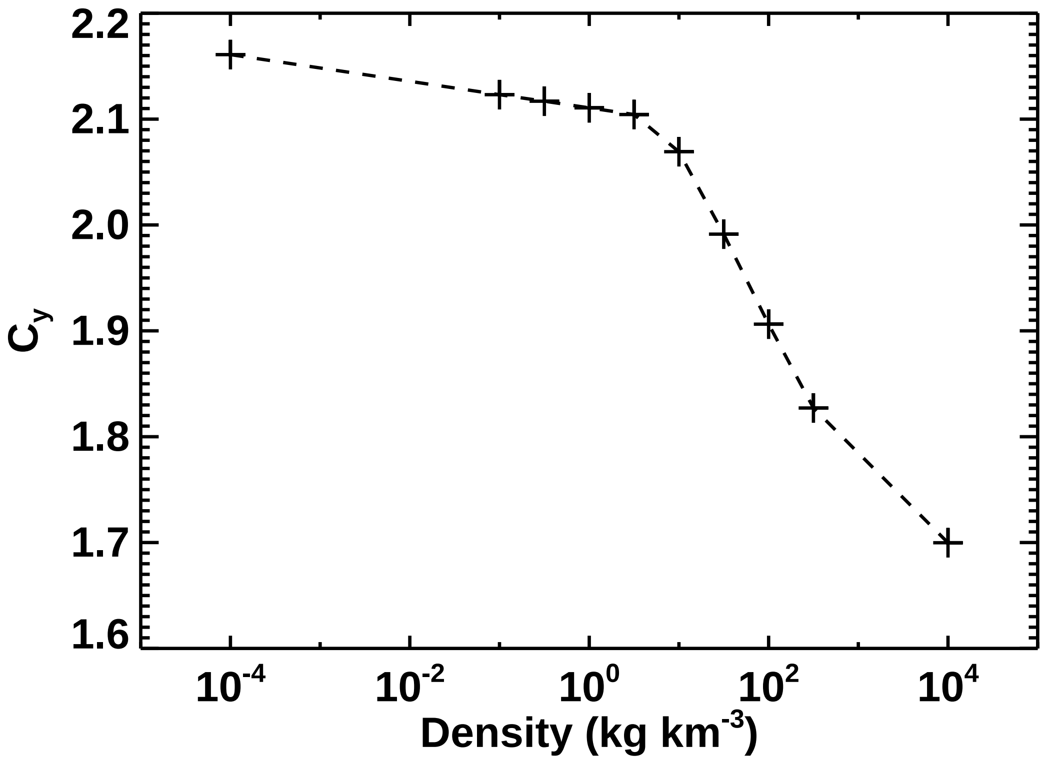

Fig. 9.— Author Paul Withers — Odyssey Accelerometer Data

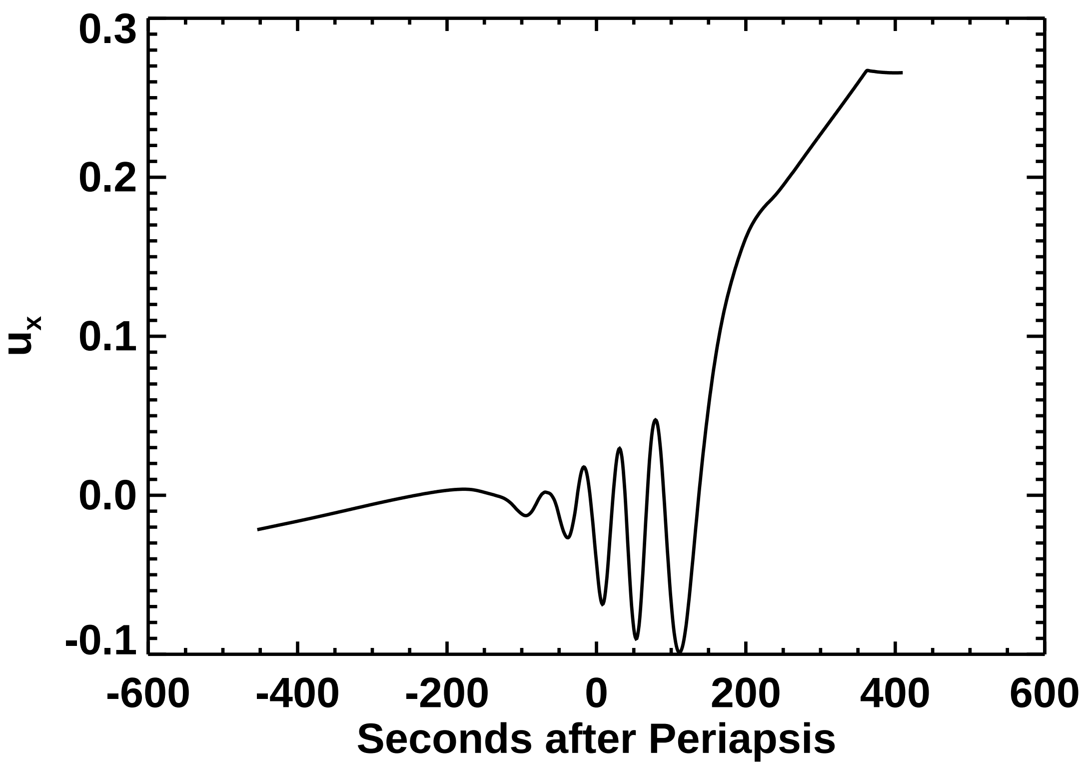

Fig. 10.— Author Paul Withers — Odyssey Accelerometer Data

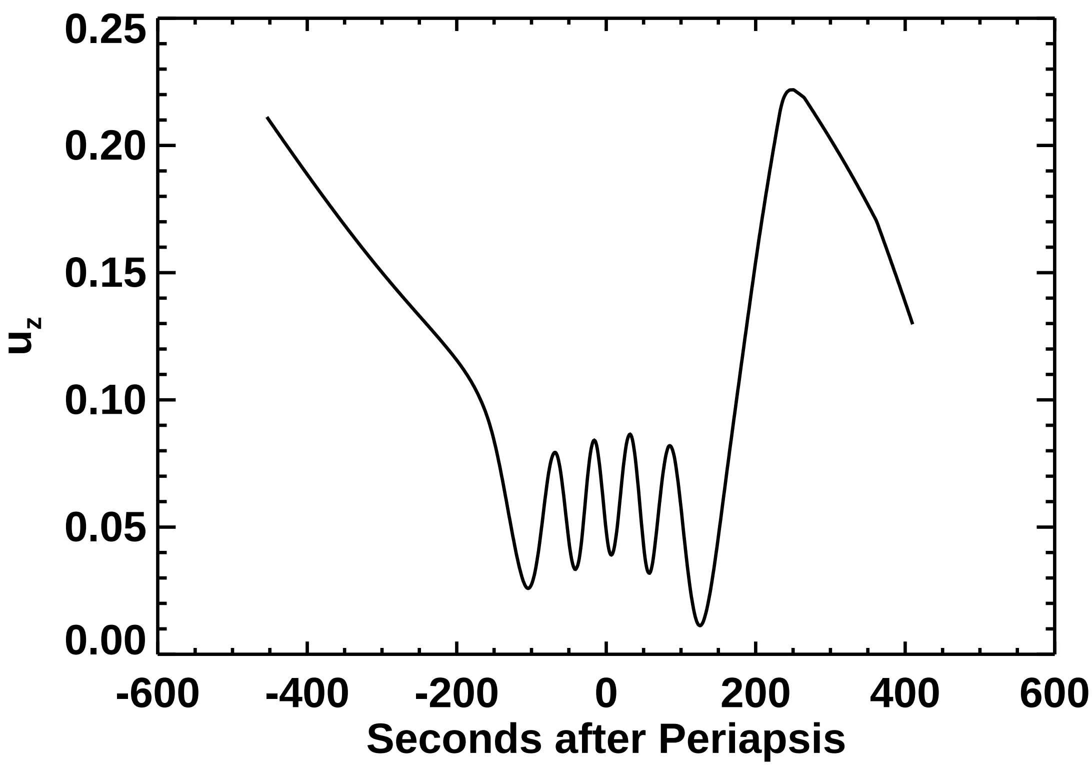

Fig. 11.— Author Paul Withers — Odyssey Accelerometer Data

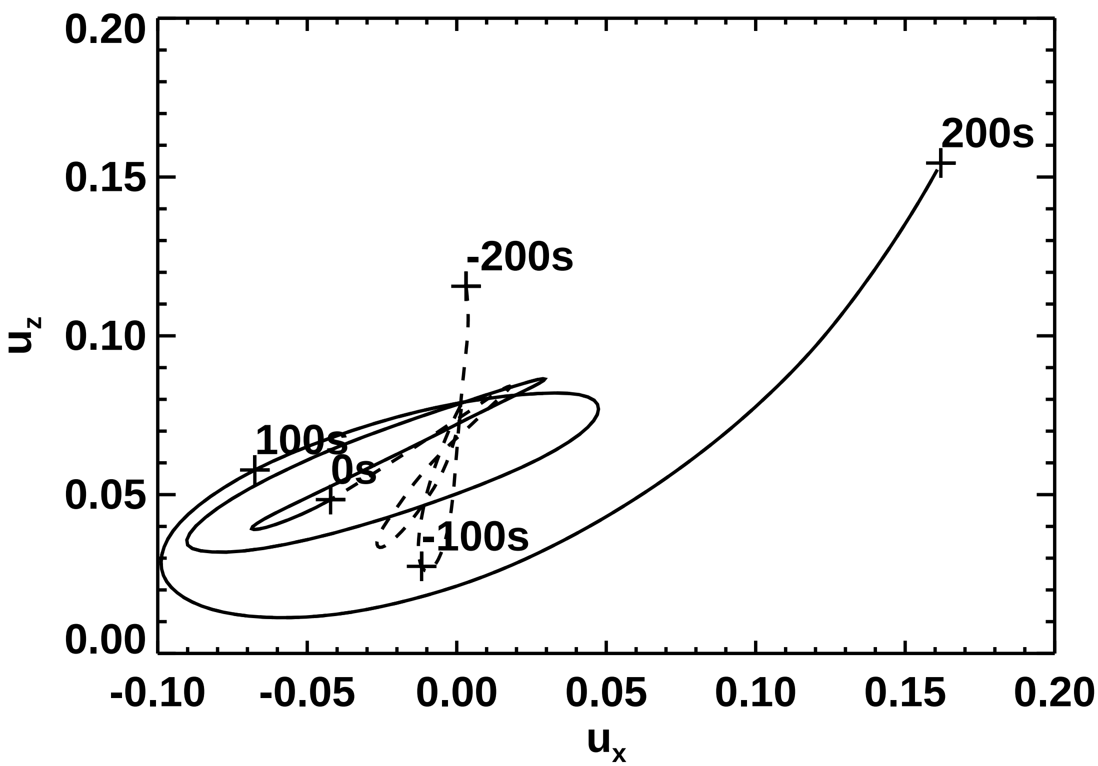

Fig. 12.— Author Paul Withers — Odyssey Accelerometer Data

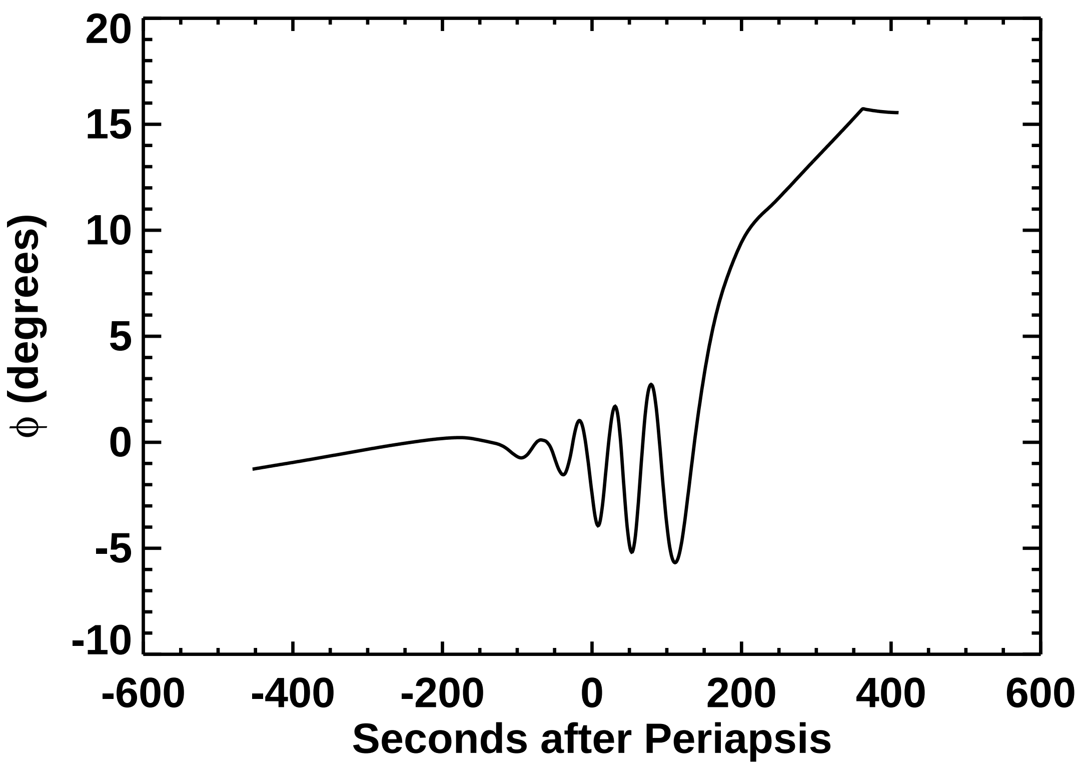

Fig. 13.— Author Paul Withers — Odyssey Accelerometer Data

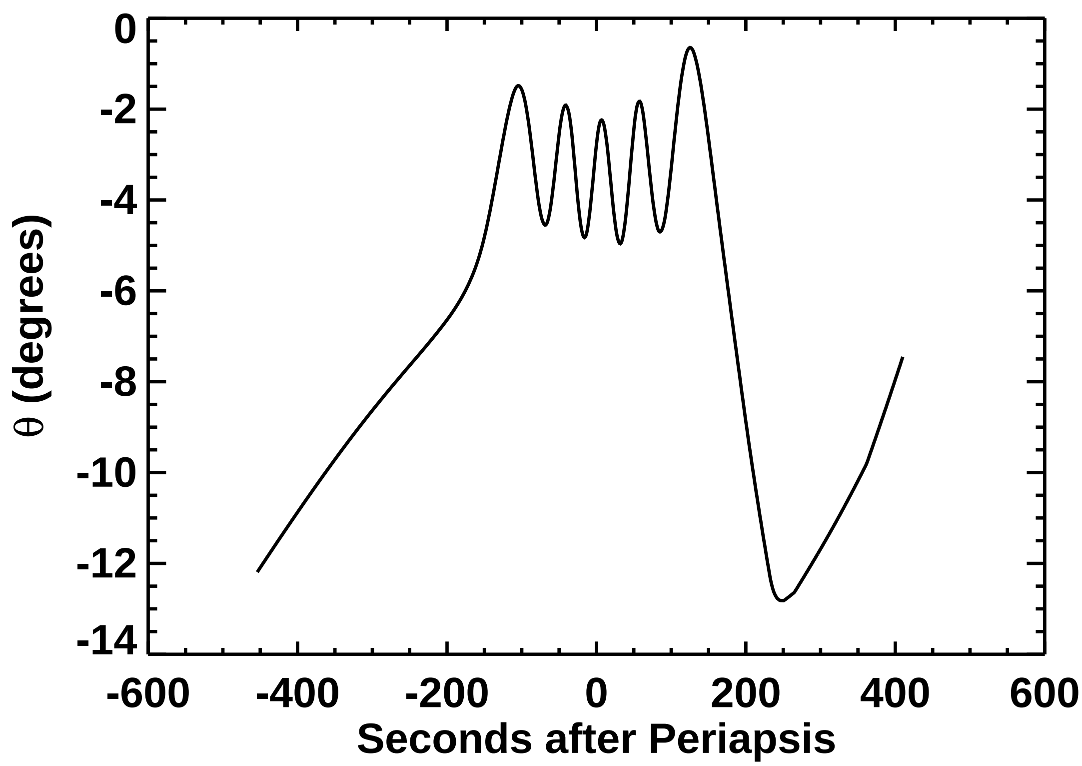

Fig. 14.— Author Paul Withers — Odyssey Accelerometer Data

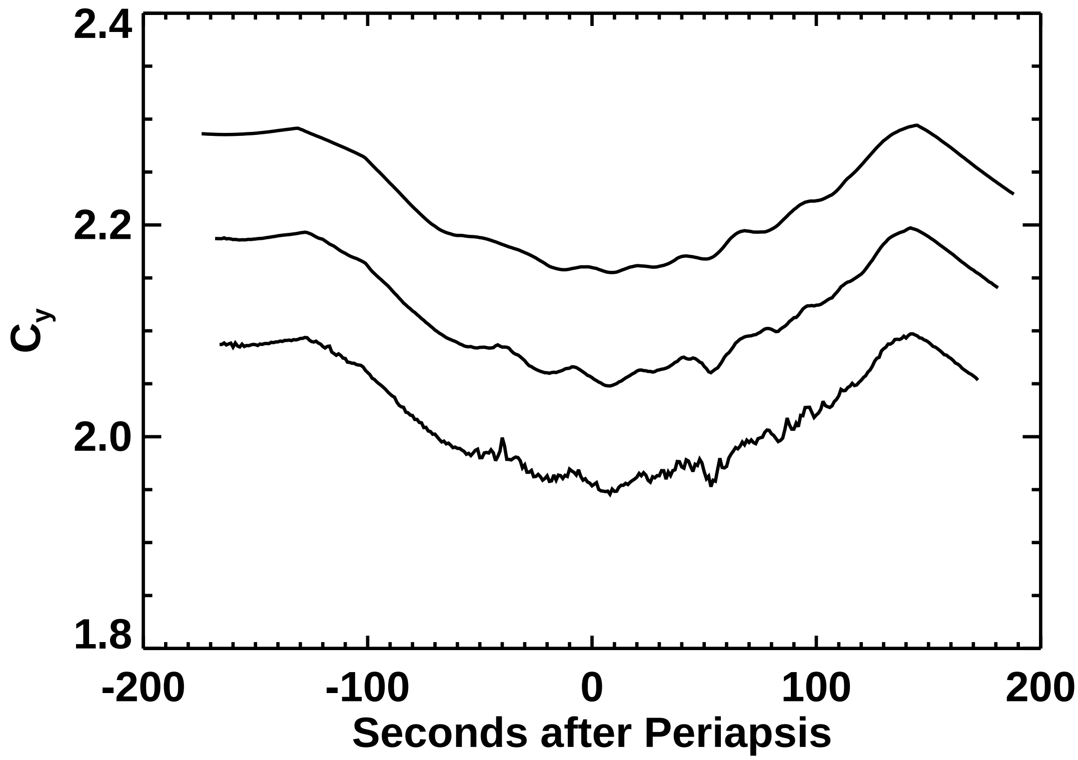

Fig. 15.— Author Paul Withers — Odyssey Accelerometer Data

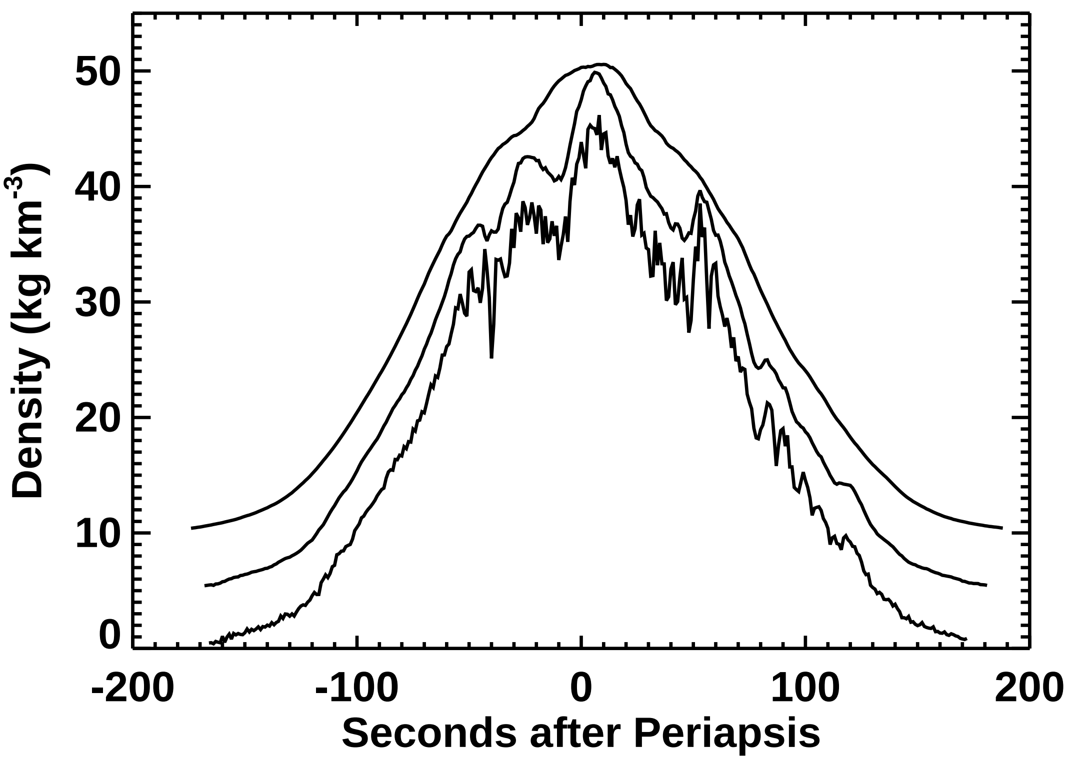

Fig. 16.— Author Paul Withers — Odyssey Accelerometer Data

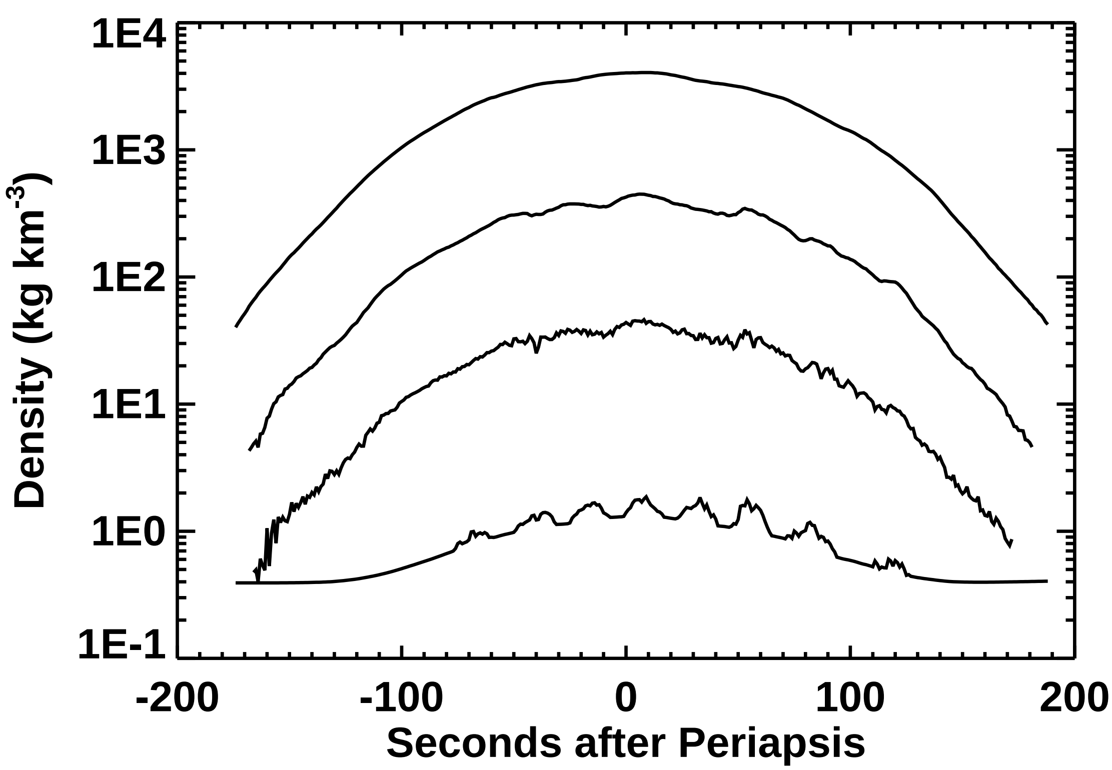

Fig. 17.— Author Paul Withers — Odyssey Accelerometer Data

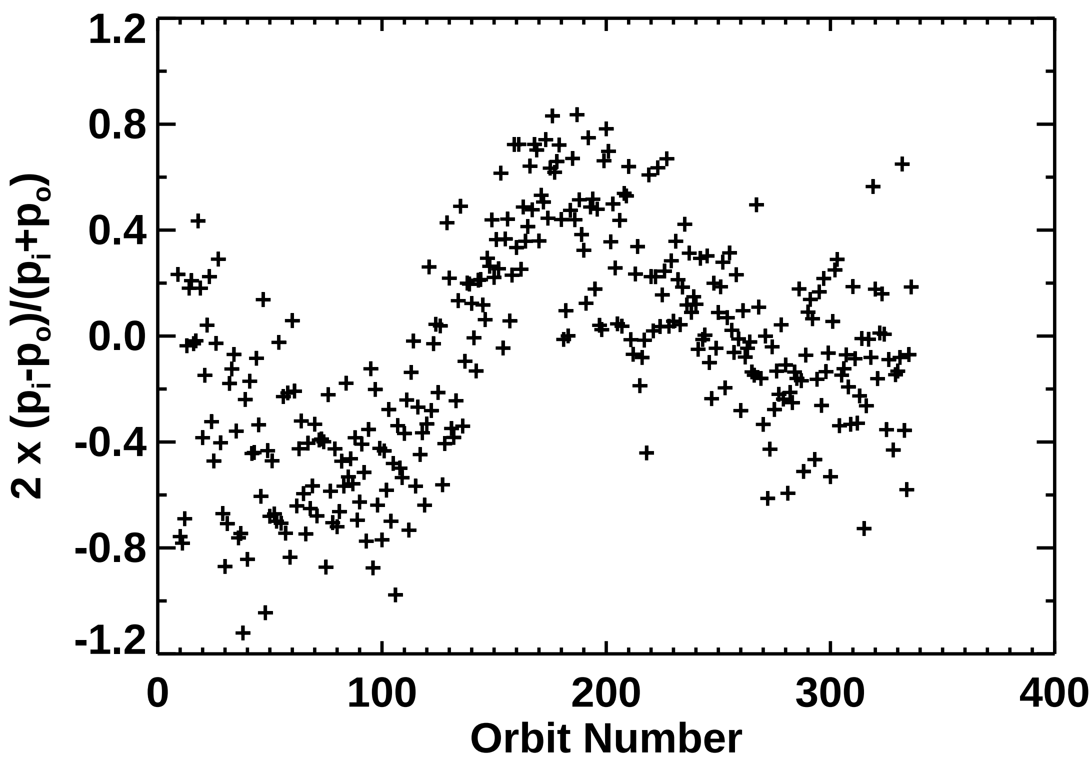

Fig. 18.— Author Paul Withers — Odyssey Accelerometer Data

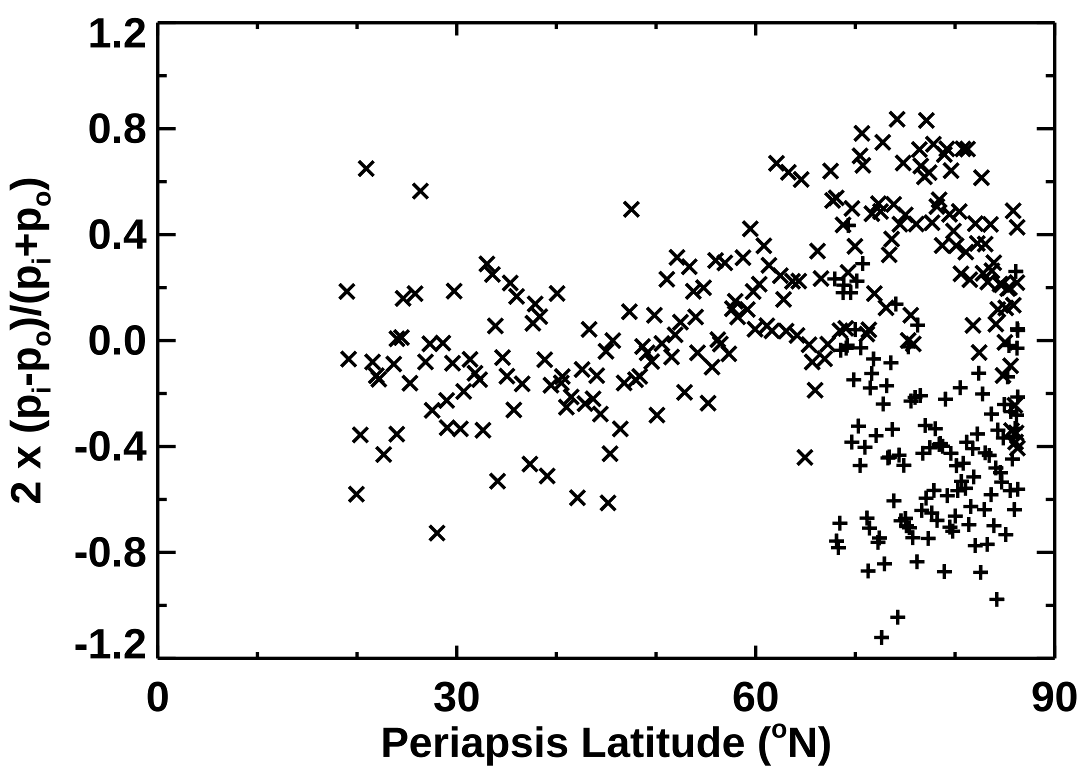

Fig. 19.— Author Paul Withers — Odyssey Accelerometer Data

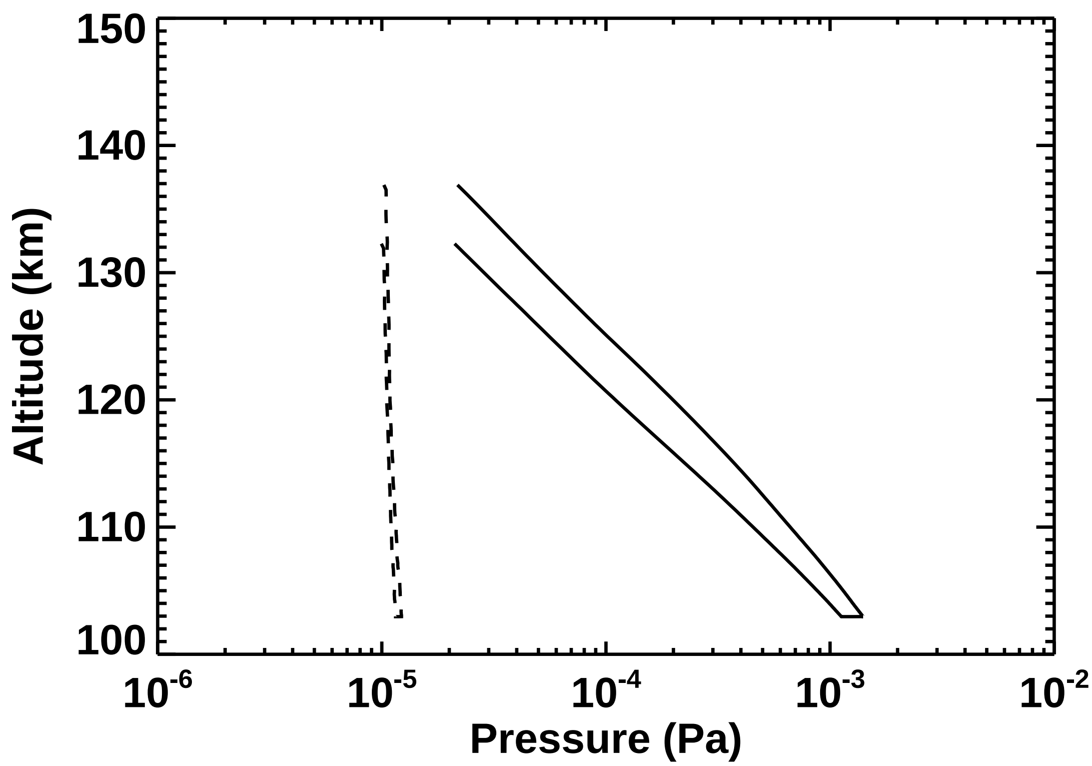

Fig. 20.— Author Paul Withers — Odyssey Accelerometer Data

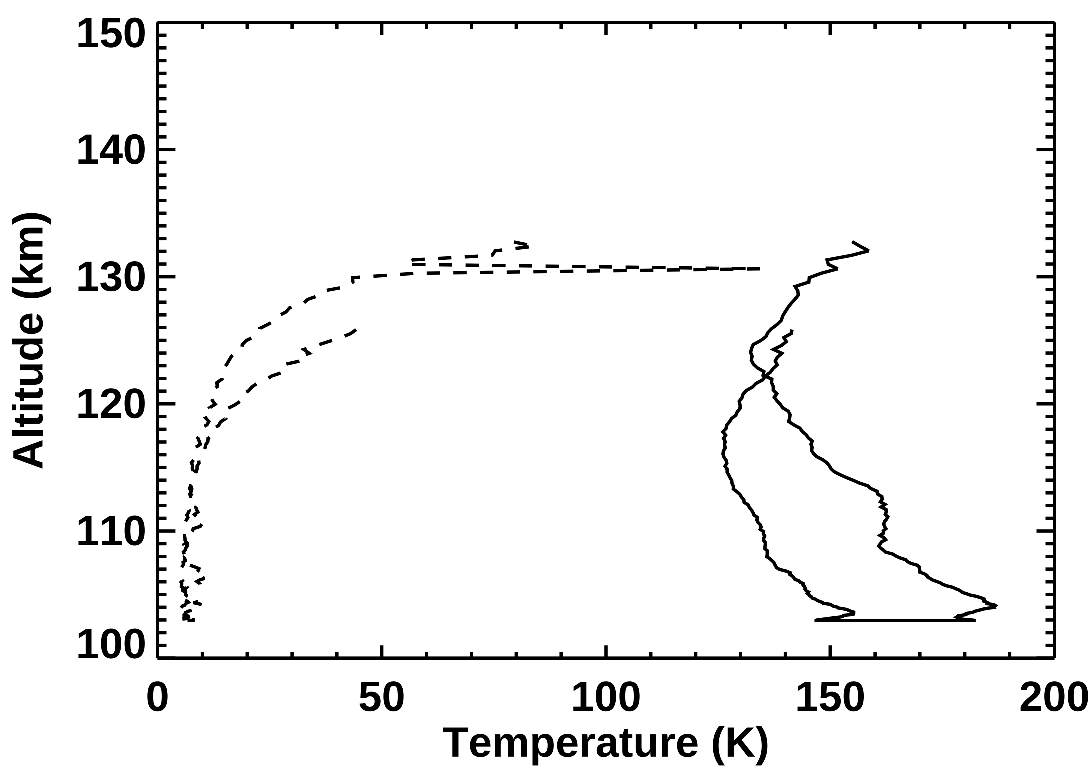

Fig. 21.— Author Paul Withers — Odyssey Accelerometer Data

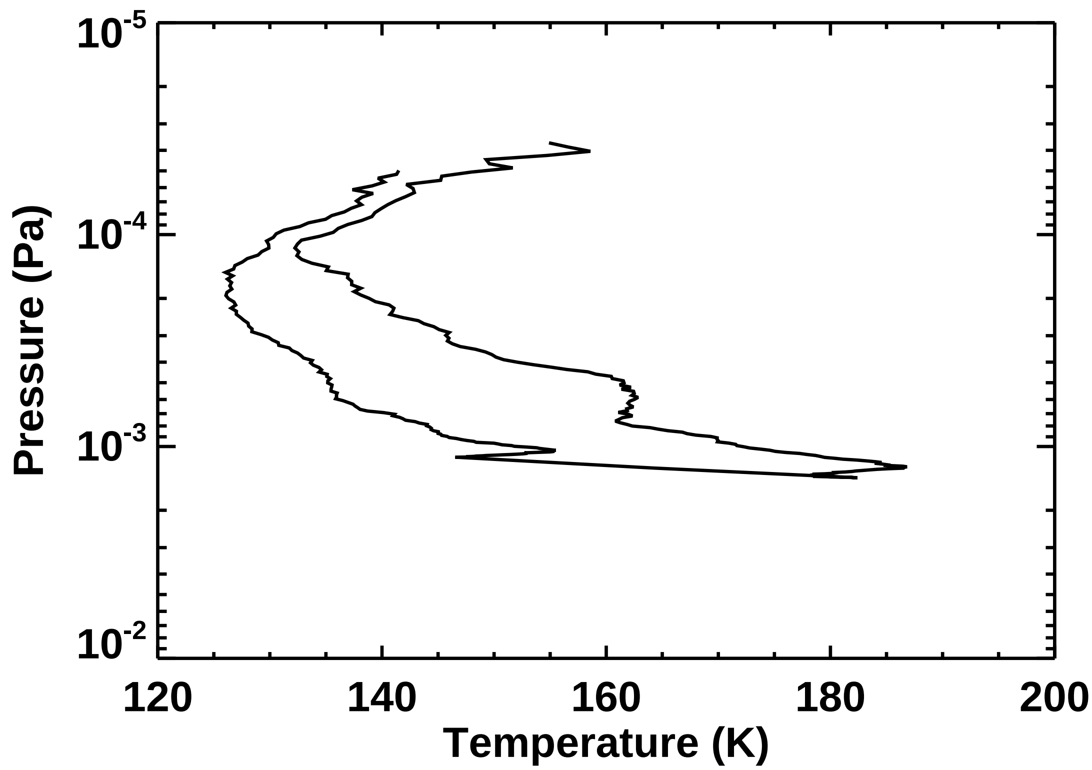

Fig. 22.— Author Paul Withers — Odyssey Accelerometer Data

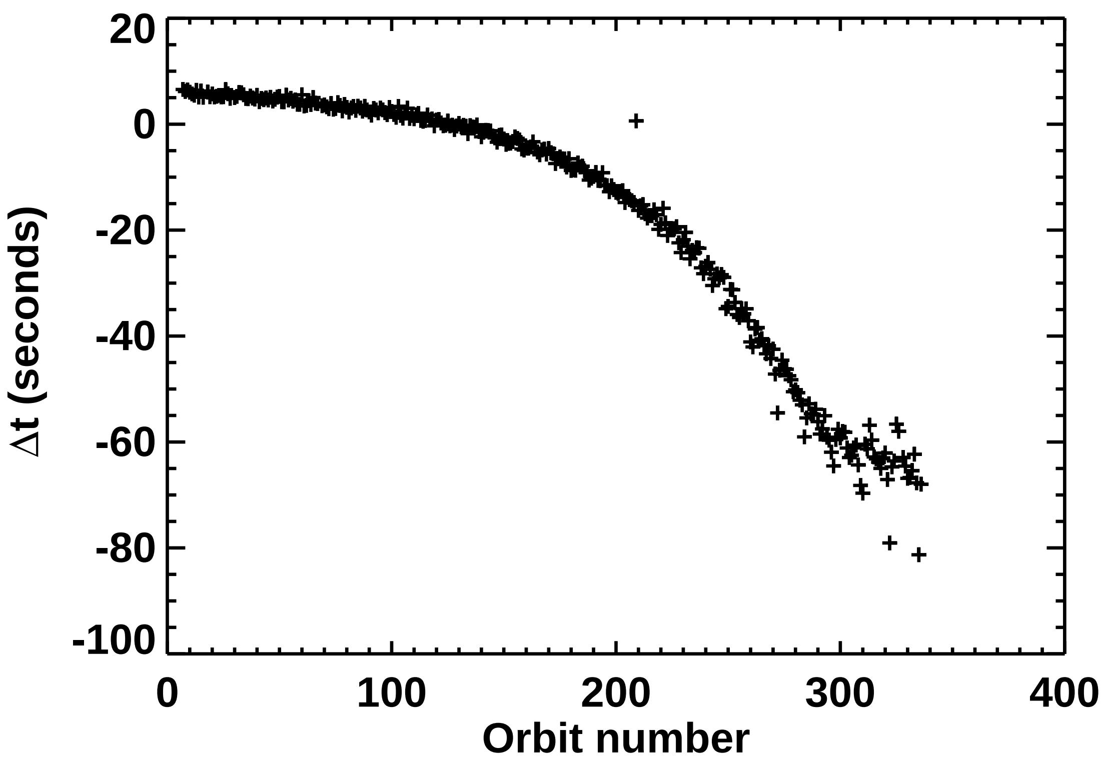

Fig. 23.— Author Paul Withers — Odyssey Accelerometer Data

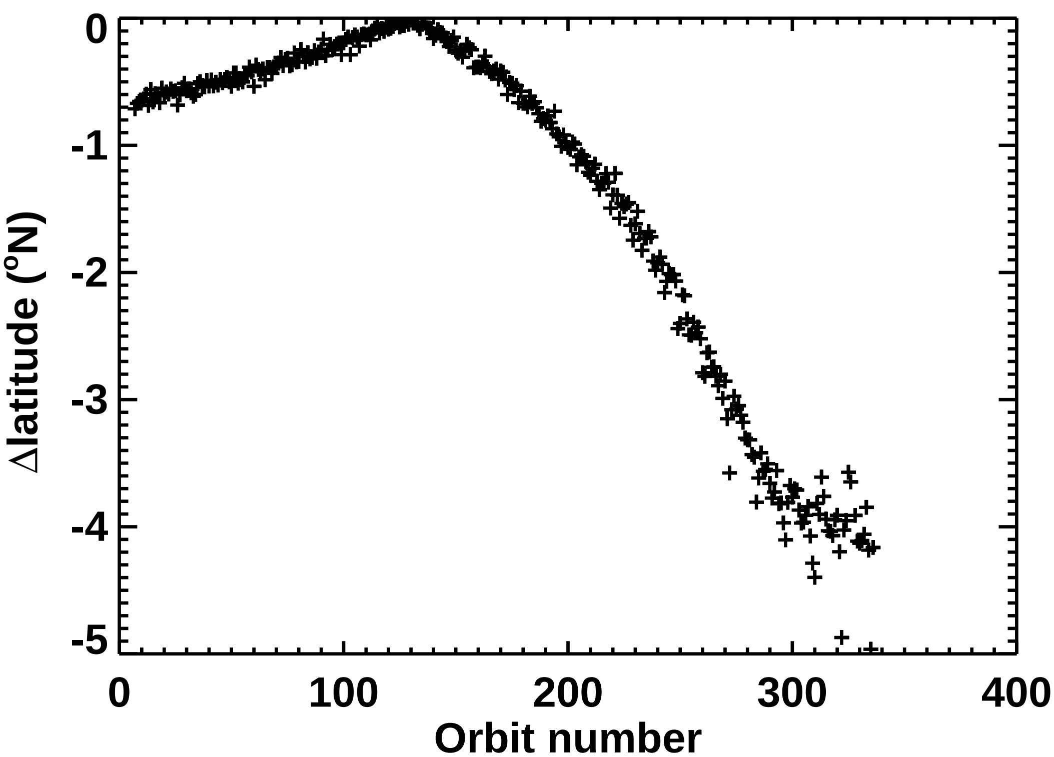

Fig. 24.— Author Paul Withers — Odyssey Accelerometer Data

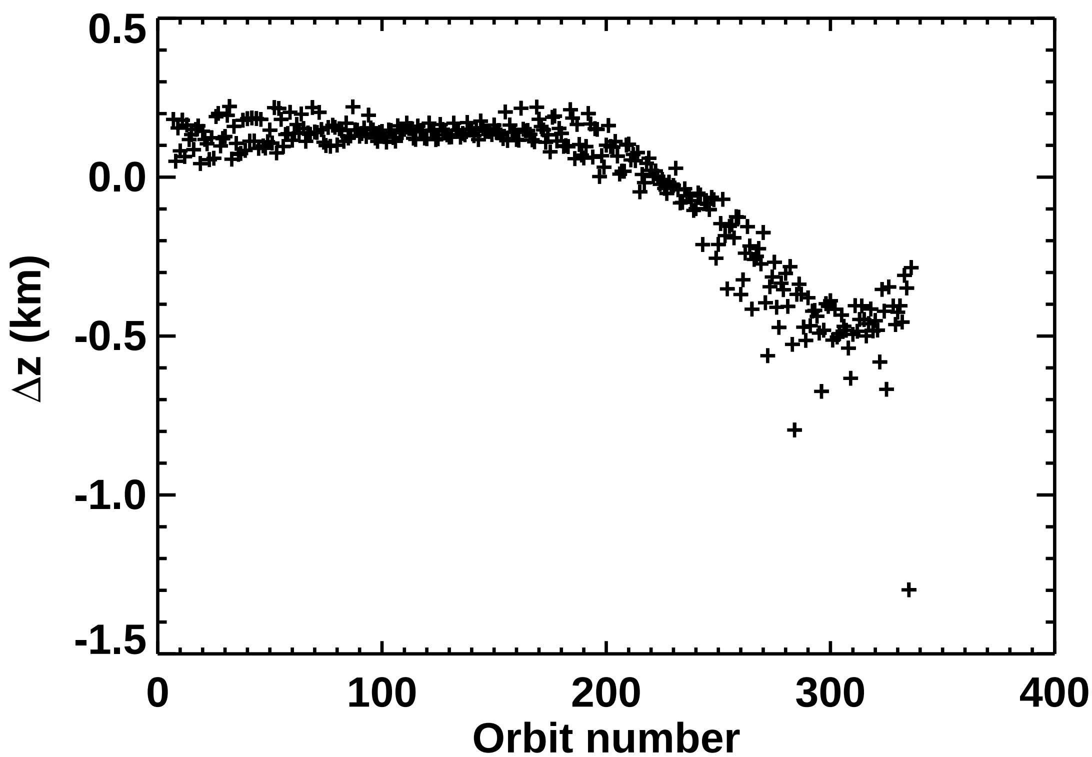

Fig. 25.— Author Paul Withers — Odyssey Accelerometer Data

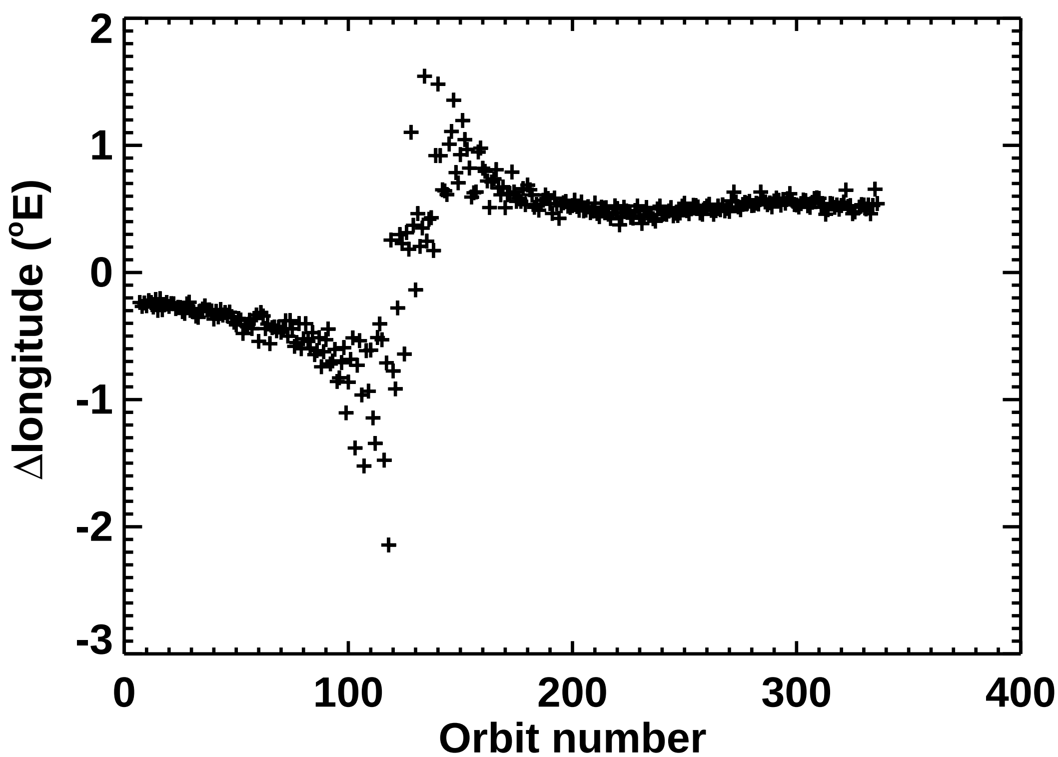

Fig. 26.— Author Paul Withers — Odyssey Accelerometer Data

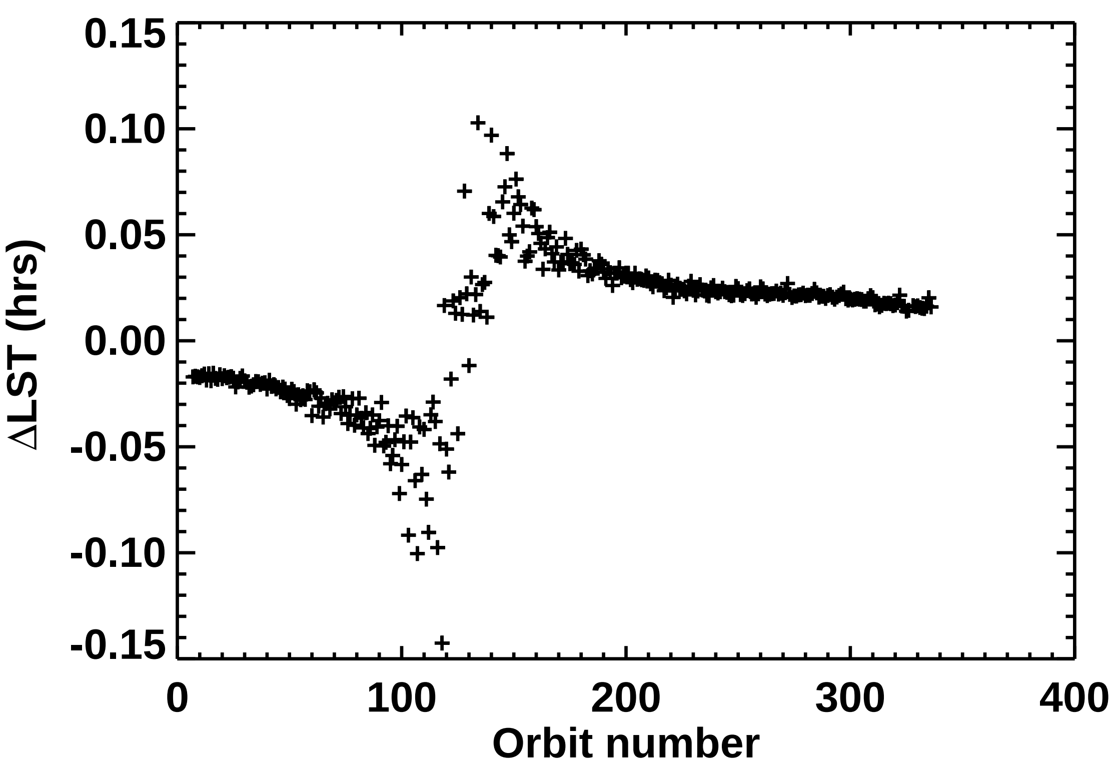

Fig. 27.— Author Paul Withers — Odyssey Accelerometer Data

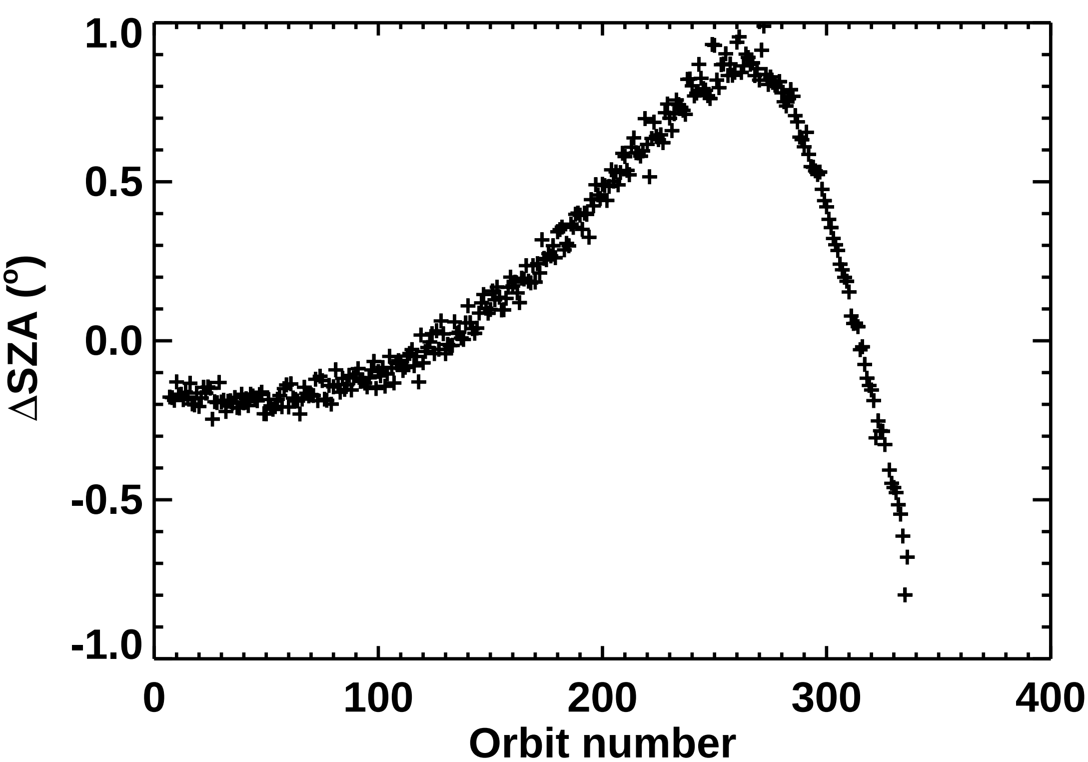

Fig. 28.— Author Paul Withers — Odyssey Accelerometer Data

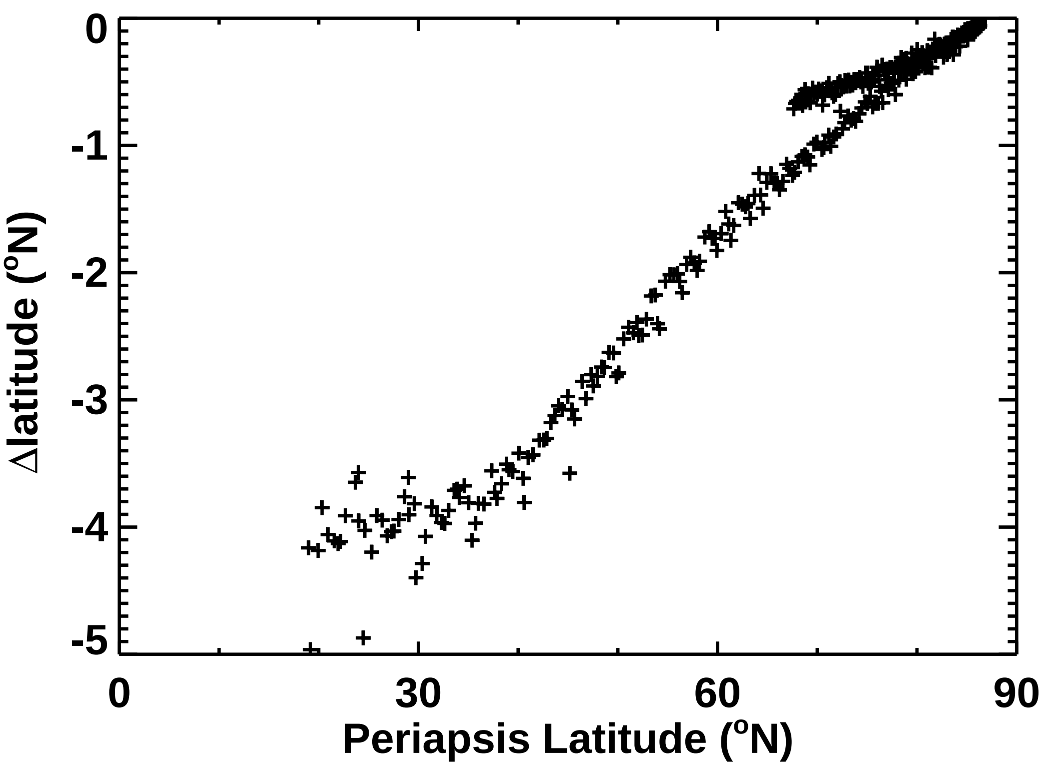

Fig. 29.— Author Paul Withers — Odyssey Accelerometer Data

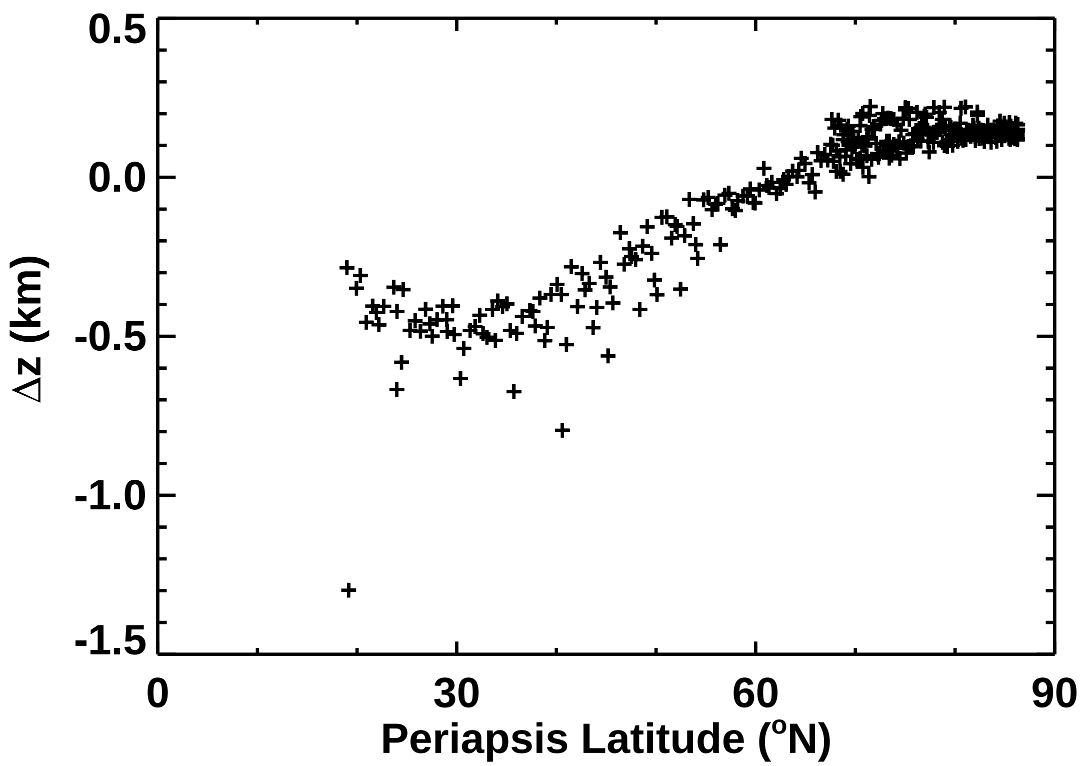

Fig. 30.— Author Paul Withers — Odyssey Accelerometer Data

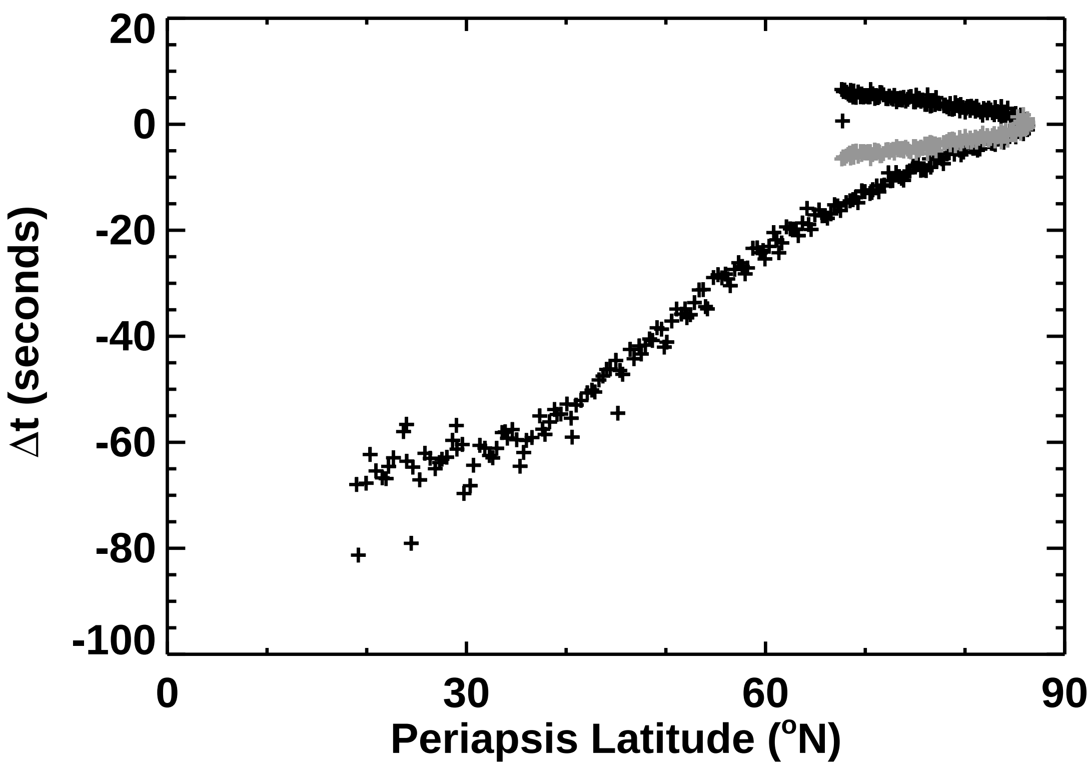

Fig. 31.— Author Paul Withers — Odyssey Accelerometer Data

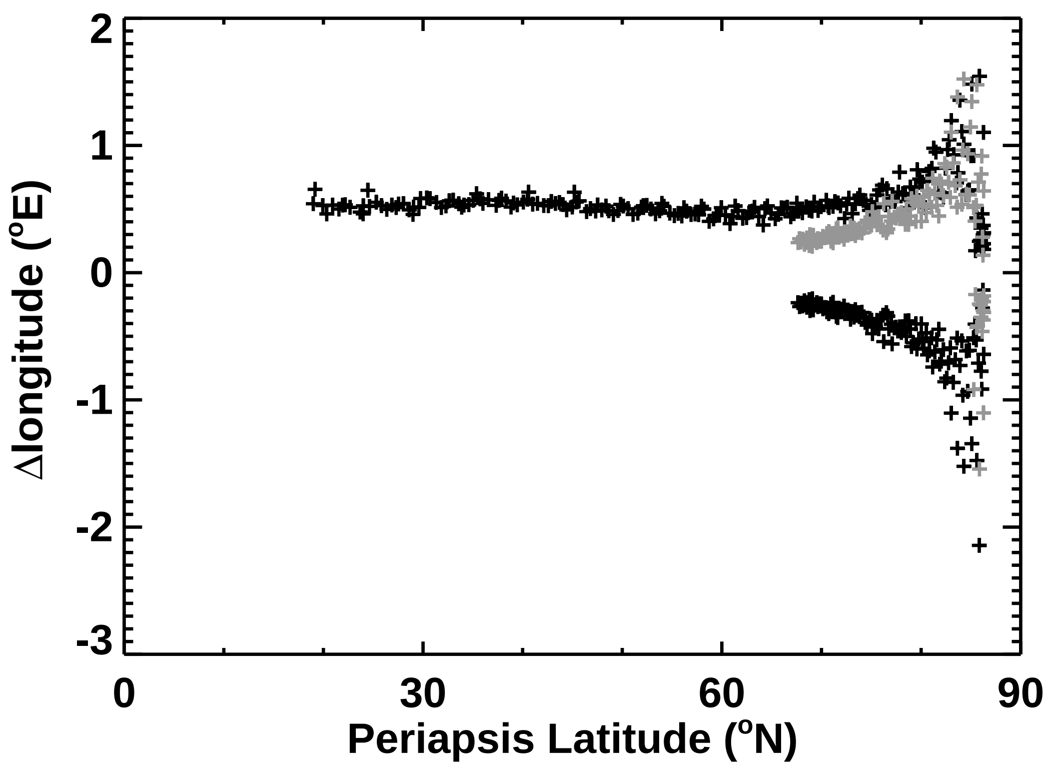

Fig. 32.— Author Paul Withers — Odyssey Accelerometer Data

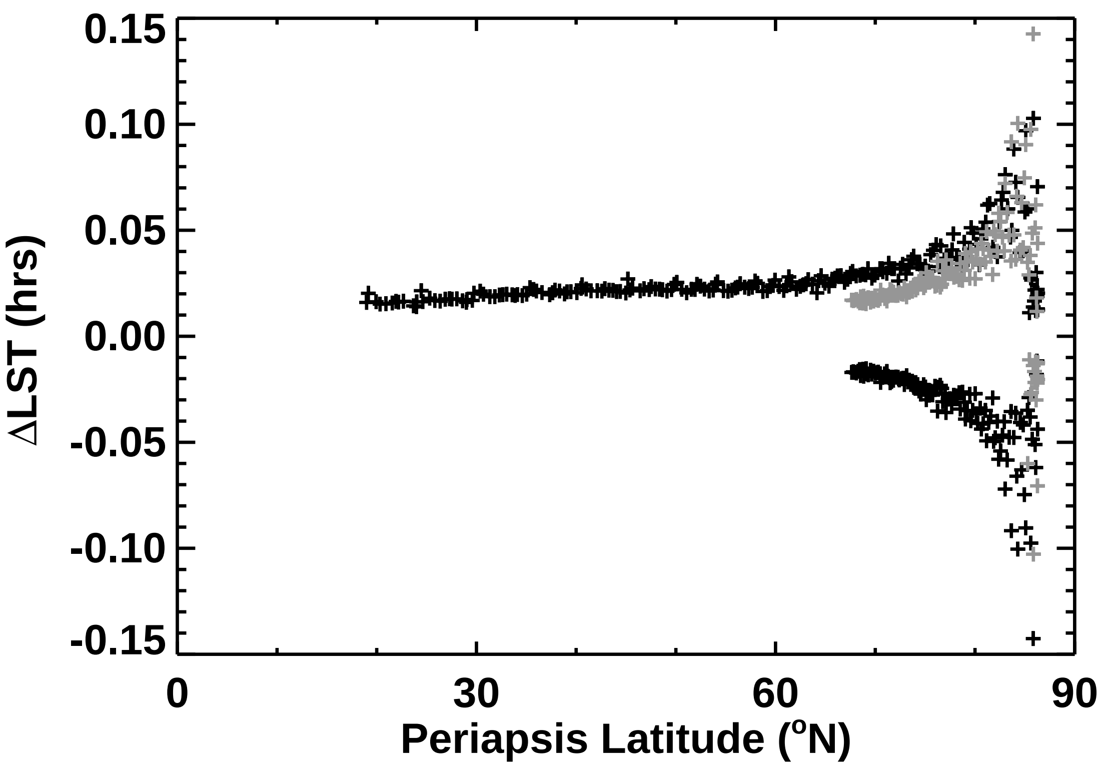

Fig. 33.— Author Paul Withers — Odyssey Accelerometer Data

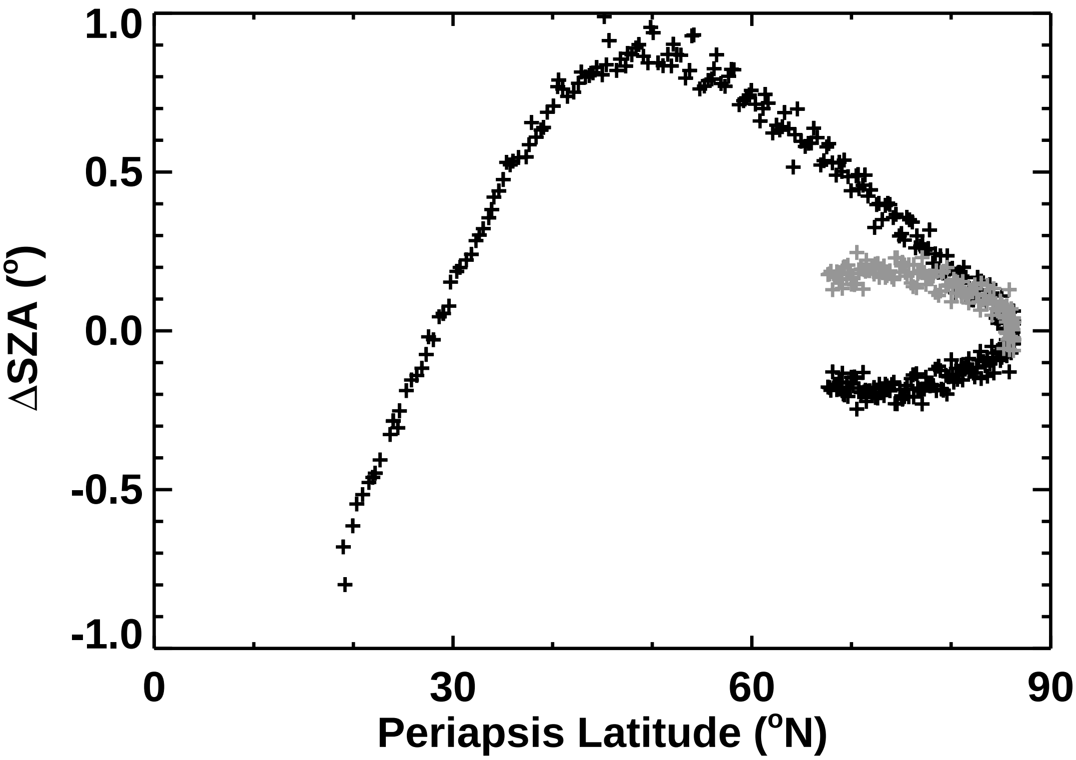

Fig. 34.— Author Paul Withers — Odyssey Accelerometer Data

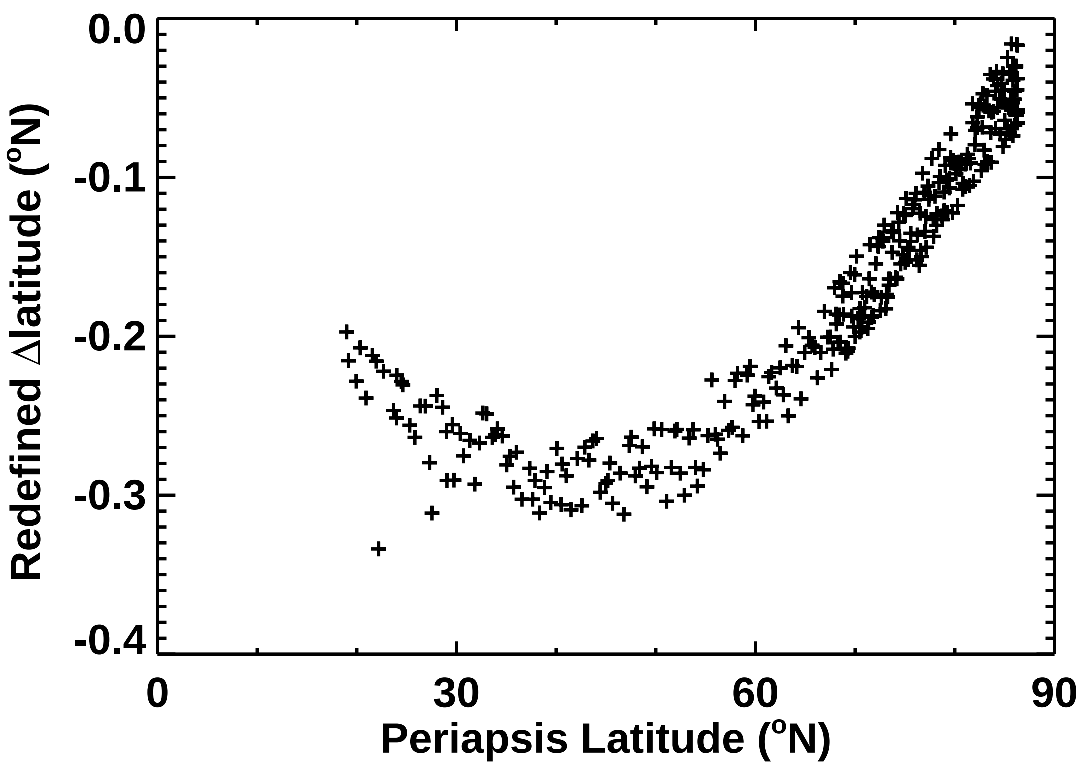

Fig. 35.— Author Paul Withers — Odyssey Accelerometer Data

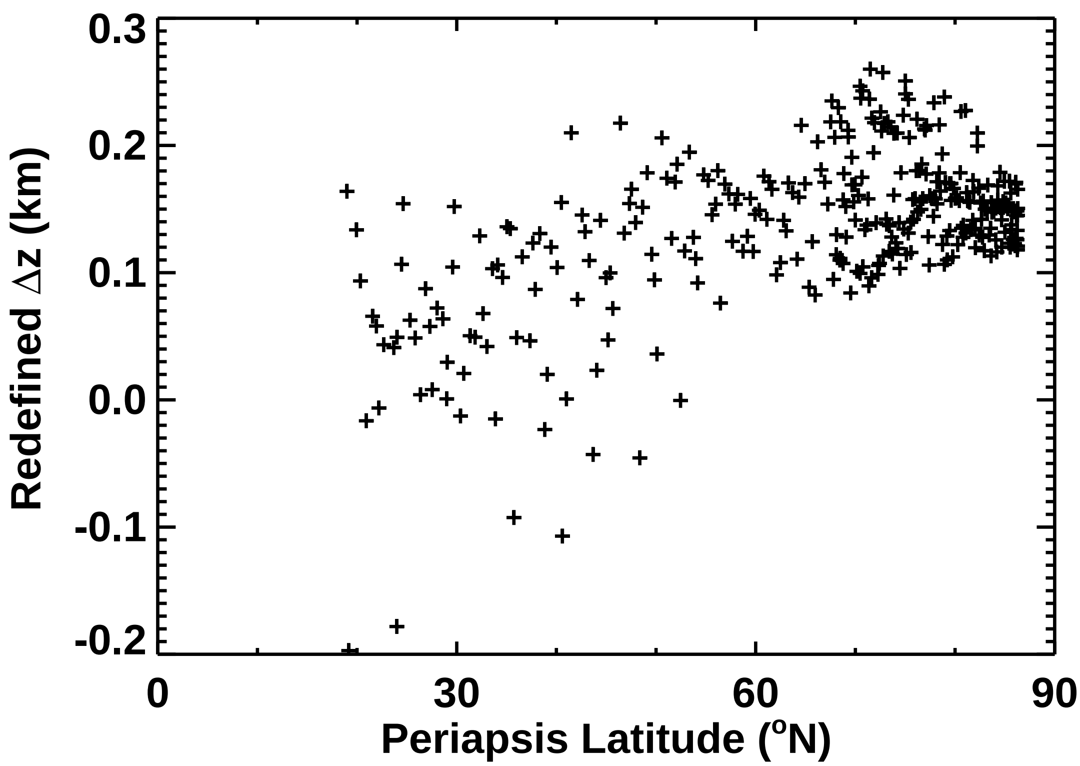

Fig. 36.— Author Paul Withers — Odyssey Accelerometer Data

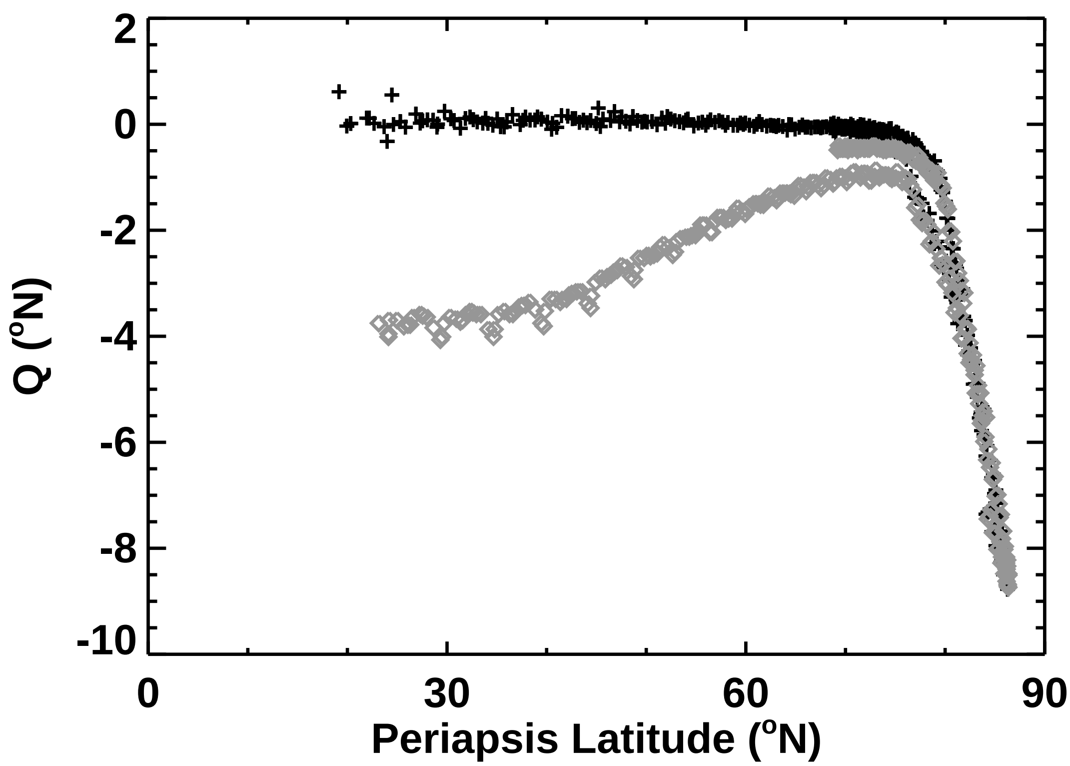

Fig. 37.— Author Paul Withers — Odyssey Accelerometer Data

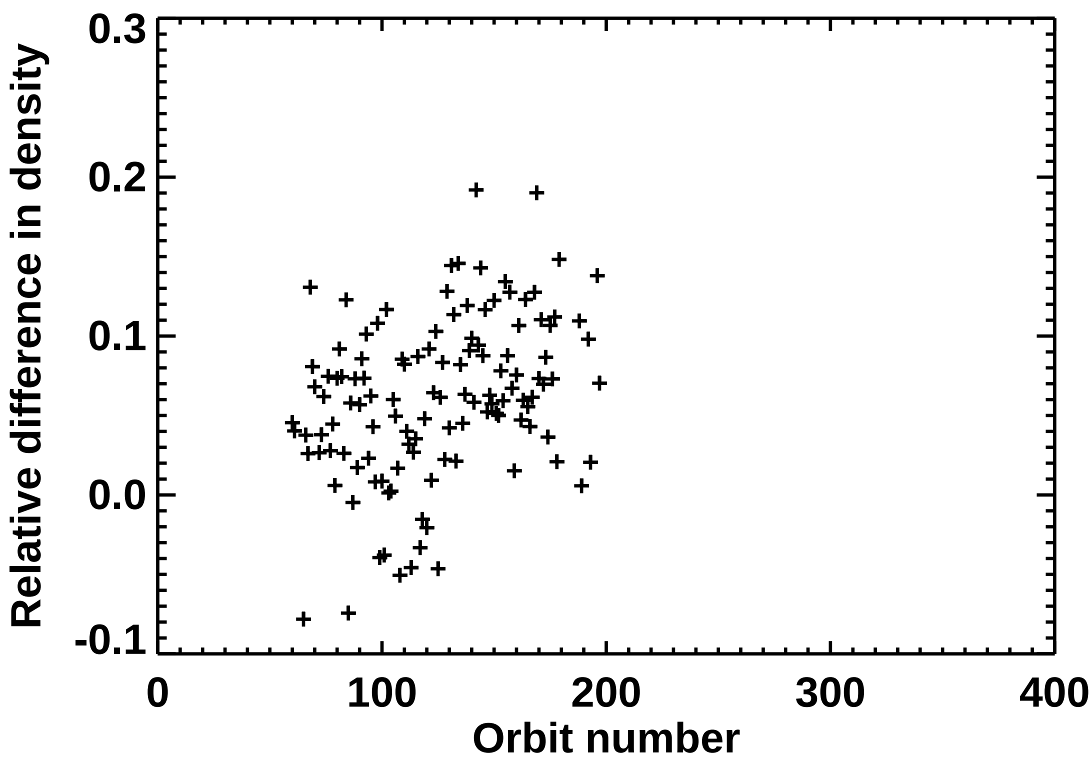

Fig. 38.— Author Paul Withers — Odyssey Accelerometer Data

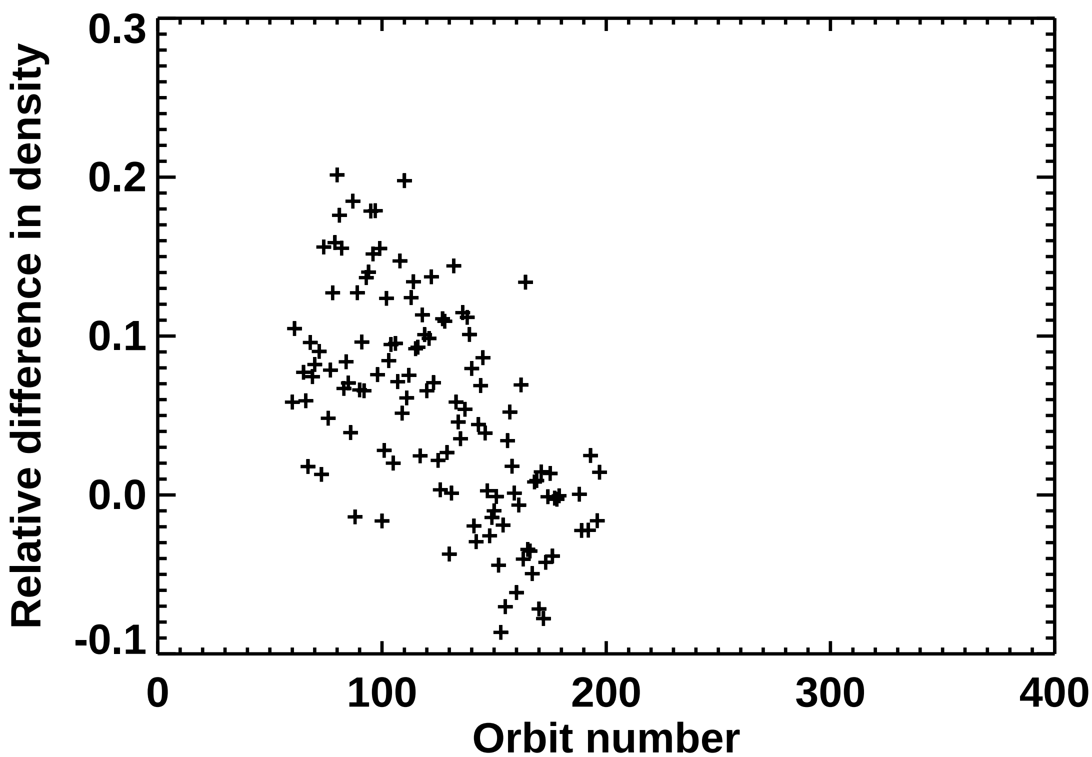

Fig. 39.— Author Paul Withers — Odyssey Accelerometer Data

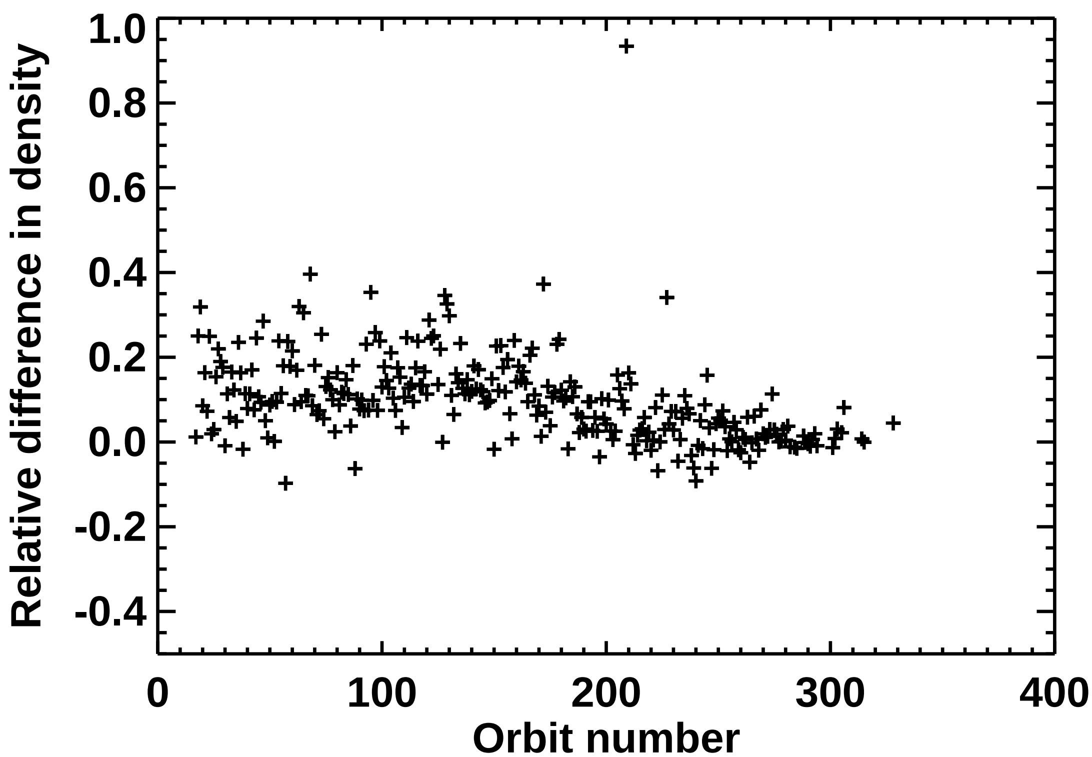

Fig. 40.— Author Paul Withers — Odyssey Accelerometer Data

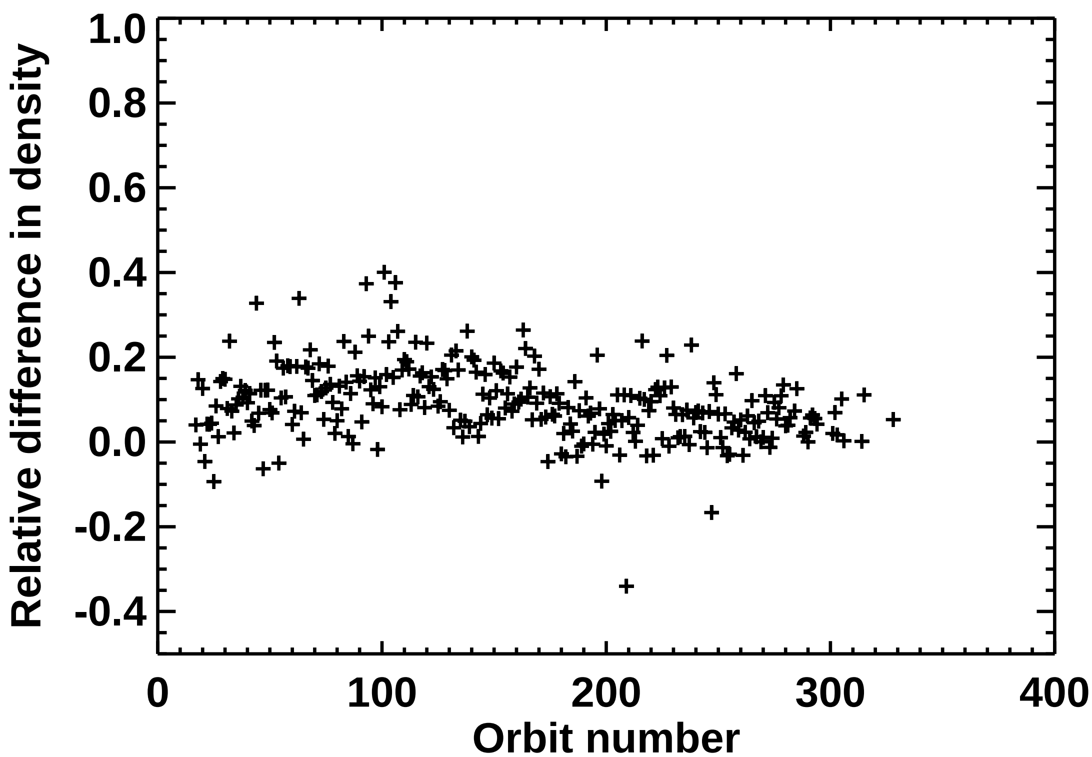

Fig. 41.— Author Paul Withers — Odyssey Accelerometer Data

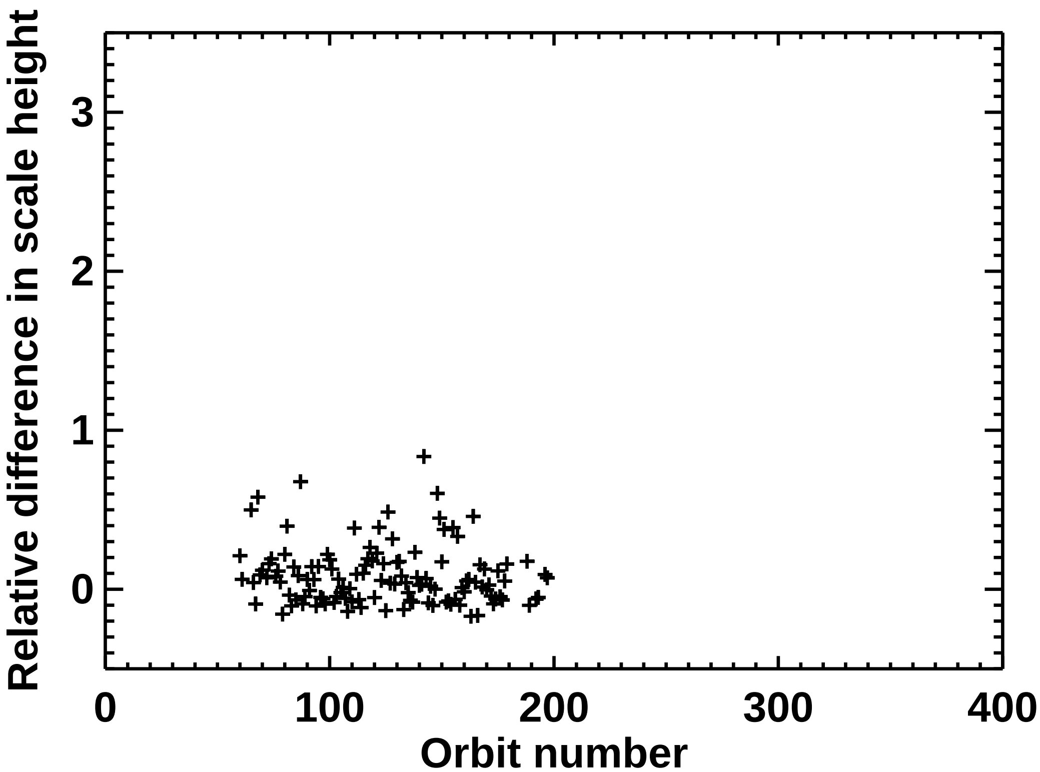

Fig. 42.— Author Paul Withers — Odyssey Accelerometer Data

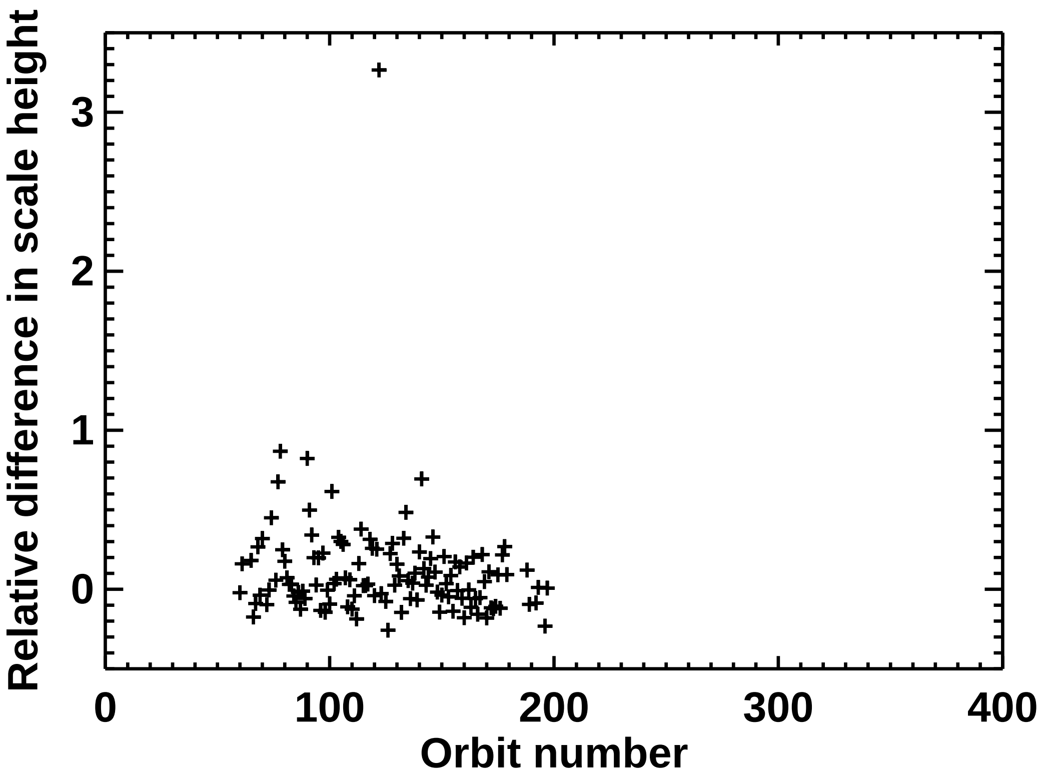

Fig. 43.— Author Paul Withers — Odyssey Accelerometer Data

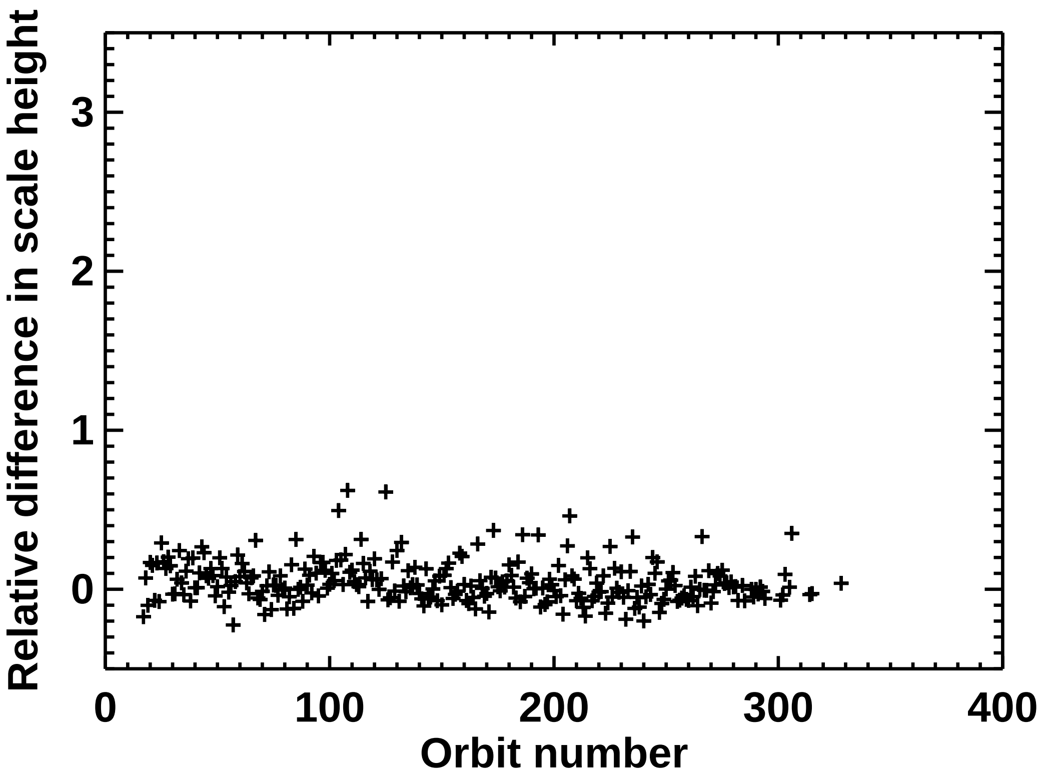

Fig. 44.— Author Paul Withers — Odyssey Accelerometer Data

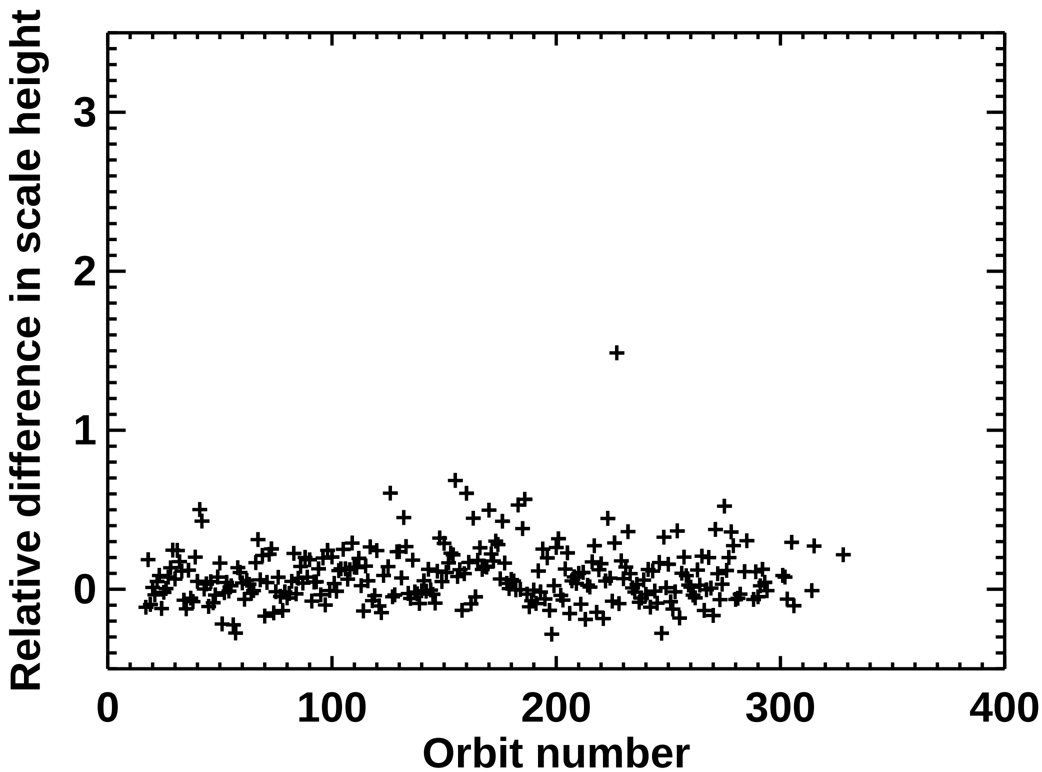

Fig. 45.— Author Paul Withers — Odyssey Accelerometer Data

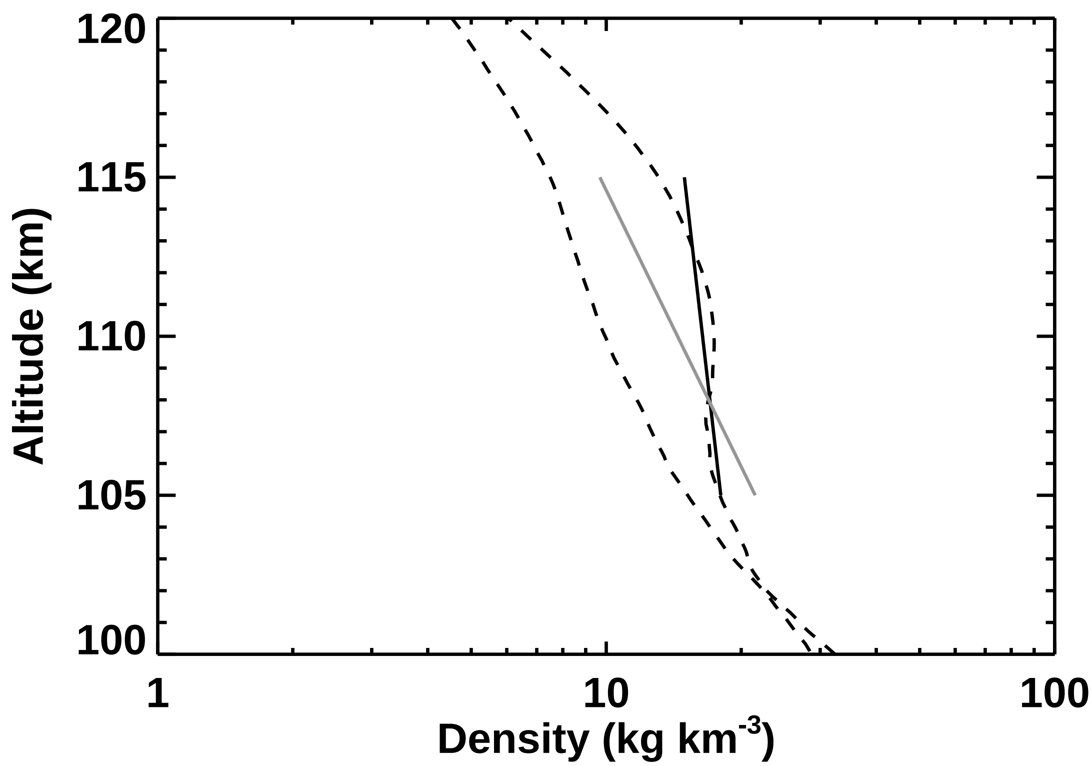

Fig. 46.— Author Paul Withers — Odyssey Accelerometer Data

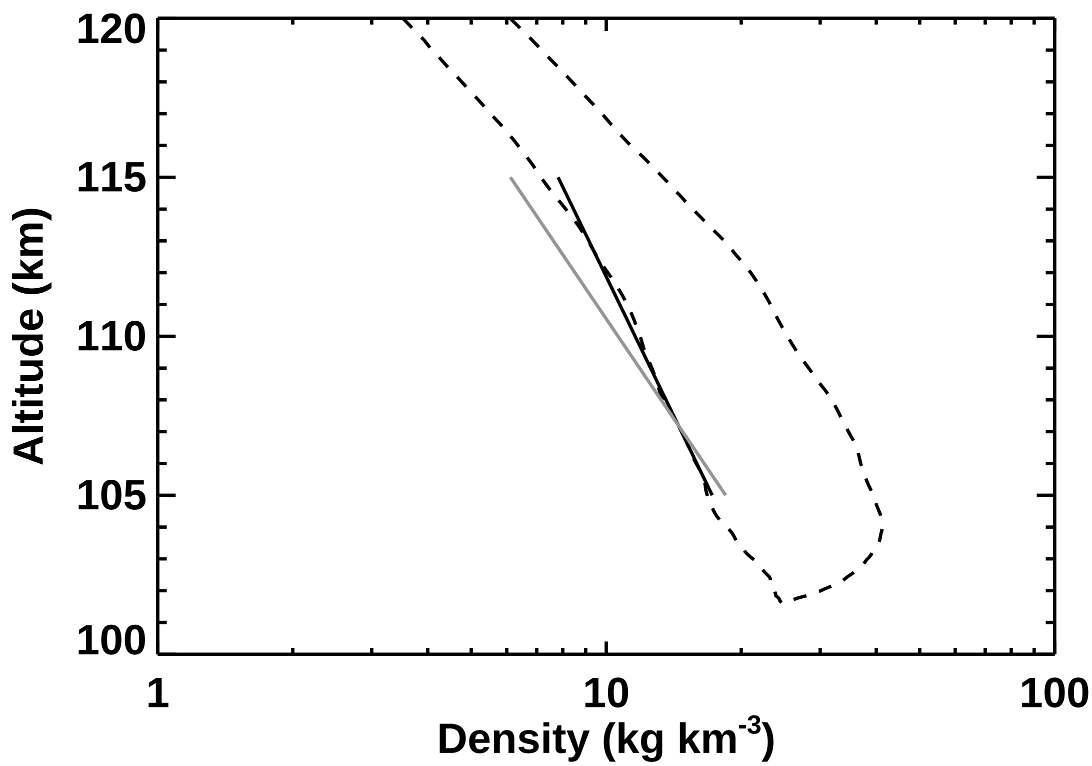

Fig. 47.— Author Paul Withers — Odyssey Accelerometer Data

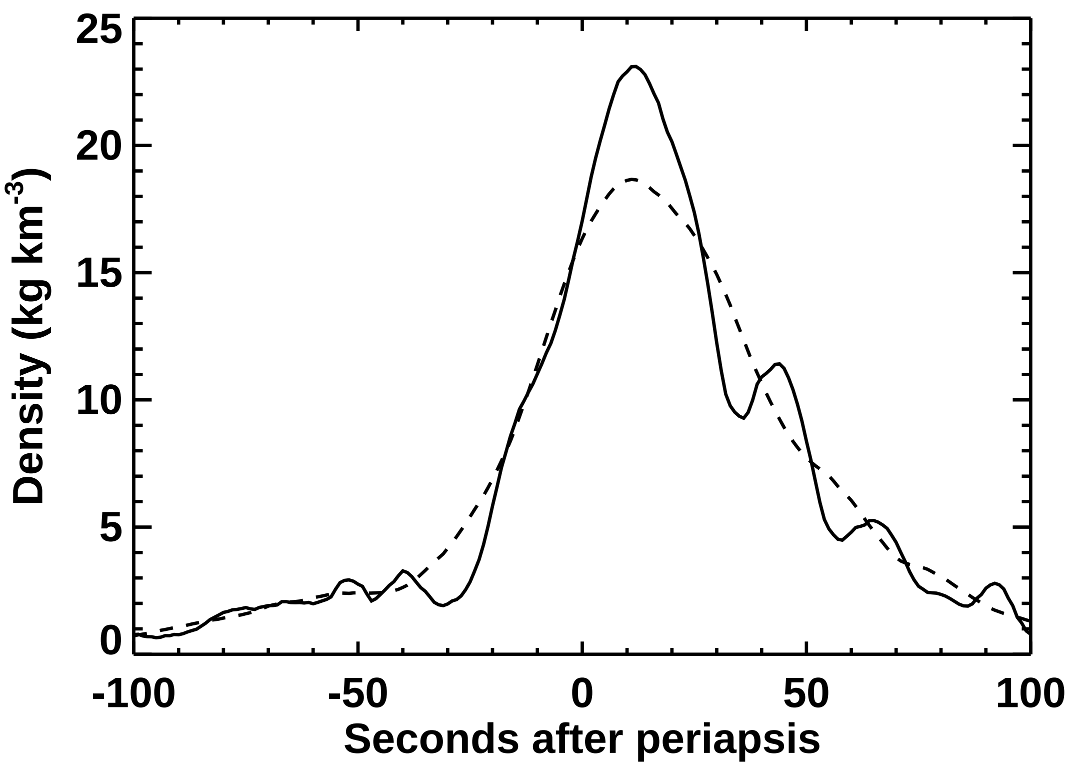

Fig. 48.— Author Paul Withers — Odyssey Accelerometer Data

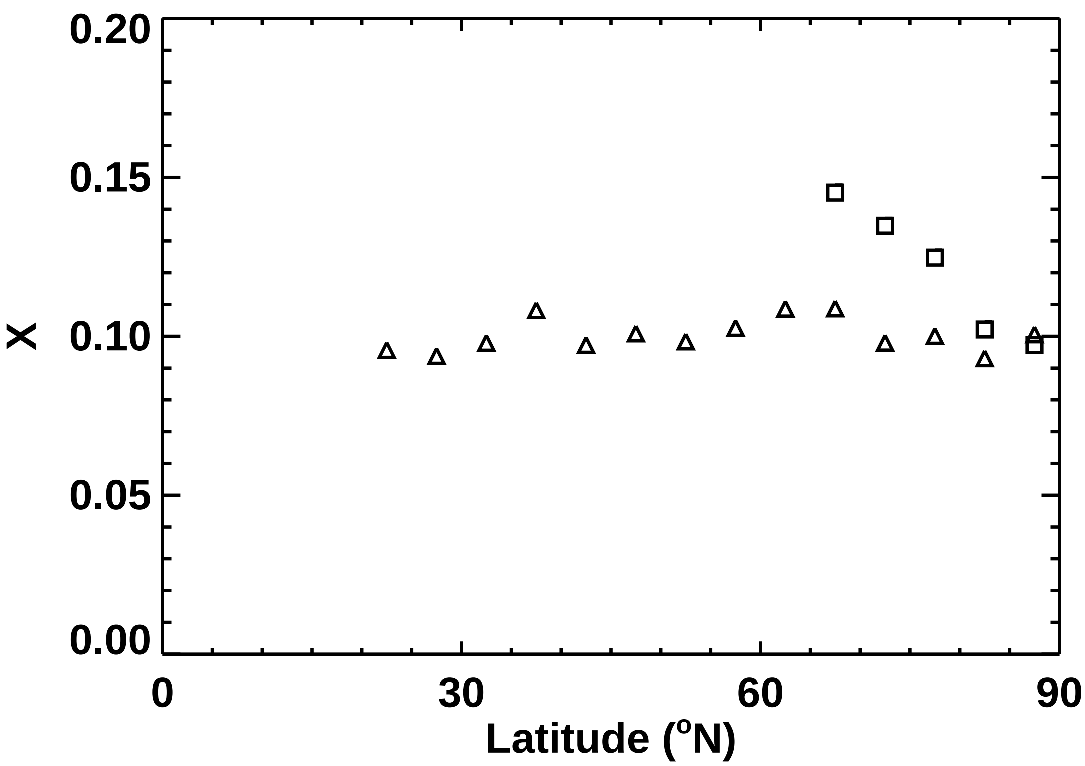

Fig. 49.— Author Paul Withers — Odyssey Accelerometer Data

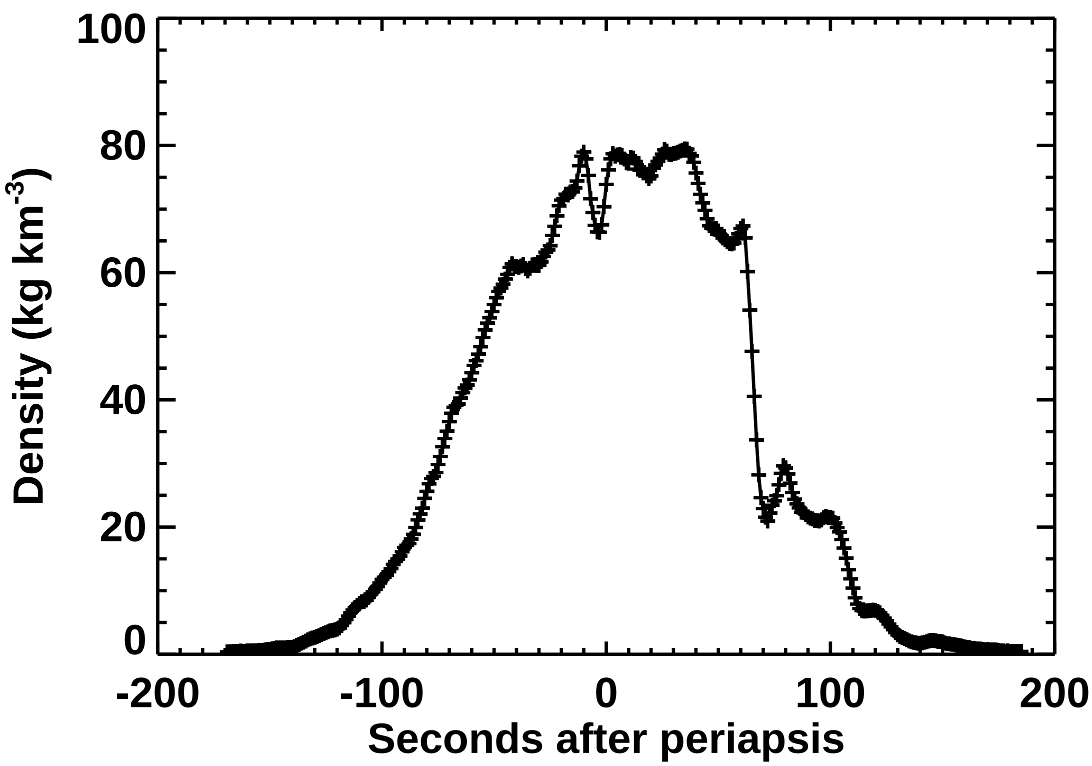

Fig. 50.— Author Paul Withers — Odyssey Accelerometer Data

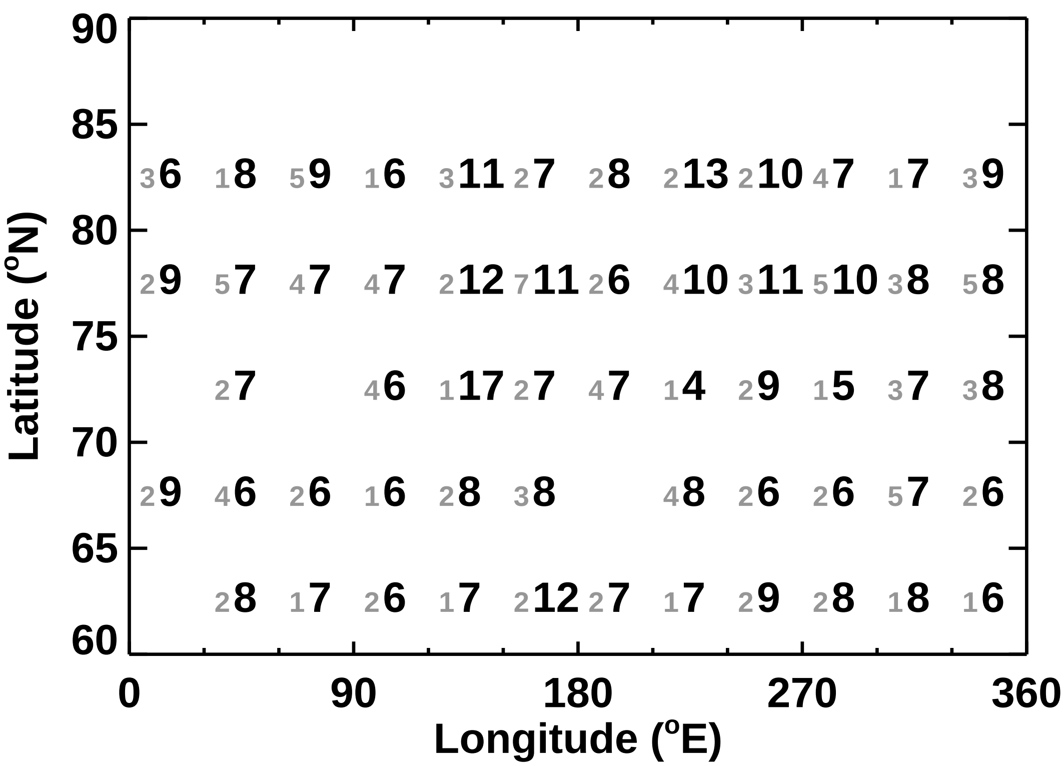

Fig. 51.— Author Paul Withers — Odyssey Accelerometer Data

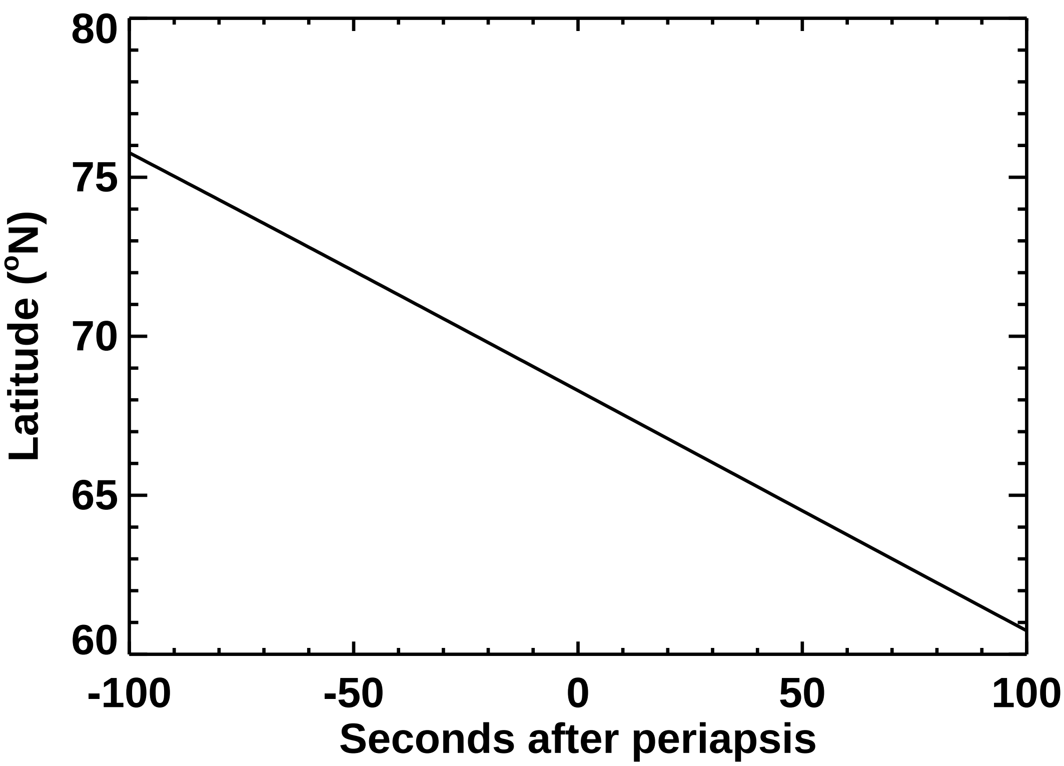

Fig. 52.— Author Paul Withers — Odyssey Accelerometer Data

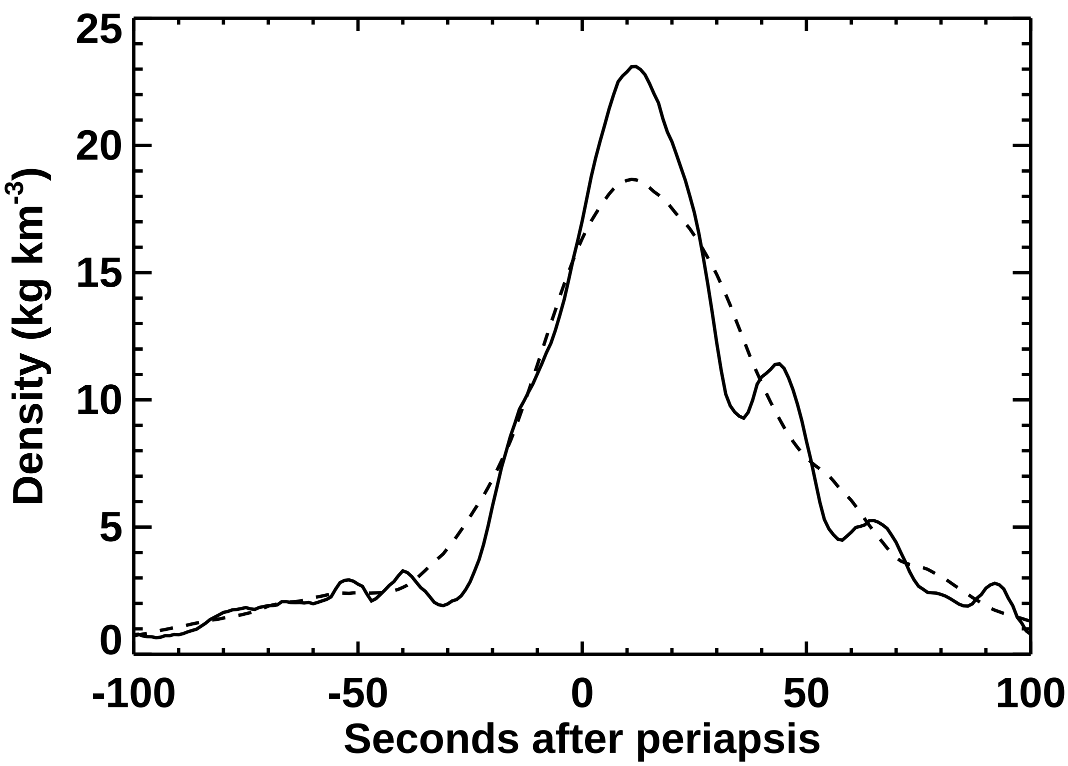

Fig. 53.— Author Paul Withers — Odyssey Accelerometer Data

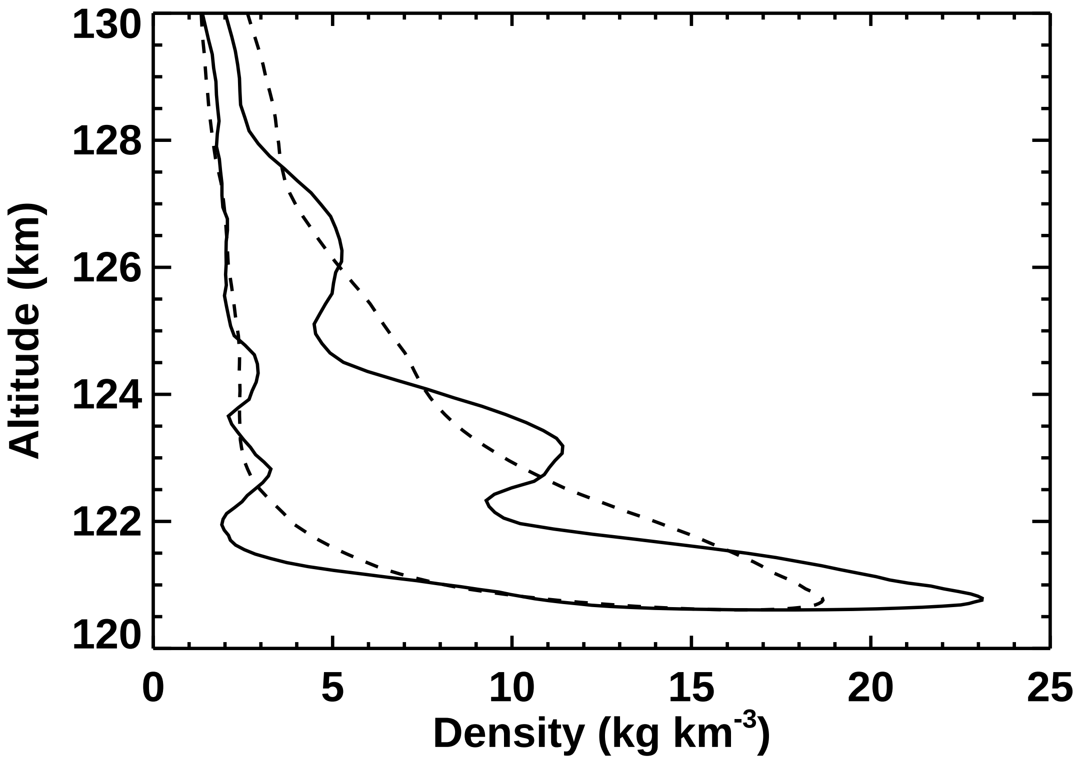

Fig. 54.— Author Paul Withers — Odyssey Accelerometer Data

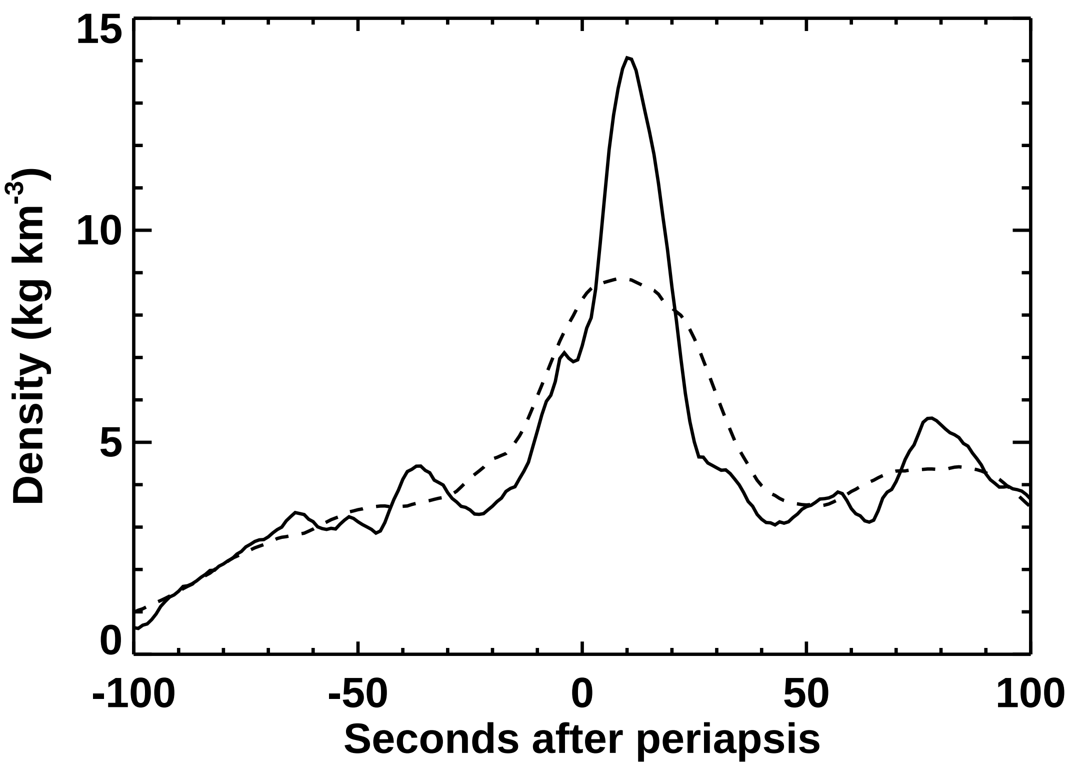

Fig. 55.— Author Paul Withers — Odyssey Accelerometer Data

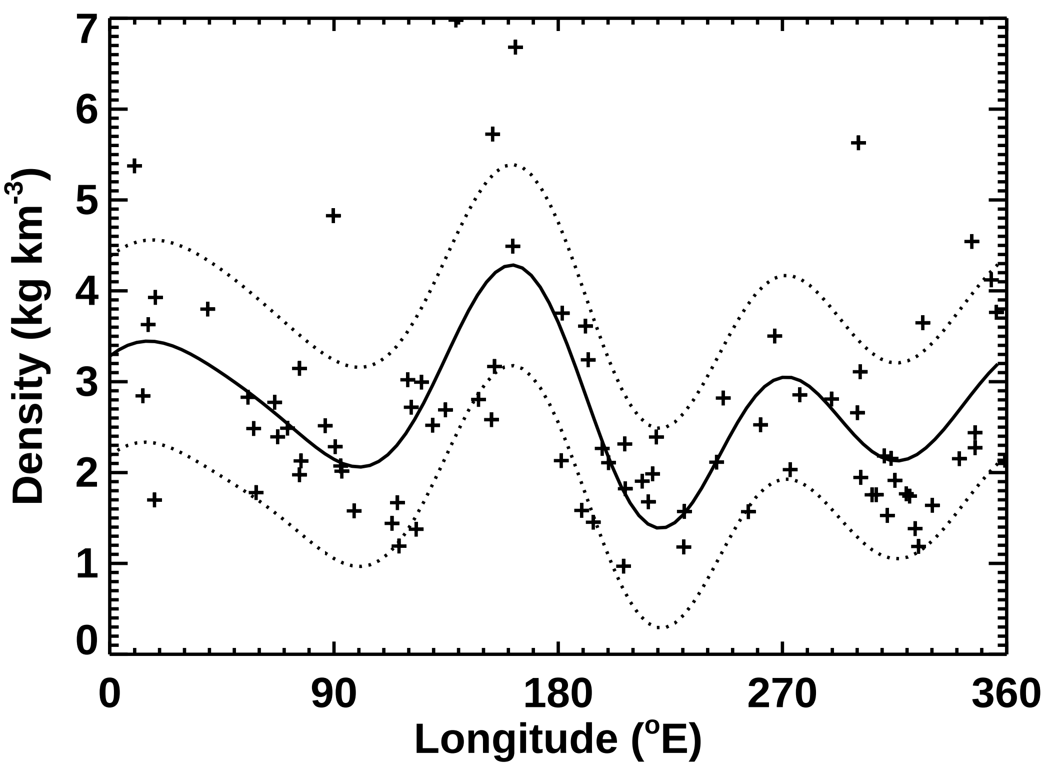

Fig. 56.— Author Paul Withers — Odyssey Accelerometer Data

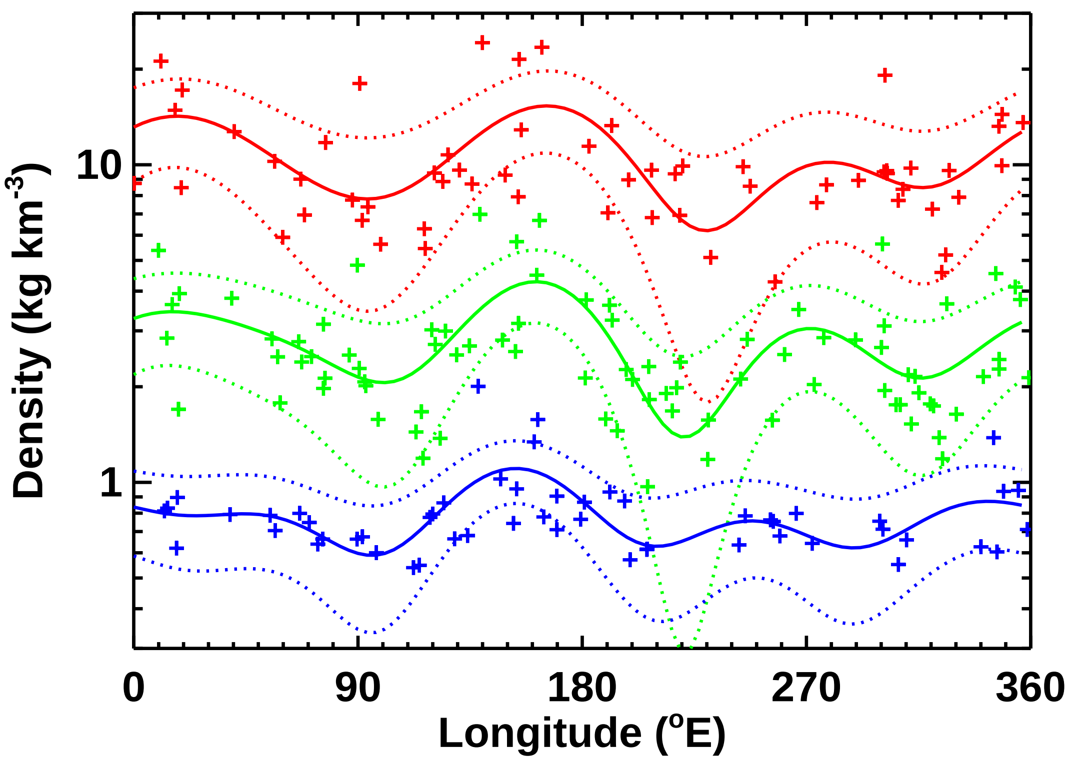

Fig. 57.— Author Paul Withers — Odyssey Accelerometer Data

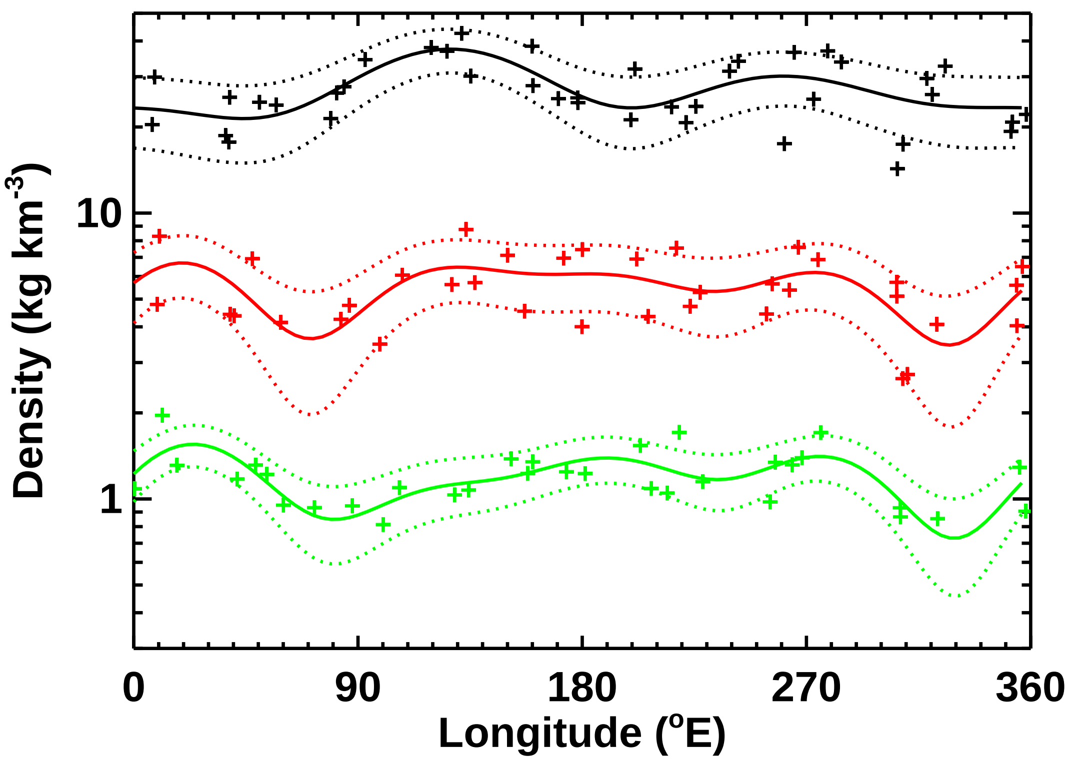

Fig. 58.— Author Paul Withers — Odyssey Accelerometer Data

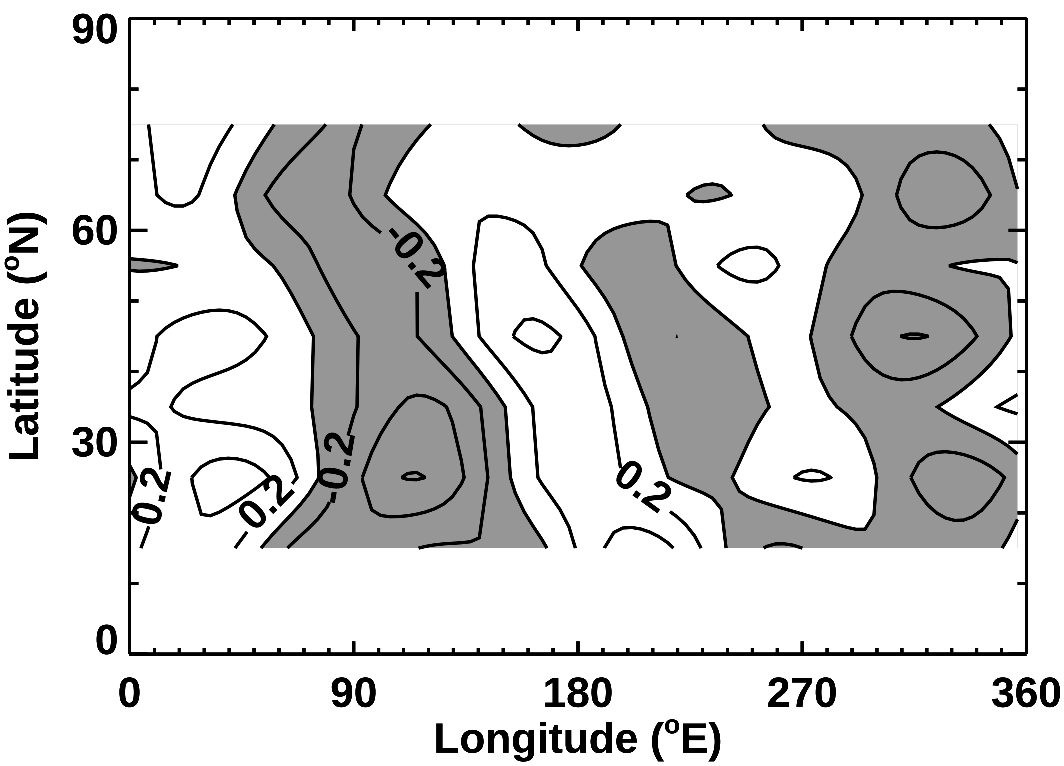

Fig. 59.— Author Paul Withers — Odyssey Accelerometer Data

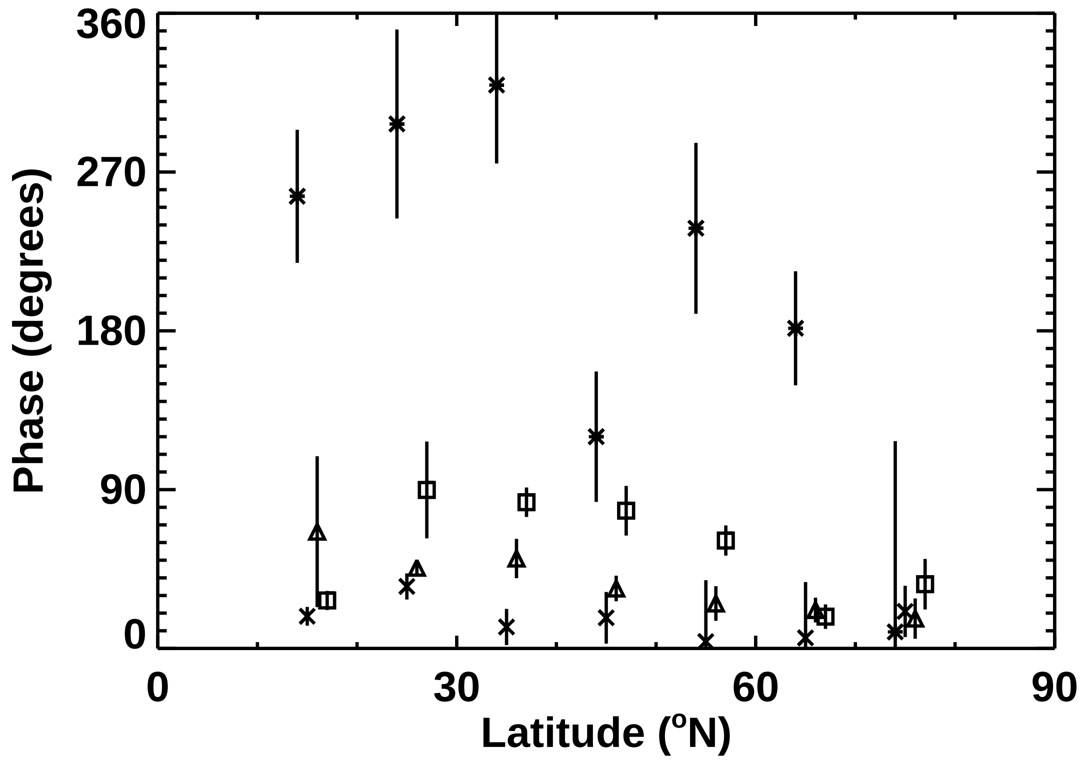

Fig. 60.— Author Paul Withers — Odyssey Accelerometer Data

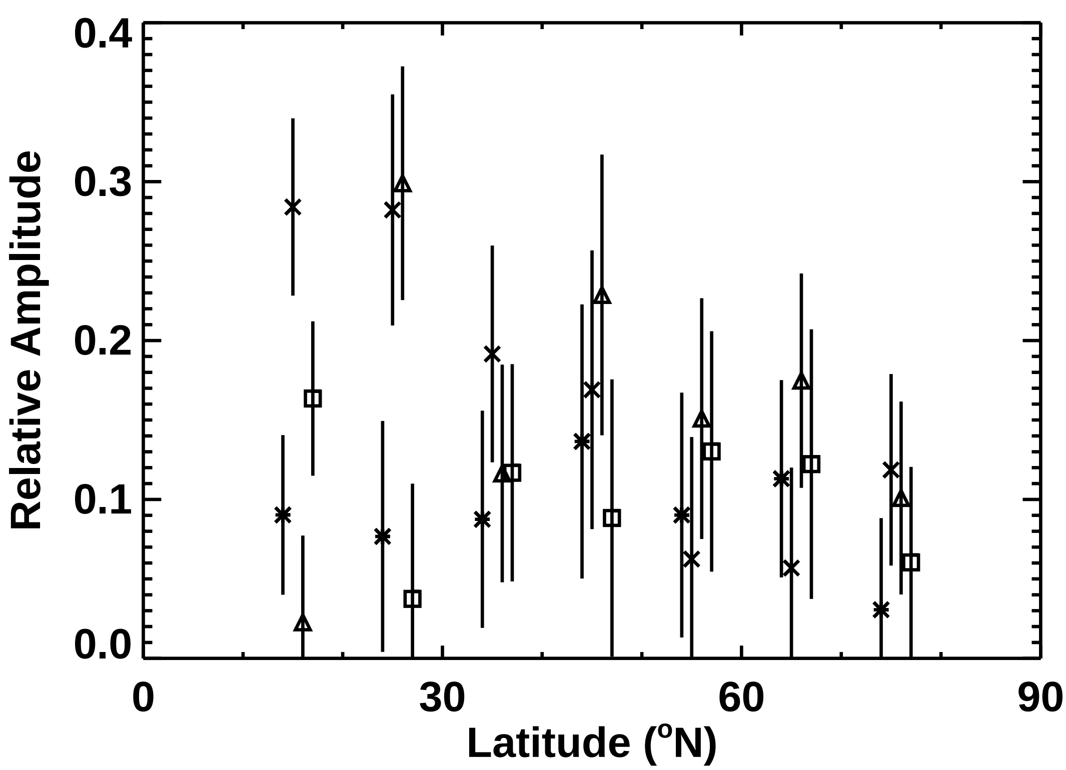

Fig. 61.— Author Paul Withers — Odyssey Accelerometer Data

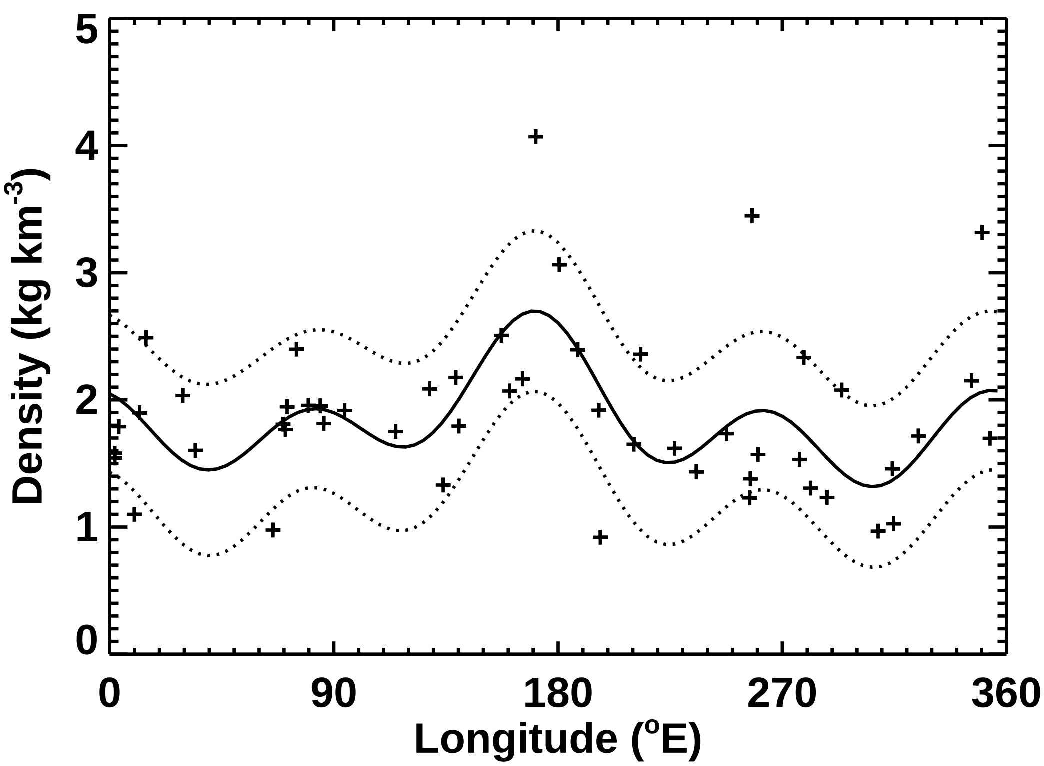

Fig. 62.— Author Paul Withers — Odyssey Accelerometer Data

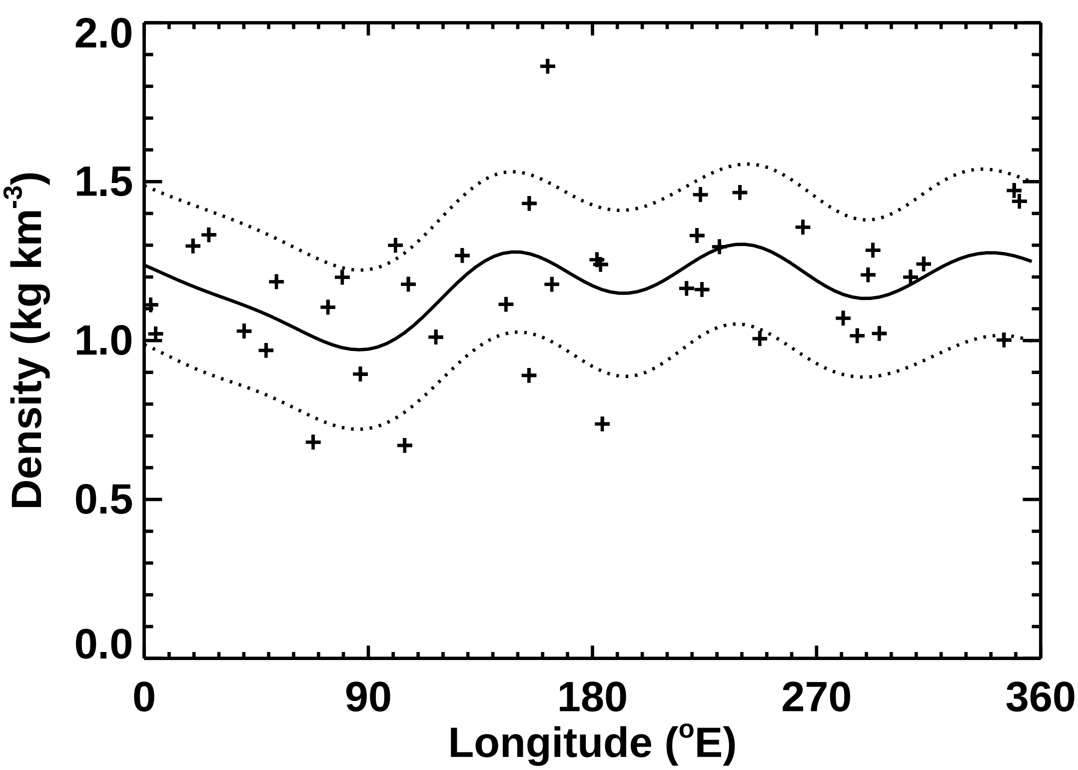

Fig. 63.— Author Paul Withers — Odyssey Accelerometer Data

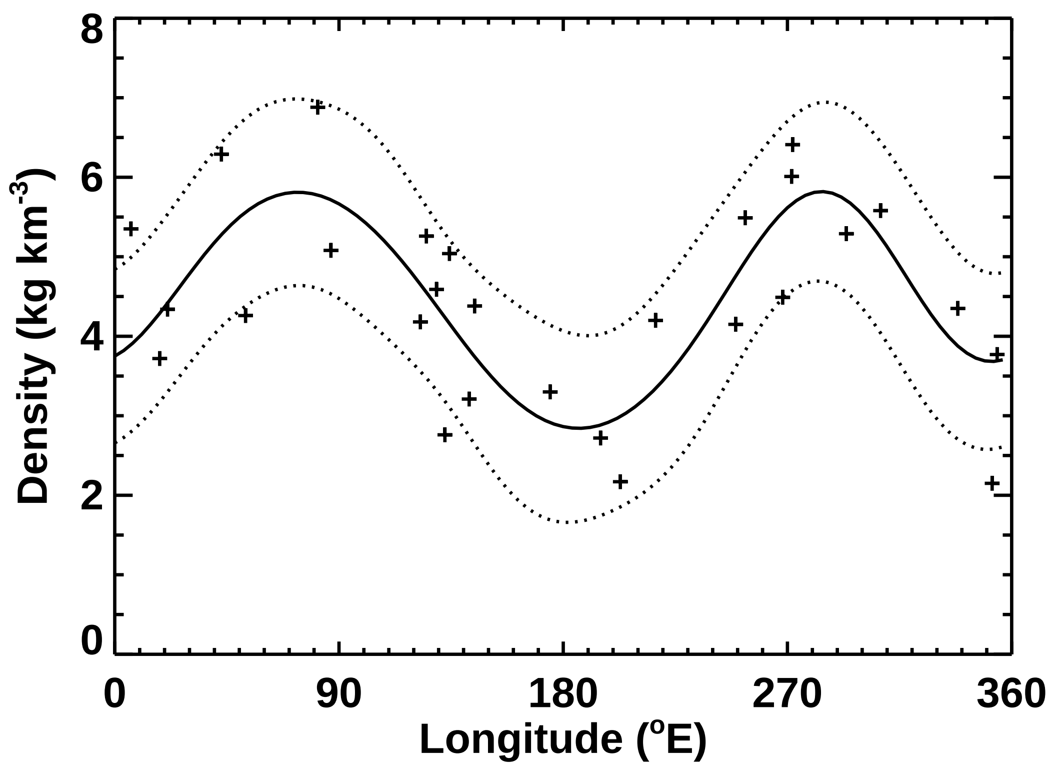

Fig. 64.— Author Paul Withers — Odyssey Accelerometer Data

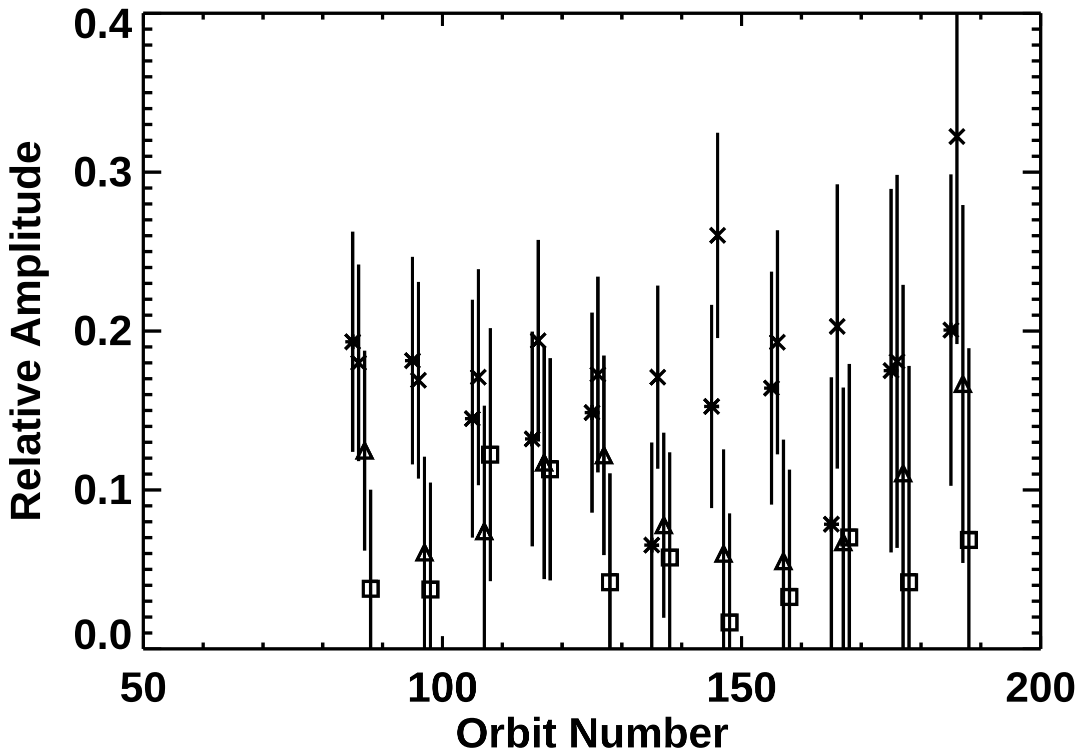

Fig. 65.— Author Paul Withers — Odyssey Accelerometer Data

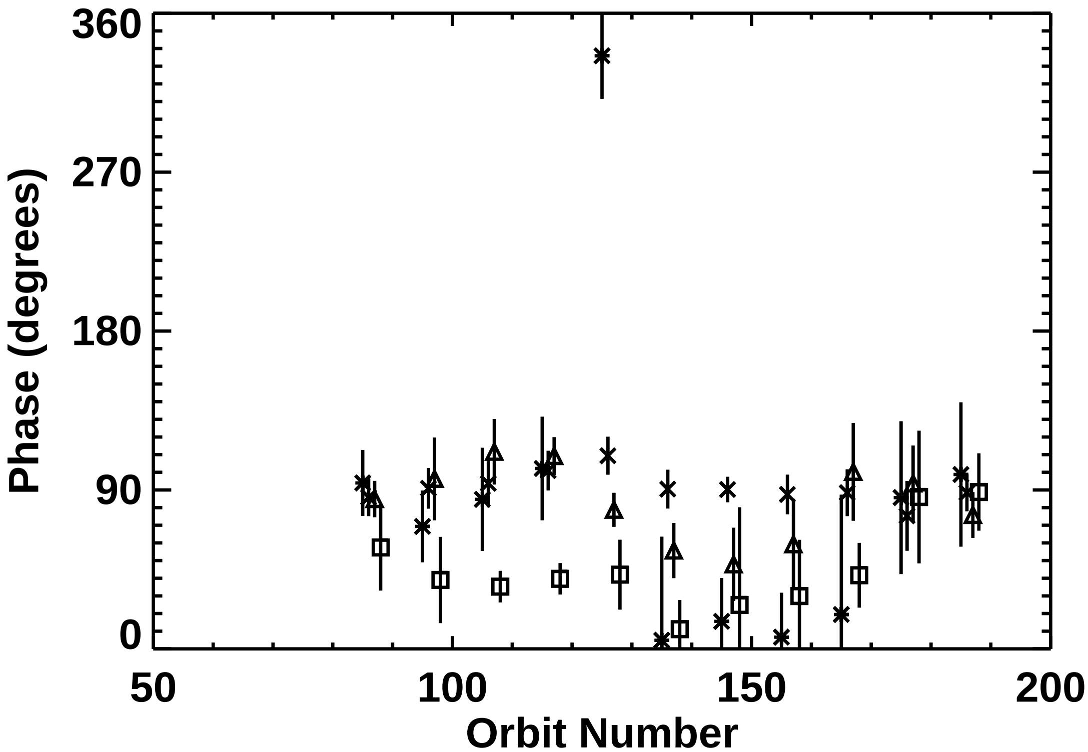

Fig. 66.— Author Paul Withers — Odyssey Accelerometer Data

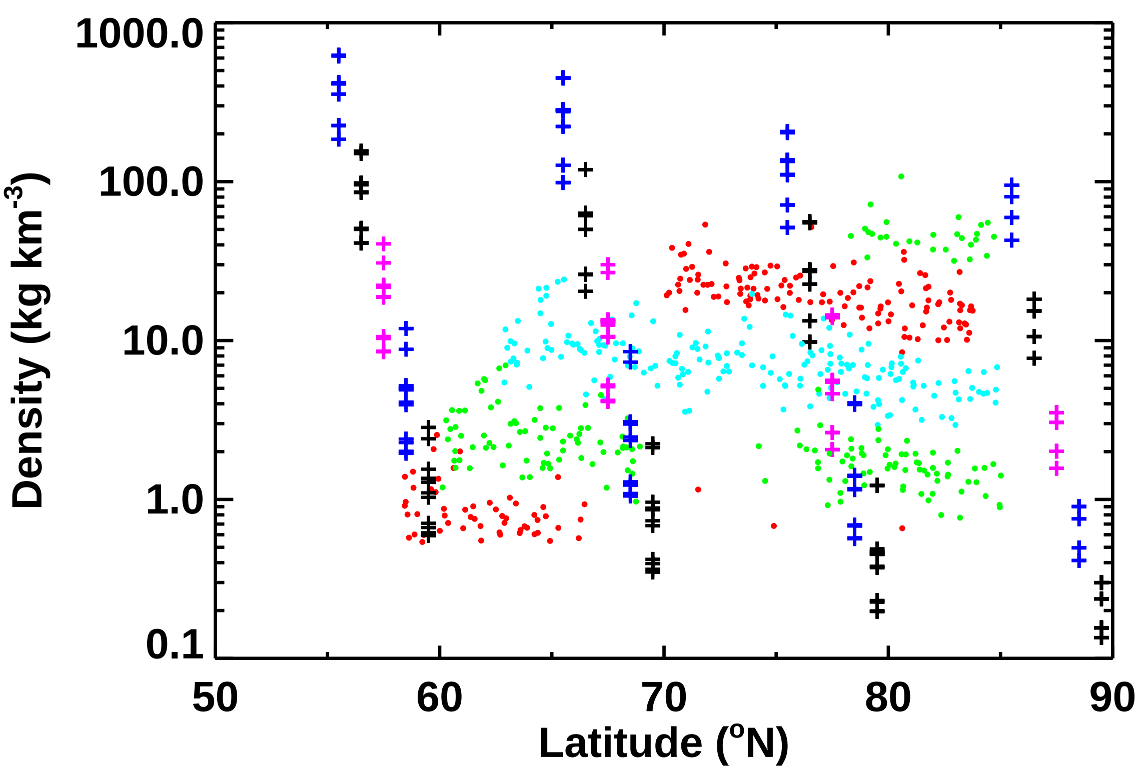

Fig. 67.— Author Paul Withers — Odyssey Accelerometer Data

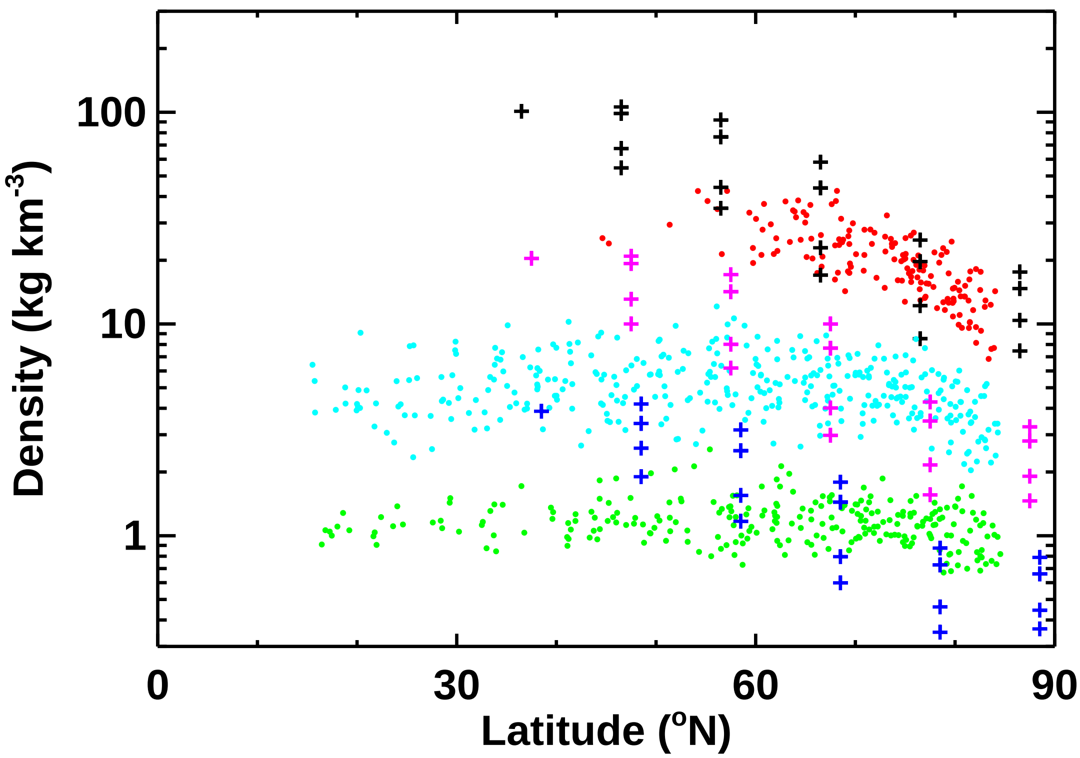

Fig. 68.— Author Paul Withers — Odyssey Accelerometer Data

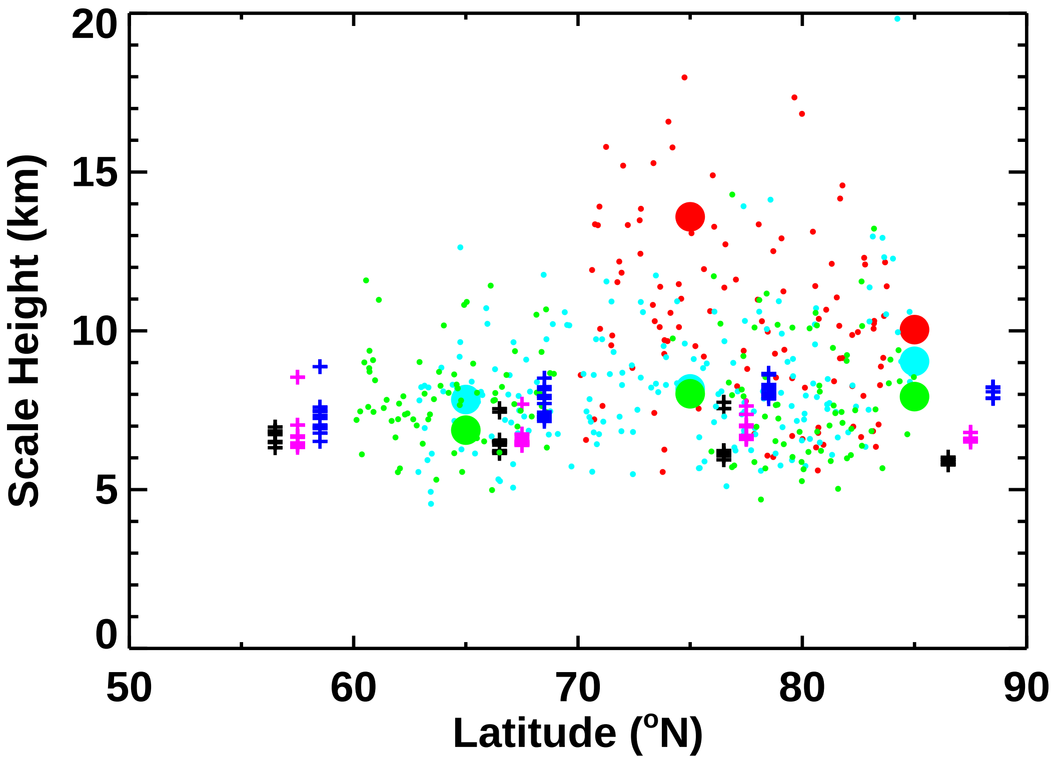

Fig. 69.— Author Paul Withers — Odyssey Accelerometer Data

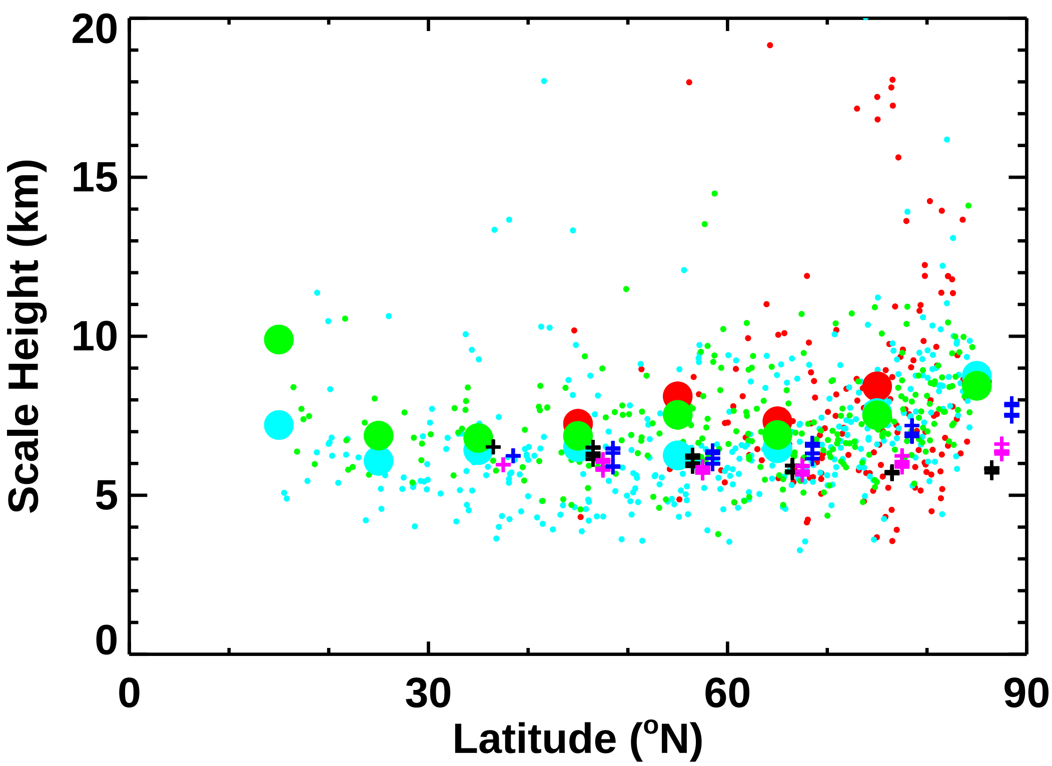

Fig. 70.— Author Paul Withers — Odyssey Accelerometer Data

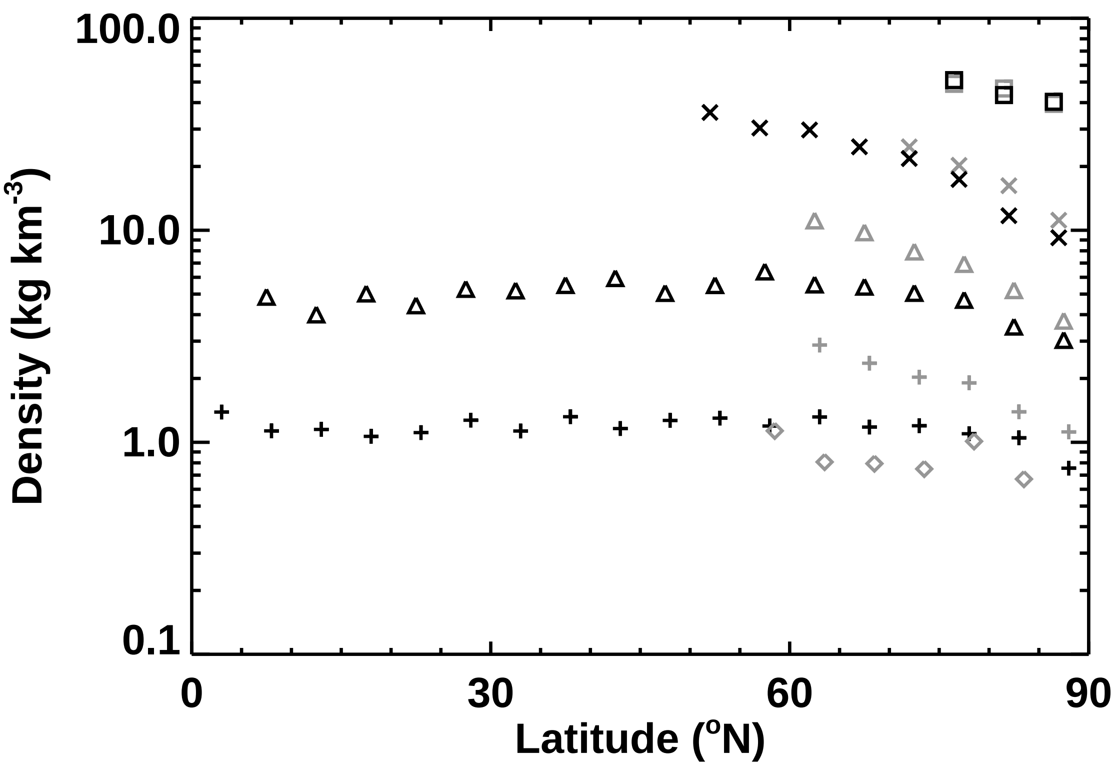

Fig. 71.— Author Paul Withers — Odyssey Accelerometer Data

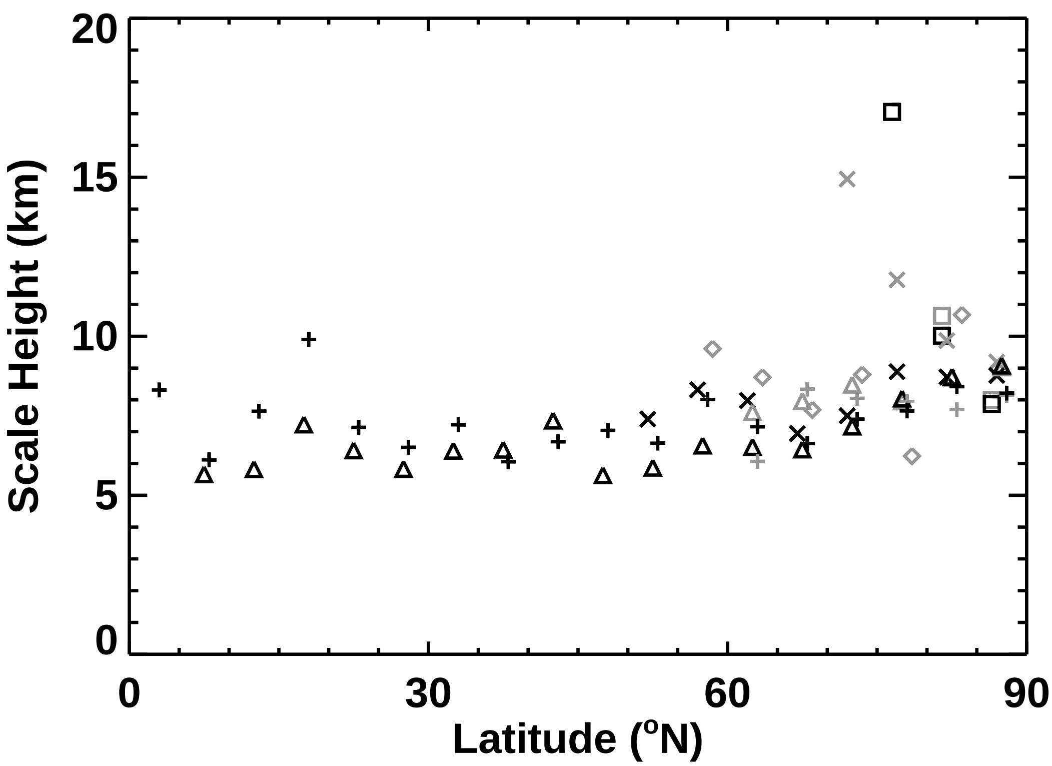

Fig. 72.— Author Paul Withers — Odyssey Accelerometer Data